2009

Aerodynamics of bridge-stay cables in the context of rigid circular cylinder in smooth flow

Arash Raeesi
University of Windsor

Aerodynamics of bridge-stay cables in the context of rigid circular cylinder in smooth flow

By

Arash Raeesi

A Thesis
Submitted to the Faculty of Graduate Studies
through the Department of Mechanical, Automotive and Materials Engineering
in Partial Fulfillment of the Requirements for
the Degree of Master of Applied Science at the
University of Windsor

Windsor, Ontario, Canada

2009

Your file Votre référence
ISBN: 978-0-494-57587-1
Our file Notre référence
ISBN: 978-0-494-57587-1

Declaration of Previous Publication

This thesis includes 1 original paper that has been previously published and 1 original manuscript to be submitted for publication in a peer reviewed journal, as follows:

Thesis Chapter	Publication Title/full citation	Publication Status
Chapter 2	Raeesi, A., Cheng, S., Ting, D. S. K., 2008. Spatial flow structure around a smooth circular cylinder in the critical Reynolds number regime under cross-flow condition. Wind and Structures, an Int. J. 11(3), 221-240.	Published
Chapter 3	Raeesi, A., Cheng, S., Ting, D. S. K., 2009. Some insight into the wind-induced phenomena of stay cables in the context of rigid static inclined circular cylinder. J. of Fluids and Structures	To be submitted

I certify that I have obtained a written permission from the copyright owner(s) to include the above published material(s) in my thesis. I certify that the above material describes work completed during my registration as graduate student at the University of Windsor.

I declare that, to the best of my knowledge, my thesis does not infringe upon anyone's copyright nor violate any proprietary rights and that any ideas, techniques, quotations, or any other material from the work of other people included in my thesis, published or otherwise, are fully acknowledged in accordance with the standard referencing practices. Furthermore, to the extent that I have included copyrighted material that surpasses the bounds of fair dealing within the meaning of the Canada

Copyright Act, I certify that I have obtained a written permission from the copyright owner(s) to include such material(s) in my thesis.

I declare that this is a true copy of my thesis, including any final revisions, as approved by my thesis committee and the Graduate Studies office, and that this thesis has not been submitted for a higher degree to any other University or Institution.

Abstract

Bridge stay cables are prone to dynamic excitations by wind. Depending on the orientation and mechanical properties of cable, wind speed, and other environmental factors, unstable cable response of different features could occur. The current work focuses on exploring the possible excitation mechanisms associated with two different types of wind-induced unstable responses observed on a rigid circular cylinder model in a series of wind tunnel tests. Characteristics of critical flow past a circular cylinder model in cross-flow were first studied to provide additional insight into the impact of critical Reynolds number regime. Then, the limited-amplitude and divergent type responses of a wind tunnel cable model were investigated. Unsteady surface pressure data were utilized to determine the separation angle, aerodynamic damping ratio, spatial correlation, and power spectra of lift and drag forces. It has been found that the divergent type response was not only accompanied with negative aerodynamic damping ratio, but also it occurred when the spatial flow was highly correlated along the cylinder. In addition, a breakdown range was detected for cable-wind relative angle around 60° within which flow characteristics could be significantly altered. This would lead to suppression of regular Karman vortex shedding in the subcritical Reynolds number range which is known to be the reason for the limited-amplitude response.

Dedication

I would like to dedicate my work to my country Iran, my family and my best friends and colleagues in Iran and Canada and Sweden. Amir, Ashkan, Ali, Bahar, Ehsan, Elham, Farmarz, Farzad, Golnar, Hadi, Hamid&Parvin, Hatef, Iman, Kianoosh, Mostafa, Mahboobeh, Majid, Mehdi, Meysam, Nader, Navid, Nibras, Nima, Pedram, Roozbeh, Samin, Yao Yao, and my supervisor in the University of Tehran, Dr. M. Raisee, thanking them for their support and kindness.

Acknowledgements

The author wishes to express his deepest appreciation and gratitude to his research supervisors, Dr. S. Cheng and Dr. D. S-K Ting for their patient guidance, fruitful discussions, and constant support during the course of this study.

Most importantly I would like to thank my family, Mom, Dad, Grandma, and Shaghayegh for their love, endless support and encouragement.

TABLE OF CONTENTS

LIST OF TABLES

LIST OF FIGURES

NOMENCLATURE

C_D	Drag force coefficient
C_L	Lift force coefficient
C_P	Pressure coefficient
D	Diameter of the circular cylinder (mm)
L_C	Correlation length
PSD	Power spectral density
R	Universal gas constant (=8.314472(15) $J \cdot K^{-1} \cdot mol^{-1}$)
R_{12}	Correlation coefficient between stations 1 and 2
R_{ij}	Correlation coefficient between stations i and j
Re	Reynolds number ($U \cdot D/ \nu$)
SSE	Sum of squared errors of polynomial fitting
St	Strouhal number ($f \cdot D/U$)
U	Wind tunnel mean velocity (m/s)
U_{Cp}	Uncertainty in the pressure coefficient
U_P	Uncertainty in the read gauge pressure (Pa)
U_{Patm}	Standard deviation of semi-diurnal pressure variation (Pa)
U_{Pdyn}	Uncertainty in the dynamic pressure (Pa)
U_N	Normal component of velocity $=U \cdot \sin\phi$
U_R	Reduced velocity ($U/f \cdot D$)
U_V	Uncertainty in the wind tunnel velocity (m/s)
$U\rho$	Uncertainty in the air density (kg/m^3)
X	Direction of X axis

Y	Direction of Y axis
Z	Direction of Z axis
Z_{ij}	Axial distance between stations i and j
Z_{max}	Maximum value of correlation length
f	Frequency (Hz)
f_s	Fluctuation frequency of separation angle or lift force(Hz)
m	Mass per unit length of cylinder (kg/m)
n	Polynomial fitting degree
z	Distance from mid-span (mm)

Greek Symbols

α	Inclination angle(°)
β	Yaw angle(°)
γ	The angle between major direction of motion and U_N
δ	Boundary layer thickness (mm)
ζ_a	Aerodynamic damping ratio
θ	Circumferential angle (°)
θ_s	Separation angle(°)
θ_{sl}	Left separation angle(°)
θ_{sr}	Right separation angle(°)
μ	Dynamic viscosity (kg/m·s)
ν	Kinetic viscosity (m^2/s)
ρ	Air density (kg/m^3)
ϕ	Cable-Wind relative angle (°)
ω_n	Undamped circular frequency of the cylinder model

Chapter 1

Introduction

1.1 Background

Flow past a circular cylinder is one of the fundamental topics in fluid dynamics. It deserves great attention because it is a common scenario in everyday life and in many engineering applications, such as wind past the strings of a wind harp or cables on cable-stayed bridges, ocean current past marine guy cables, or flow past pipes in heat exchangers. From a fluid dynamics point of view, in spite of countless number of reports on circular cylinder in cross-flow case, there remain some conflicts and uncertainties in the data reported by different investigators due to the existence of complexity in the nominally two-dimensional flow. It seems, owing to the revelation of various three-dimensional wake phenomena, the discrepancies in different reports appear to be decreasing in the last few decades. For relatively low Reynolds number regime (say up to 5×10^4), summary of some of the most important studies on the three-dimensional wake dynamics could be found in the reviews by Williamson (1997) and Zdravkovich (1997). Also, Roshko (1993) introduced aspects of bluff body aerodynamics. It is particularly interesting to note that studies on the spatial variation of flow structure around a circular cylinder, be it normal or inclined to the oncoming flow, are rarely seen in the literature. On the other hand, from a structural point of view,

when flow passes a structure, various flow-induced vibration phenomena could occur due to interaction between the structure and the passing flow. The bridge stay-cable is an example of engineering application of circular cylinders. There have been a number of reports concerning vibration of bridge stay-cable on bridge sites as well as in wind-tunnel experiments in the last few decades (Hikami and Shiraishi, 1988; Irwin et al, 1999; Main and Jones, 2001; Bosch, 2006). In addition, different response characteristics have been found when a cylinder-like structure has different orientations with respect to the oncoming flow direction. One of the most important books on the effects of wind on structures is that by Simiu and Scanlan (1996). Also, the aspects of flow-induced vibrations (Roshko, 2001), and aspects of fluctuating lift by Norberg (2003) could be used as a priori for investigating such phenomena.

A circular cylinder, considering its orientation with respect to the oncoming flow direction, can generally be either in cross-flow or inclined with respect to the flow direction. In the former case, the flow direction is perpendicular to the cylinder axis (cylinder-wind relative angle is 90°); while in the latter orientation, the cylinder-wind relative angle ϕ could be determined by two independent angles as portrayed in Figure 1-1. The relative angle ϕ between the cylinder axis and the wind direction is determined by two independent orientation angles, i.e. the inclination angle α, and the yaw angle β as portrayed in Figure 1-1. The inclination angle α is the angle between the cylinder axis and its horizontal projection, whereas the yaw angle β is the angle between the horizontal projection of the cylinder axis and the mean flow direction. Cross-flow past a circular cylinder is known as nominally two-dimensional flow while the flow past inclined-yawed cylinder has three-dimensional features. Being nominally

two-dimensional, the cross-flow over a circular cylinder implies that the flow characteristics around the cylinder surface are expected to be uniform along the cylinder span. This is the phenomenon observed within the lower subcritical Reynolds number range, though the flow in the wake and shear layers are still three-dimensional. However, by reaching the upper limits of subcritical and critical Reynolds number regime (say, $Re>10^5$), it has been found that the flow is no longer two-dimensional on the surface of the cylinder. This implies that flow is not only three-dimensional in the wake and shear layers, but also three-dimensional at the cylinder surface and flow characteristics would vary along the span of the cylinder.

1.2 Motivation

Majority of the previous studies on flow past a circular cylinder in cross-flow were conducted based on the aerodynamic data at one particular location along the cylinder span, without any revelation of spatial variation. In the case of flow past an inclined circular cylinder, considering their vast applications in engineering, there is still much more to be uncovered about the surrounding flow field. In addition, many observed wind-induced vibration phenomena on cables of cable-stayed bridges such as dry-inclined cable galloping and limited-amplitude instability of cables, have caused serious concerns of bridge designers and yet the knowledge would be central to the understanding of the basic physics underlying various types of flow-induced responses of such cables. On the other hand, the Reynolds number can affect the surrounding flow field drastically. In particular, when reaching the so-called "Critical Reynolds Number Range", even cross flow past a circular cylinder is characterized as highly three-

dimensional and very sensitive to perturbations. This signals that the critical Reynolds number range, within which many observed flow-induced vibration phenomena occur, is a key factor, to be studied thoroughly.

1.3 Scope of study

The current study is an extended effort to further analyze the experimental data from a series of wind tunnel tests conducted earlier (Cheng et al, 2005, 2008) on a rigid circular cylinder model. The tests were designed and conducted to further elucidate the physics lying behind the observed phenomena on either modeled or real inclined cables specifically the limited-amplitude response and divergent response like dry-inclined galloping. The present work focuses on studying the spatial structure of flow past a circular cylinder using the instantaneous surface pressure data sampled at five different spanwise locations along the cylinder over a Reynolds number range of 1×10^5 to 6×10^5 under smooth flow conditions. Different wind-cylinder relative angles is achieved by choosing a variety combination of inclination and yaw angles (α=90°, 60°, and 54.7°; $0°<\beta<120°$). The current research is an effort to attain the following objectives:

- Investigation of cross-flow past a circular cylinder within the critical Reynolds range and its spatial structure focusing on its fundamental features. Analyses such as spanwise correlation and power spectra of separation angle and surface pressure are used. This is presented in Chapter 2.

- Discussion on the possible generation mechanisms of the so-called dry-inclined cable galloping and limited-amplitude instability responses of inclined and/or

yawed circular cylinder on a fundamental fluid dynamics basis. This is presented in Chapter 3.

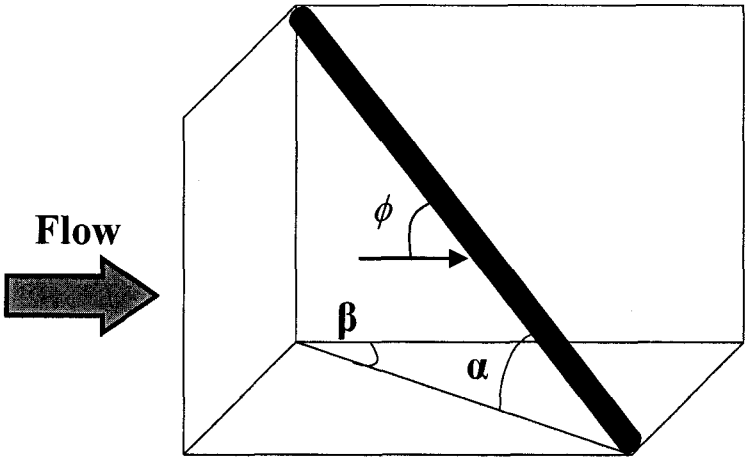

Figure 1-1- Orientation of cylinder in the flow and definition of angles

References

Bosch, H., 2006. Review of Bridge Cable Vibrations within the USA. Proceeding of 2006 Wind Induced Vibration of Cable Stay Bridges Workshop (on CD-ROM).

Cheng, S., Tanaka, H., 2005. Correlation of aerodynamic forces on an inclined circular cylinder. Wind and Structures. An Int. J., 8(2), pp. 135-146.

Cheng, S., Larose, G. L., Savage, M. G., Tanaka, H., Irwin, P. A., 2008. Experimental study on the wind-induced vibration of a dry inclined cable—Part I: Phenomena. J. Wind Eng. Ind. Aerodyn. 96, 2231-2253.

Hikami, Y. Shiraishi, N., 1988. Rain-wind induced vibration of cables in cable-stayed bridges. J. Wind Eng. Ind. Aerodyn. 29, 409-418.

Irwin, P.A., Nedim, A., Telang, N., 1999. Wind induced stay cable vibrations a case study. Proceeding of the Third International Symposium on Cable Aerodynamics, Trondheim, Norway, pp. 171-176.

Main, J.A., Jones, N.P., 2001. Evaluation of viscous dampers for stay-cable vibration mitigation. Journal of Bridge Engineering ASCE. 6 (6), 385-397.

Norberg, C., 2003. Fluctuating lift on a circular cylinder: Review and new measurements. J. Fluids and Structures. 17, 57-96.

Roshko, A., 1993. Perspectives of bluff body aerodynamics. J. Wind Eng. and Ind. Aerodyn. 49, 79-100.

Roshko, A., 2001. Aspects of flow-induced vibrations. J. of Fluids and Structures. 15, 415-425.

Simiu, E., Scanlan, R. H., 1996. Wind Effects on Structures, an Introduction to Wind Engineering, John Wiley & Sons.

Williamson, C. H. K., 1997. Advances in our understanding of vortex dynamics in bluff body wakes. J. of Wind Eng. and Ind. Aerodyn. 69-71, 3-32.

Zdravkovich, M.M., 1997. Flow around circular cylinders, Fundamentals, Vol. 1, University Press, Oxford, England.

Chapter 2

Spatial flow structure around a smooth circular cylinder in the critical Reynolds number regime under cross-flow condition

2.1 Introduction

Flow past a circular cylinder is one of the fundamental topics in fluid dynamics. It deserves great attention because it is a common scenario in everyday life and in many engineering applications, such as wind past the strings of a wind harp or cables on cable-stayed bridges, ocean current past marine guy cables, or flow past pipes in heat exchangers. A decent knowledge of flow pattern around such a simple bluff body in the smooth flow condition is a priori to explore the effects of complex turbulent flow, such as natural wind, on the practical cylindrical type of structures (Simiu and Scanlan, 1996). Though intensive effort has been invested in advancing this evergreen topic for over a century, some aspects of the phenomenon are still far from comprehension. In particular, studies on the spatial variation of flow structure around a circular cylinder, be it normal or inclined to the oncoming flow direction, are rarely seen in the literature, yet the knowledge would be central to the understanding of the basic physics underlying various types of flow-induced responses of a circular cylinder.

Majority of the previous studies on flow past a circular cylinder were conducted based on the aerodynamic data at one particular location along the cylinder span,

without revelation of spatial variation. Roshko (1961) first attempted to classify the characteristics of cross-flow past a circular cylinder at very high Reynolds numbers regime, where he defined different flow states for Reynolds numbers in excess of 1×10^5 as sub-critical ($C_d\approx1.2$), supercritical (C_d value drastically reduces to about 0.3), and transcritical ($C_d\approx0.7$). Within each subrange, the flow exhibits different features of aerodynamic characteristics. He also found that the regular periodic vortex shedding, which ceased in the supercritical regime, reappeared in the transcritical regime. Roshko's findings and the existence of different sub-regimes which he defined were reconfirmed later by a number of researchers including Achenbach (1968), Bearman (1969), Batham (1972) and Schewe (1983). Zdravkovich (1997) made a comprehensive review for a broad range of researches done on this subject, where he used the notation "TrBL" (transition in boundary layer) to represent the Reynolds numbers ranging from 1×10^5 up to a few millions (within which the current experimental study was conducted). This range was subdivided into TrBL0 as the sub- or pre-critical regime ($1\sim2\times10^5<Re<3\sim3.4\times10^5$); TrBL1 as the single separation-bubble regime with steady asymmetric pressure distribution ($3\sim3.4\times10^5<Re<3.8\sim4\times10^5$); TrBL2 as the range accompanied with the formation of the second separation-bubble and return of the flow symmetry ($3.8\sim4\times10^5<Re<5\sim10\times10^5$); TrBL3 as the supercritical regime where the regular vortex shedding ceases ($5\sim10\times10^5<Re<3.6\sim6\times10^6$) and TrBL4 as the post- or transcritical regime which is followed by reappearance of the periodic vortex shedding ($Re>3.6\sim6\times10^6$). To be consistent with other literatures, Zdravkovich's classification is used in the present paper and the term "critical Reynolds number regime" will be used to represent TrBL1 and TrBL2 regimes.

Bearman (1969) observed a steady lift force as a consequence of asymmetric flow structure around a circular cylinder within a narrow range of critical Reynolds number. He suggested that this steady lift force could be induced by the formation of laminar separation bubble on just one side of the cylinder surface within that particular Reynolds number range. Beyond that range, the second separation bubble would appear on the other side, the flow structure would become symmetric again and the steady lift force would then return to zero. Schewe (1983) confirmed Bearman's findings and proposed an associated mechanism. According to him, the transition in the boundary layer depended on the micro-scale perturbations which would not occur necessarily on both sides of the cylinder surface simultaneously. Therefore, the formation of the first separation bubble on one side of the cylinder surface would cause a steady circulation around the cylinder and decelerate the flow over the opposite side. The transition and formation of the second separation bubble on the other side would thus be delayed. It should also be noted that different aspects of fluctuating lift force on a circular cylinders have been studied in a very comprehensive and recent review by Norberg (2003), within which his own measurements in the subcritical range (Re up to 2.1×10^5) were compiled.

The three-dimensional structure of the flow around a circular cylinder whether normal or inclined to the oncoming flow was only addressed in a limited number of studies. For the case of a cross-flow cylinder, Roshko (1954) first observed three-dimensional structures of flow (in terms of either slanted or wavy spanwise eddy filaments) at Reynolds numbers as low as around 100. It was later found that (Slaouti and Gerrard, 1980) subtle difference in boundary conditions at the two ends can cause

the flow characteristics to vary along the cylinder span. Spanwise correlation length, i.e. the maximum length along which correlation coefficient of sectional aerodynamic characteristics is not lost, is another feature of three-dimensional flow. Within the subcritical Reynolds numbers range, the spanwise correlation length could be found in the study by Norberg (2001) and references cited in it. It was shown that within the subcritical Re range, the spanwise correlation length has a general decreasing trend with increase of Reynolds number except for a local maximum at $Re=5\times10^3$ (Norberg, 2001). Other studies addressing such three-dimensional structures in either wake or shear layers were reviewed by Roshko (1993) and later by Williamson (1997). Most of them were conducted in the subcritical Re range by flow visualization.

At higher Reynolds numbers, when the transition in boundary layer occurs, the impact of perturbations on the three-dimensional structure of the flow around a cross-flow circular cylinder was identified by Bearman (1969). Further, it was noticed that as the surrounding flow become three-dimensional, the cylinder base pressure is no longer uniform along the cylinder span. Based on the force measurement at both ends of the circular cylinder in the critical Reynolds number regime, Schewe (1983) suggested that the flow field around a circular cylinder in cross-flow could be divided along its span into many subsystems, which would differ slightly from each other in terms of aerodynamic characteristics. To the knowledge of the authors, there have been very few studies dedicated to investigate such three-dimensionalities at Reynolds numbers corresponding to the critical regime. Higuchi et al. (1989) conducted experiments over a range of Re from 0.8×10^5 to 2×10^5. They found that flow motion in this regime is characterized by the intermittent boundary-layer separation and reattachment

accompanied with the presence of well-defined spanwise cell structures. Different spanwise structures were also observed in the flow visualizations by Humphreys (1960), Korotkin (1976), and more recently, Gölling (2004) within the TrBL regime. It is clear from these studies that much is yet to be uncovered regarding the three-dimensional structure of flow around a circular cylinder, especially in the critical Reynolds number regime.

The present work focuses on studying the spatial structure of flow pattern around a circular cylinder in cross-flow. The analysis is based on the experimental data of a wind tunnel test conducted earlier by Cheng and Tanaka (2005). Surface pressure was measured at five different longitudinal locations along the cylinder span, at fourteen Reynolds numbers in the TrBL regime from 1.14×10^5 to 5.85×10^5. Fluctuating flow characteristics such as the separation angle and aerodynamic forces at those five locations and their spanwise correlations are analyzed. The possible existence of multiple flow regimes at different spanwise locations as suggested by Schewe (1983) is also discussed.

2.2 Experimental details

A series of wind tunnel tests has been conducted at National Research Council of Canada (NRCC) for studying wind-induced vibration of bridge stay cables by using a rigid smooth circular cylinder model (Cheng and Tanaka, 2005). The current study is based on the experimental data obtained from this set of experiments.

The tests were conducted under smooth flow condition in the 2m high by 3m wide wind tunnel at NRCC. The maximum wind speed of the tunnel is 140m/s. To simulate the cross flow case, a rigid steel circular cylinder model with a diameter of 88.9mm was installed vertically across the center of the test section and placed perpendicular to the on-coming flow direction, as shown in Figure 2-1(a). Elliptical plates were attached close to both ends of the model to reduce the horse-shoe vortex and boundary-layer end effects. The exposed length of the cylinder to the flow in between the end plates was 1.93m. This leads to a model aspect ratio of 21.7. The blockage ratio is 2.96%.

To monitor the flow pattern around the cylinder model, a total of 192 pressure taps of 1mm diameter were installed on the model. As illustrated in Figure 2-1(b), five pressure tap rings were fitted at different longitudinal locations along the cylinder span (Z direction), with the plane of each ring perpendicular to the model axis. Each ring contains 32 pressure taps over the circumference of the model with a more condensed arrangement on the downstream side. Figure 2-2 portrays the layout of pressure taps on a typical ring and the definition of the X and Y axes with respect to the on-coming wind direction. The angular positions are defined clockwise, with respect to the location of tap number 17. Also, left and right sides of the cylinder are defined in Figure 2-2 with respect to the wind direction. In addition, 32 pressure taps were installed along two longitudinal lines at the leeward side of the model, with 16 taps on each line. The pressure taps were connected to five electronic pressure scanners (Scanivalve ZOC™Kulite) embedded in the model through urethane tubes, nominally 1m long.

(a) Cross-flow circular cylinder model in the NRCC wind tunnel

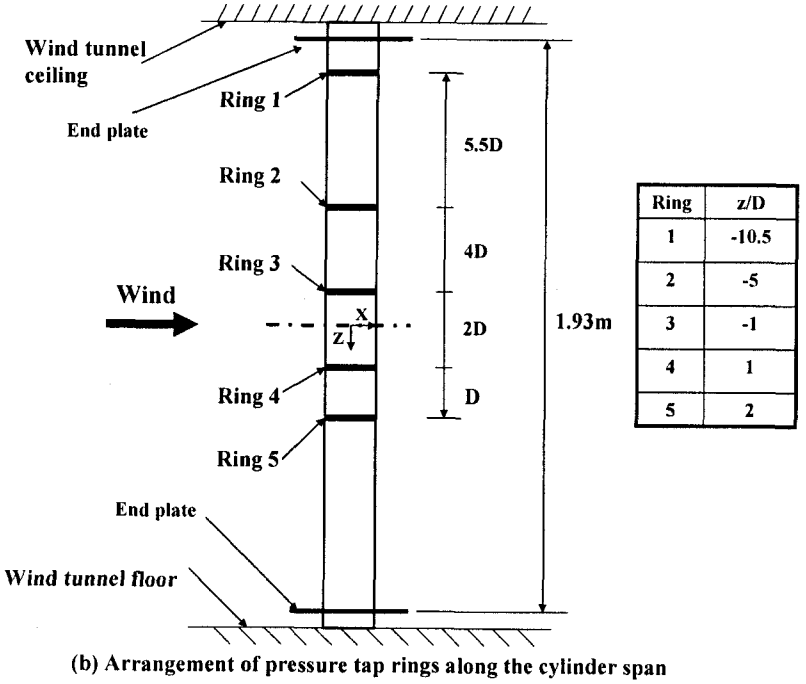

Ring	z/D
1	-10.5
2	-5
3	-1
4	1
5	2

(b) Arrangement of pressure tap rings along the cylinder span

Figure 2-1 Experimental setup

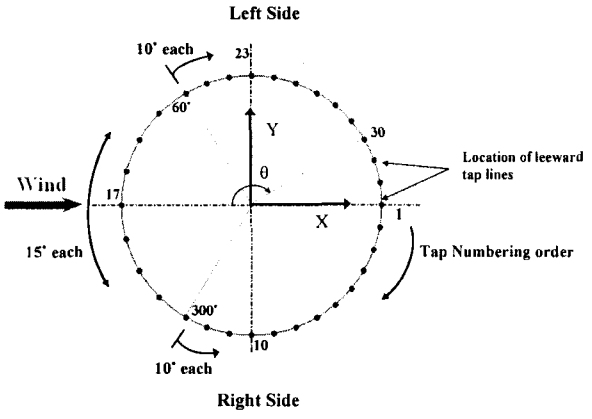

Figure 2-2 Pressure tap array around cylinder circumference on a typical ring

The tests were conducted under smooth flow conditions, with the longitudinal turbulence intensity at the model location being 0.13%. Unsteady surface pressure of the cylinder model at the tap locations were measured over a wind tunnel speed range of 19.6m/s to 98.6m/s, which, based on the cylinder diameter, corresponded to a Reynolds number range of 1.14×10^5 to 5.85×10^5. Two sampling frequencies of 400Hz and 1200Hz were used, with details described in Table 2-1. The distortion of the sampled pressure signals induced by the tubing system was corrected before further analyses of the collected data. Due to the relatively low percentage of blockage ratio, no correction of blockage effect was made to the raw data. More details regarding this series of wind tunnel experiments are reported by Cheng and Tanaka (2005).

2.3 Results and discussion

In order to study the spatial structure of flow past a circular cylinder in the critical Reynolds number range, the surface pressure time-histories are further processed to obtain parameters that are key to the representation of the surrounding flow structure. The time-averaged surface pressure of the cylinder, time-averaged separation angles, power spectra of fluctuating separation angles, and the spanwise correlations of separation angles, force coefficients and surface pressures are presented in the following sections.

Table 2-1 Experimental conditions

Sampling mode	Sampling frequency (Hz)	Testing cases	Re range	Sampling time(S)	Activated taps	No. of active taps
Low	400	14	1.14×10^5 to 5.85×10^5	120	At 5 rings + 2 lines	192
High	1200	12	1.14×10^5 to 5.85×10^5	60	Rings 2 and 4	64

2.3.1 Surface pressure distributions

2.3.1.1 Time-averaged surface pressure

The time-averaged cylinder surface pressures at the locations of all five rings are presented in Figure 2-3. The dimensionless pressure coefficient is represented by $C_p = P/(0.5\rho U^2)$, where U is the wind tunnel speed, ρ is the air density, and P is the

measured gauge pressure. Figure 2-3(a) portrays the time-averaged surface pressure at $Re=1.14\times10^5$, which is within the TrBL0 (sub-critical) regime. It can be seen from the figure that the surface pressure around the cylinder circumference shows almost the same distribution at all five spanwise locations considered. This indicates that the flow structure in this Reynolds number range is primarily two-dimensional which agrees with many earlier studies (Fage, 1928; Achenbach, 1968; Batham, 1972). Distribution of the time-averaged surface pressure at $Re=3.04\times10^5$ is illustrated in Figure 2-3(b), which corresponds to the TrBL1 regime. A highly asymmetric steady pressure distribution can be observed particularly at the spanwise locations of Rings 1, 4 and 5 (where z/D=-10.5, 1, 2 respectively). This fact correlates to the formation of a single separation bubble on one side of the cylinder surface, which is the phenomenon to be expected in the TrBL1 regime, as was observed by Bearman (1969) and Schewe (1983). When the Reynolds number increases to 3.50×10^5, the symmetric circumferential pressure distribution reappears at some spanwise locations (at z/D=-1 and 1), as shown in Figure 2-3(c). This indicates the formation of the second separation bubble on the other side of the cylinder surface at those locations. Figure 2-3(d) shows the time-averaged surface pressure distribution at $Re=5.85\times10^5$. It is accompanied by a decrease of the minimum pressure coefficient at all spanwise locations considered (e.g. at Ring 4, from $|C_{p,min}|\approx3.0$ in Figure 2-3(c) to $|C_{p,min}|\approx2.0$ in Figure 2-3(d)).

Differences between time-averaged circumferential pressure distributions at different spanwise locations when the flow undergoes transition from TrBL0 to TrBL1 or from TrBL1 to TrBL2 regime can be seen in Figure 2-3. In Figure 2-3(b), surface pressure distribution at z/D=-10.5, 1 and 2 (locations of Rings 1, 4 and 5) show

significant asymmetry, while at z/D=-5 and -1 (locations of Rings 2 and 3), they still remain more or less symmetric. At $Re=3.50\times10^5$, as shown in Figure 2-3(c), the reappearance of symmetric pressure distribution can only be detected at z/D=-1 and 1 (locations of Rings 3 and 4). While at higher Reynolds numbers, the symmetric pressure distribution around the circumference of the cylinder more or less reoccur at all spanwise locations considered. The existence of symmetric and asymmetric circumferential pressure distributions in Figure 2-3(b) and Figure 2-3(c) suggests the co-existence of dual flow sub-regimes along the span of the cylinder in a narrow critical Reynolds number range.

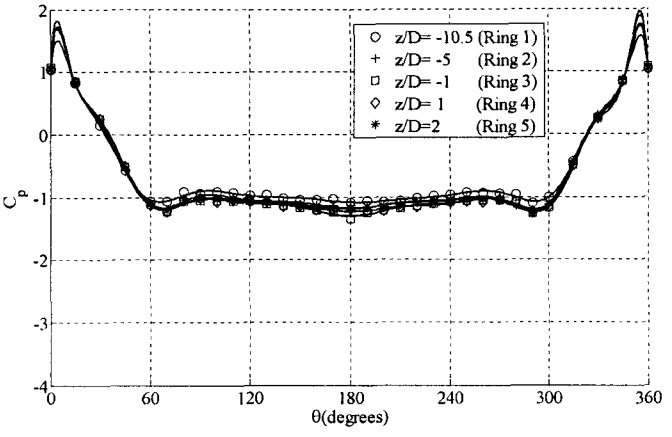

(a)Re=1.14E5

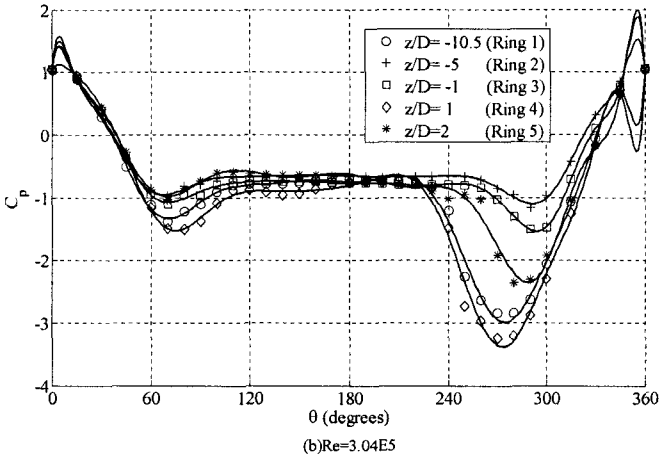

(b)Re=3.04E5

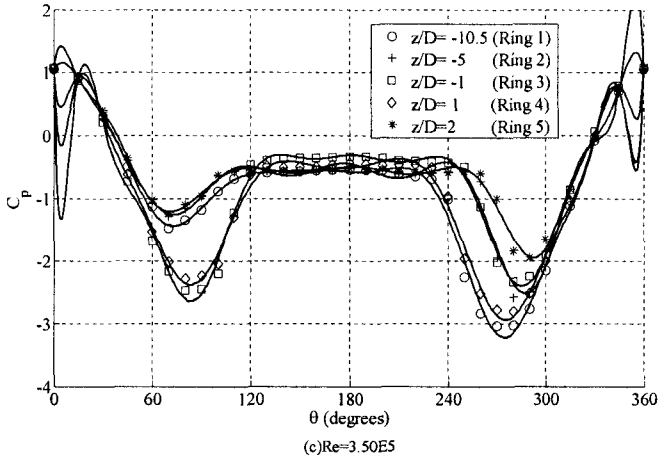

(c)Re=3.50E5

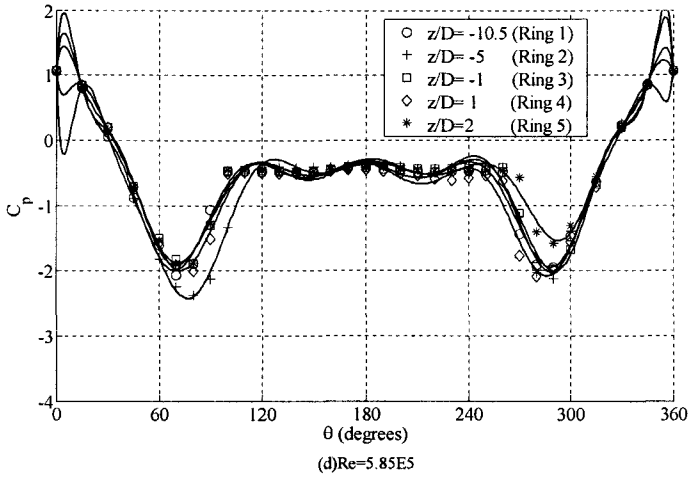

Figure 2-3-Time-averaged surface pressures of five spanwise locations at four Reynolds numbers (Note: For the purpose of deriving separation angles, curve fitting was applied to the sampled surface pressure data by 16th order polynomial. The solid lines in the figure shows the fitted curve, with details presented in Section 3.2.1)

2.3.1.2 Surface pressure contours

Surface pressure contours detected from the time-averaged pressure data are plotted in Figure 2-4. The vertical axis represents dimensionless distance from the midspan of the cylinder to the location of different rings, z/D. The horizontal axis gives the angular position in terms of the circumferential angle, θ.

Figure 2-4(a) illustrates pressure contours within the sub-critical regime at $Re=1.14\times10^5$. As expected, constant spanwise pressure patterns, as indicated by fairly straight (vertical) pressure contour lines can be observed on the surface, suggesting that the flow is primarily two-dimensional. At $Re=2.90\times10^5$, as shown in Figure 2-4(b), these pressure contours no longer present two-dimensional flow. They demonstrate cell-like patterns near the regions close to midspan where rings are more densely arranged (hence there are more data points to plot the contours). These cell-like patterns were also observed in the surface pressure contours by Higuchi et al. (1989) at a lower

Reynolds number of 1.95×10^5. In the current study, however, these cell-like structures were not observed until at a higher Reynolds number reaching 2.95×10^5. The slanted patterns and cell-like constant pressure regions, which corresponds to three-dimensionality in the flow structure, are more evident at $Re=3.33\times10^5$ (within the TrBL1 regime) as shown in Figure 2-4(c). The increase of the Reynolds number to 3.80×10^5, where the second separation bubble is formed, results in a narrower three-dimensional region as depicted in Figure 2-4(d). Further increment in Reynolds number again serves to shift the observed constant pressure cells toward the ends and consequently narrow three-dimensional flow region as shown in Figure 2-4(e). The same behavior in the surface pressure contours can be seen at the largest Reynolds number tested, 5.85×10^5 in Figure 2-4(f).

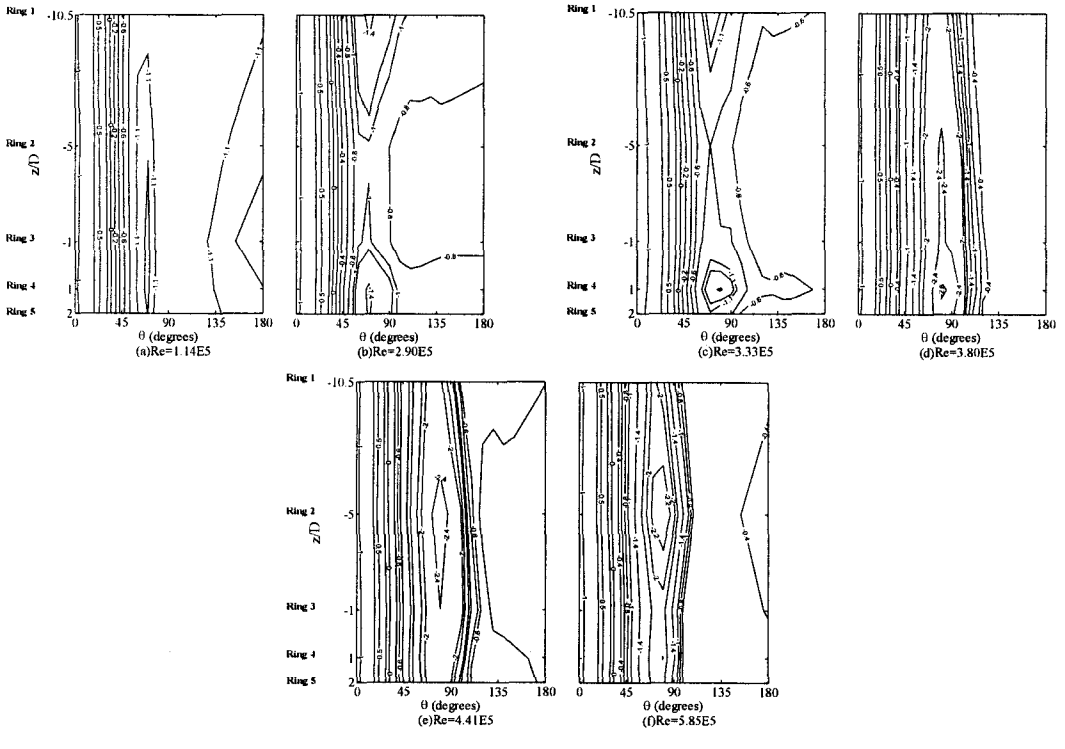

Figure 2-4- Constant pressure coefficient (C_P) contours on the surface of cylinder at six different Reynolds numbers

2.3.2 Flow separation angle

2.3.2.1 Determination of separation angle

It is now quite well known that adverse pressure gradient is the main cause of separation of flow over a body. It induces an opposite force against the motion of fluid and thus decreases the skin friction. The point where the skin friction vanishes and beyond which flow reversal occurs in a steady flow is marked as the flow separation point. In unsteady and oscillatory flow conditions such as the current study, however, different criteria have been used for the determination of the separation point. Despard and Miller (1971) proposed an empirical definition for an unsteady oscillatory separation point as the farthest upstream point within the entire cycle of oscillation, at which the wall shear-stress is non-positive. Sears and Telionis (1975) noted the lack of evidences to detect the point where wall shear-stress vanishes in unsteady oscillatory flows. Based on the above mentioned studies, Higuchi et al. (1989) indicated that both the instantaneous wall shear-stress and flow direction data are necessary for the determination of oscillatory separation points in the cases such as the flow past a circular cylinder.

The accurate definition of separation angle in unsteady flows is not the main focus of the present paper. Therefore, the instantaneous flow separation points in the current study are simply defined as the mathematical inflection point of the surface pressure curves, which are obtained by the application of curve fitting to the surface pressure data. This approach has been successfully employed earlier by Nishimura and Taniike (2001) who applied curve fitting to the instantaneous pressure data to determine the separation points within the sub-critical regime.

To obtain the time-history of separation angles, at any specific ring location, curve fitting is first applied to the surface pressure data sampled from 32 taps on the corresponding ring. Polynomial is utilized in fitting data obtained at different time instances and spanwise locations. Based on the uncertainty analysis of experimental error and curve fitting error resulted from different order of polynomials, the 16^{th} order polynomial is selected. The fitted curves of the time-averaged surface pressure data are also presented in Figure 2-3 as solid lines. Since polynomials of this order could produce local maxima and minima, it can be seen from Figure 2-3 that the pressure distribution between $\theta=0^\circ$ and $\theta=15^\circ$ and also between $\theta=345^\circ$ and $\theta=360^\circ$ could not be well represented by the polynomial curves. However, these local errors resulting from high order polynomial curve fitting, do not distort the pressure distribution in the region of interest where the flow separation is expected to occur (i.e. $60^\circ \leq \theta \leq 300^\circ$).

Separation angles on both sides of the circular cylinder are defined with respect to the side they are located and marked as left and right separation angles, θ_{sl} and θ_{sr}, as illustrated in Figure 2-5, noting that θ starts clockwise from the location of tap 17 (refer to Figure 2-2). To identify the appropriate separation point from the fitted instantaneous surface pressure curves, the following criteria have been set: (a) The first derivative of the pressure curve with respect to θ at the corresponding point must be negative (i.e. it is located in the region of adverse pressure gradient); (b) The inflection point of the fitted curve, which represents the separation point, must be located within the expected region (i.e. $60^\circ \leq \theta \leq 150^\circ$ for the left separation angle, θ_{sl}, and $210^\circ \leq \theta \leq 300^\circ$ for the right separation angle, θ_{sr}); (c) The inflection point is located just after (or before in case of the right separation angle) the minimum pressure point, beyond which the adverse

pressure gradient occurs. Following these criteria, the instantaneous separation angles are calculated and then time-averaged for further analyses.

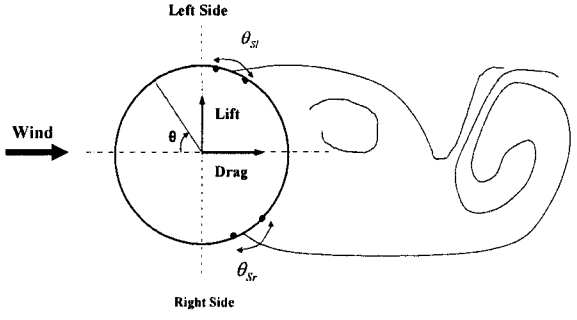

Figure 2-5- Schematic and definition of left and right separation angles with respect to the on-coming wind direction

2.3.2.2 Time-averaged separation angle

Figure 2-6 shows the variation of time-averaged left separation angle, θ_{sl}, at each considered spanwise location versus Reynolds number. The figure also includes the results of Achenbach (1968) and Tani (1964). A general trend, at which θ_{sl} slightly increases with Re can be observed in all results within the sub-critical regime. While at higher Reynolds numbers ($Re>3.5\times10^5$), when the separation bubbles form, Achenbach's (1968) results seem to overshoot and remain significantly higher than Tani's (1964) and the present results, while the latter two sets manifest better agreements.

Time-averaged separation angle calculated based on Ring 1 (z/D=-10.5) measurement experienced somewhat smoother variation with Re, i.e. the increase in the

θ_{sl} value is less than those at other spanwise locations. Since Ring 1 is the closest ring to the top end plate, with a distance of 1D, the end plate might have somewhat diminished the expected increase in θ_{sl}. Therefore, the data obtained at z/D=-10.5 (Ring 1 location) will not be considered for further analyses (conducted in Section 3.3 to 3.5). Results of other rings showed more or less the expected variation for transitions to TrBL1 and TrBL2 regimes.

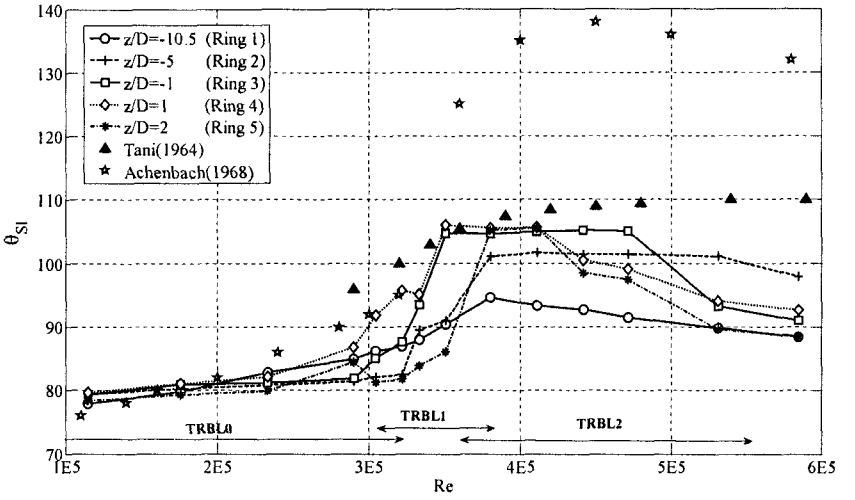

Figure 2-6 Time-averaged separation angles on the left side of the cylinder surface; compared with Achenbach's (1968) and Tani's (1964) results

It can be detected from Figure 2-6, that laminar boundary-layer separates almost uniformly along the cylinder span at $\theta_{sl}\approx78^\circ$ at $Re=1.14\times10^5$ and may rise slightly to $\theta_{sl}\approx82^\circ$ at $Re=2.33\times10^5$. Spanwise non-uniformities tend to begin around the upper limit of the TrBL0 regime, at which the spanwise cell-like structures are also observed in Figure 2-4(b), suggesting the three-dimensional nature of the surrounding flow. The transition into TrBL1 regime was first identified in Figure 2-3(b) to occur at some spanwise locations when Re reached 3.04×10^5. This transition can not be detected from

Figure 2-6 by a considerable jump in θ_{sl} values, because the asymmetric surface pressure distribution shown in Figure 2-3(b) suggests that first separation bubble forms on the right side of the cylinder. The second transition, i.e. to the TrBL2 regime is detected first in Figure 2-3(c) when $Re=3.50\times10^5$ at z/D=-1 and 1 (Rings 3 and 4) and subsequently when $Re=3.80\times10^5$ at z/D=-5 and 2 (Rings 2 and 5). This transition is accompanied by a jump of left separation angle to $100^\circ<\theta_{sl}<105^\circ$ as seen in Figure 2-6. Within TrBL2, the left separation angle gradually decreases to $89^\circ<\theta_{sl}<97^\circ$ as the Reynolds number reaches 5.85×10^5. This decrease seems to correspond to entrance into TrBL3 regime as the decrease of the minimum pressure coefficients in Figure 2-3(d) appears to support this idea.

It thus appears that the observed jumps in the variation of separation angles occur at slightly different Reynolds numbers for different spanwise locations. In other words, the surface pressure distributions shown in Figure 2-3, and the time-averaged separation angles, suggest that the respective overlaps of TrBL1 regime with TrBL0 and TrBL2 at its lower and upper limits exist, as illustrated in Figure 2-6. This seems to verify Schewe's (1983) suggestion of which the flow could be divided along the span into different sub-systems, with each of them exhibiting slightly different characteristics corresponding to the co-existence of different flow sub-regimes. In the current study, TrBL1 regime is thus considered as the Reynolds number range within which any circumferential asymmetric pressure distribution exists along the cylinder span, i.e. $3.04\times10^5<Re<3.80\times10^5$ (also see Figure 2-3).

Using flow visualization techniques, in addition to laminar separation angles, Tani (1964) also indicated the circumferential position where the transition into turbulence

occurs within the critical range, i.e. $\theta \approx 90^\circ$ for TrBL0 regime and $\theta \approx 110^\circ$ for TrBL1 and TrBL2. The reattachment of boundary layer was also reported to occur at $\theta \approx 117^\circ$ within the TrBL1 regime. Achenbach (1968) used skin friction measurement which would give the final turbulent separation point around the circular cylinder. This could be the main reason for Achenbach's (1968) θ_s values to be larger than those of Tani's (1964) and the current study within the TrBL1 and TrBL2 regimes, as observed in Figure 2-6. Despite the discrepancy with Achenbach's results (1968), the separation angles obtained in the current study exhibited all other expected features of transition into the TrBL1 and TrBL2 regimes. Therefore, they were used in the further analyses to study the three-dimensional flow structure around the circular cylinder. Comparing the current results with those of Achenbach's (1968) and Tani's (1964), it may be concluded that the proposed criteria for the detection of separation angles (i.e. curve fitting to the surface pressure data and locating inflection point of curves) have led to the determination of the laminar separation point within the TrBL1 and TrBL2 regimes.

2.3.3 Power spectra of separation angle

Power spectral analysis is conducted for the time-histories of left and right separation angles, and the resulting power spectra are presented in Figures 2-7 to 2-10, where the frequency domain, f is normalized by U/D (free stream velocity divided by cylinder diameter). Normalized frequency of vortex shedding, the dominant frequency in the power spectra where the energy is concentrated, yields the Strouhal number, $St=f_sD/U$. Also, the third axis in Figure 2-7 and Figure 2-9 represents the spanwise distance from each ring to the cylinder mid-span. The power spectra density (PSD), as shown in Figure 2-7 and Figure 2-9, is obtained from the low sampling frequency data

at Reynolds numbers of Re=1.75×10^5 to 3.33×10^5 at z/D=-5, -1, 1, 2 (Rings 2-5). High sampling frequency data set is used at higher Reynolds numbers of Re=3.50×10^5 to 5.85×10^5 at z/D=-5, 1 (Rings 2 and 4) to obtain power spectra in Figure 2-8 and Figure 2-10. The entire separation angle time-history was divided into equal segments, with Fast Fourier Transform (FFT) applied to each of them. The obtained power spectra were then averaged to represent the energy distribution at different frequencies for the flow separation angle. It was found that 64 segments worked the best, i.e., resulted in smooth variation of PSD with distinct frequency peaks. It should also be noted that to avoid aliasing frequencies in the power spectra, the expected frequency range of vortex shedding was first calculated from the universal Reynolds-Strouhal number curve (Zdravkovich, 1997). This resulted in a frequency bandwidth of 44~444Hz respectively corresponding to the lowest and highest Reynolds number tested (1.14×10^5 to 5.85×10^5). The Nyquist frequency for the two sampling rates of 400Hz and 1200Hz were respectively 200Hz and 600Hz. Therefore, for Reynolds numbers higher than 3.33×10^5 which would correspond to the expected vortex shedding frequencies larger than 190Hz, the data sampled at 1200Hz rate were used for Fast Fourier Transform.

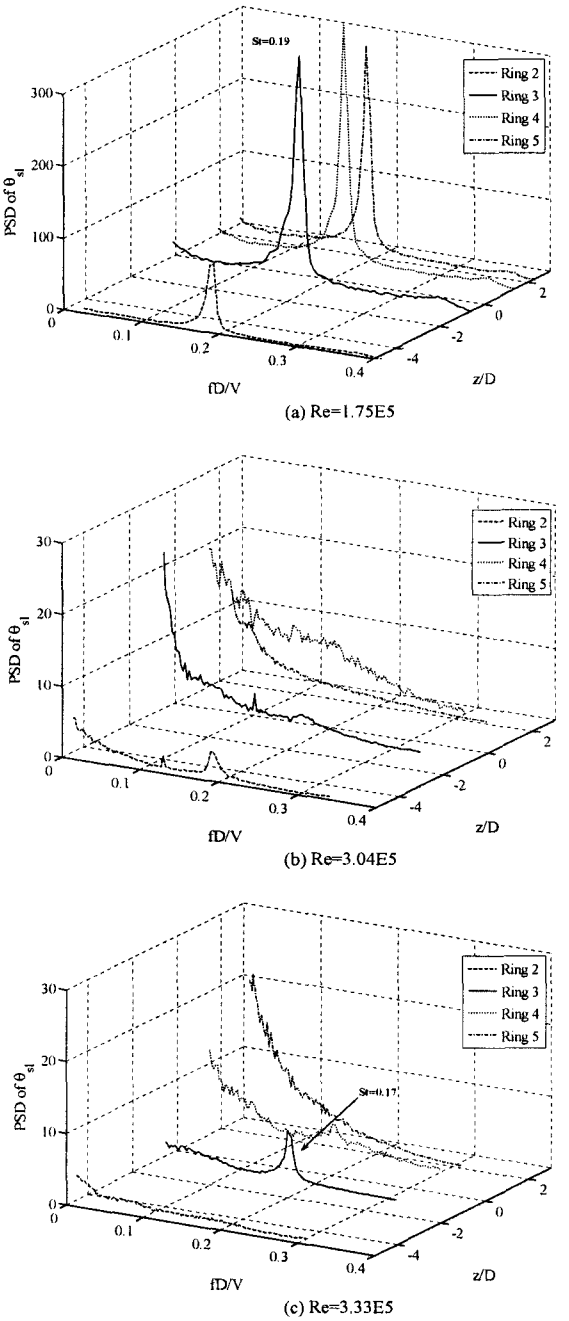

Figure 2-7- Power spectra density of left separation angle on the cylinder at (a) Re=1.75E5, (b) Re=3.04E5, (c) Re=3.33E5 at Rings 2-5, using low sampling frequency data

As shown in Figure 2-7(a) and Figure 2-9(a), left and right separation angles oscillate with very well-defined periodicity in the sub-critical regime, the dominant peaks suggest Strouhal number of 0.19 at all four spanwise locations. Another minor

peak may also be detected at 2St. The presented results are fairly consistence with other Strouhal number measurements in the sub-critical regime, such as Nishimura and Taniike (2001), who reported St=0.202 at Re=6.1×10^4, and Bearman (1969), who reported St=0.18~0.20 (using hot-wire signals) within this range. Strongly uniform distribution of separation angle PSD along the span of the cylinder highlights the two-dimensional and organized flow patterns within the sub-critical range.

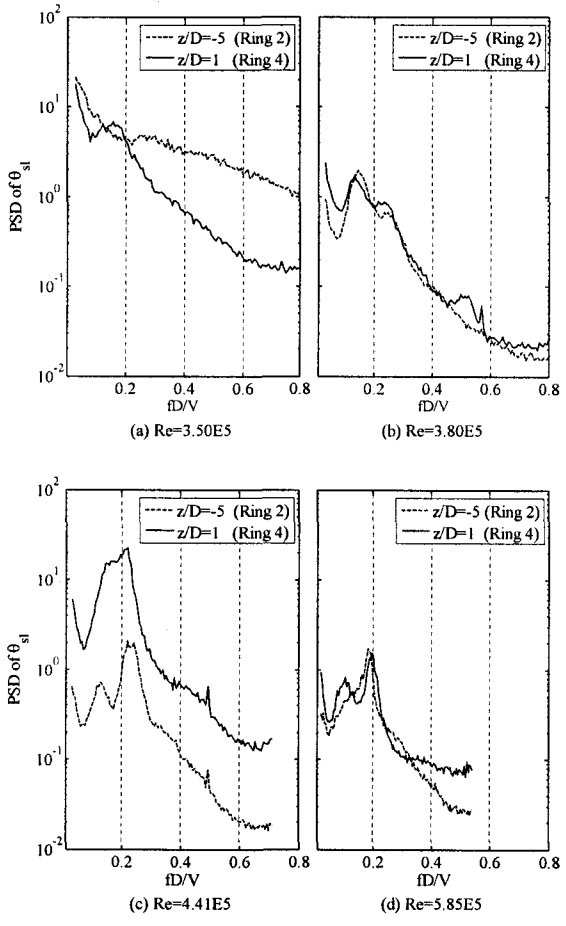

Figure 2-8- Power spectra density of left separation angle on the cylinder at (a) Re=3.50E5, (b) Re=3.80E5, (c) Re=4.41E5, (d) Re=5.85E5 at Rings 2&4, using high sampling frequency data

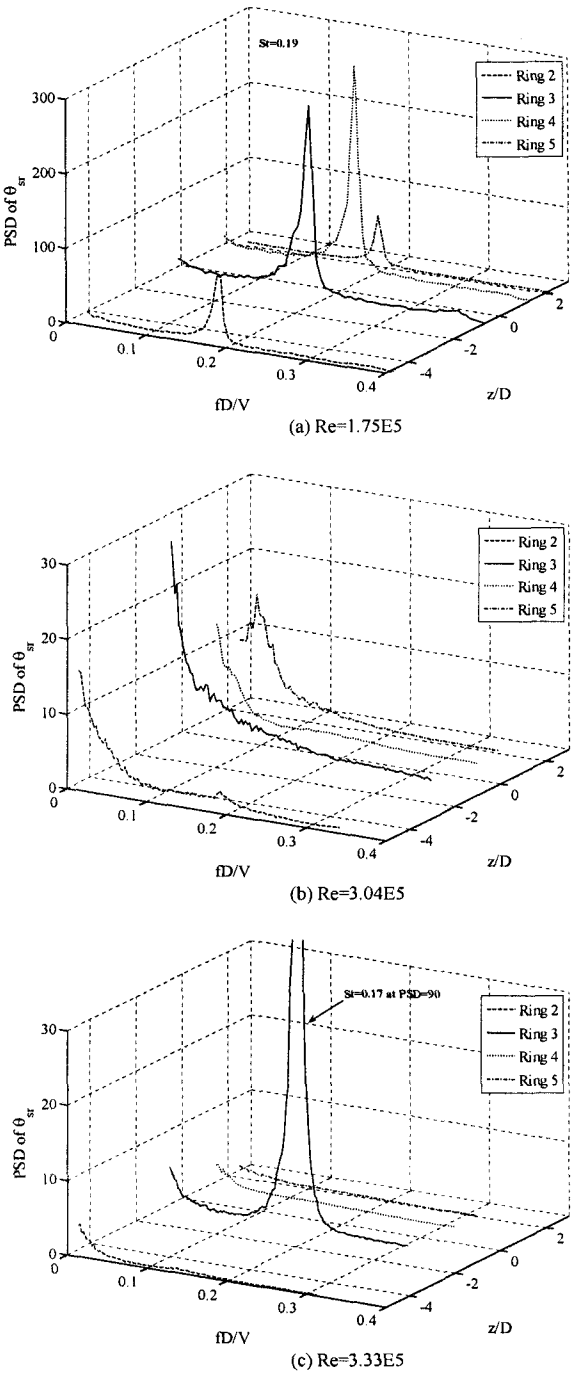

Figure 2-9- Power spectra density of right separation angle on the cylinder at (a) Re=1.75E5, (b) Re=3.04E5, (c) Re=3.33E5 at Rings 2-5, using low sampling frequency data

Entrance to TrBL1 regime is denoted by lower energy level and broader energy distribution in the power spectra (say an order of magnitude lower than that of the sub-

critical regime) and lack of spanwise uniformity comparing to the sub-critical regime, as shown in Figure 2-7(b) and Figure 2-9(b). Within the TrBL1 regime, energy is more concentrated in lower frequencies, however, minor peaks at z/D=-5 (Ring 2) can be detected at St=0.19 both in Figure 2-7(b) and Figure 2-9(b). As conceived earlier from Figure 2-3(b), at $Re=3.04\times10^5$, jump in the surface pressure coefficient values at z/D=-10.5, 1, 2 (Rings 1, 4 and 5) occurs first on the right side of the cylinder. Compared to Figure 2-9(b), relatively higher energy level shown in Figure 2-7(b) at z/D=1 and 2 (Rings 4 and 5) indicates that the formation of a single separation bubble on the cylinder surface would decrease the amount of separation angle fluctuation energy on the corresponding side more than the opposite side. In Figure 2-7(c) and Figure 2-9(c), at $Re=3.33\times10^5$, detectable peaks at slightly lower Strouhal number of 0.17 can be observed in the PSD of the left and right separation angles at z/D=-1 (Ring 3). At this Reynolds number, energy distribution in the PSD of the right separation angles show lower levels than those of the left separation angles, except at z/D=-1 (Ring 3), where a considerably higher energy level corresponding to the peak of the right separation angle PSD is observed, as can be clearly seen in Figure 2-9(c).

At higher Reynolds numbers, power spectra analysis of separation angle are conducted based on the high sampling frequency data set at z/D=-5, 1 (Rings 2 and 4) and presented in Figure 2-8 and Figure 2-10. Entrance into the TrBL2 regime at all four spanwise locations occur when Re reaches 3.80×10^5, as noted earlier. It can be observed in Figure 2-8(b) and Figure 2-10(b), this transition results in another decrease in the energy level. Within the TrBL2 regime, qualitative trends in PSD of θ_{sl} and θ_{sr} are somewhat similar, suggesting the return of circumferential symmetry, though lack

of precisely quantitative agreement between the right and left separation angle power spectra can be seen in Figure 2-8 and Figure 2-10.

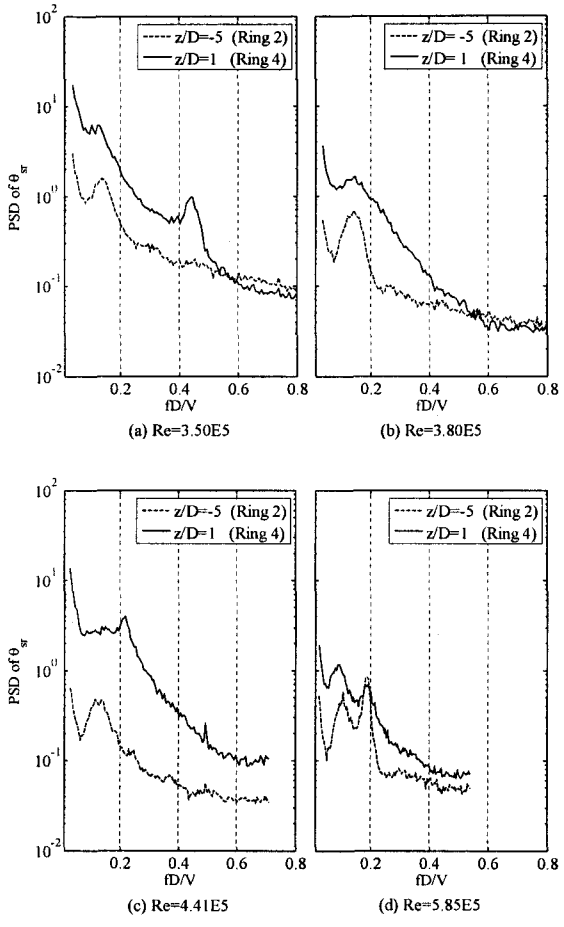

Figure 2-10- Power spectra density of right separation angle on the cylinder at (a) Re=3.50E5, (b) Re=3.80E5, (c) Re=4.41E5, (d) Re=5.85E5 at Rings 2&4, using high sampling frequency data

At Re=5.85×10^5, as depicted in Figure 2-8(d) and Figure 2-10(d), the PSD curves exhibit peaks at St=0.19 at both spanwise locations. At this Reynolds number, however, relatively better spanwise agreement could be seen in terms of power spectra energy levels and energy distribution in the frequency domain in Figures 2-8(d) and 2-10(d). It

should be noted that there is still lack of spanwise uniformity, suggesting the three-dimensionalities in the surrounding flow structure.

2.3.4 Fluctuating flow characteristics

Standard deviation of the fluctuation of the left and right separation angles at z/D=-5, -1, 1, 2 (Rings 2-5) versus Reynolds number are presented in Figure 2-11. A general trend, of which the fluctuation amplitude of the separation angles (θ'_{sl} and θ'_{sr}) decreases by increasing Reynolds number from the TrBL0 regime up to TrBL2 regime, can be seen in Figure 2-11. The transition from TrBL0 into TrBL1 regime is accompanied by a decrease in the amplitude of fluctuations of the right separation angle at z/D=-1, 1, 2 (Rings 3-5), shown in Figure 2-11(b), at the corresponding transition Reynolds number within the overlap range of TrBL1 (i.e. $3.04\times10^5 \leq Re \leq 3.33\times10^5$). The same phenomenon, however at a lower degree, can be observed in Figure 2-11(a) before the transition into TrBL2 regime. Based on the presented results, it might be concluded that the fluctuation amplitude of separation angles increases just before each transition into both TrBL1 and TrBL2 regimes and suddenly drops afterwards (i.e. θ'_{sr} in case of transition into TrBL1 regime and θ'_{sl} when transition from TrBL1 into TrBL2). At higher Reynolds number within the TrBL2 regime, the results show much smaller fluctuation amplitude of separation angles on both sides of the cylinder. This is probably related to the intermittent low amplitude movements of separation-reattachment bubble as indicated by Higuchi et al. (1989).

Standard deviations of surface pressure at four circumferential locations (θ=60°, 90°, 110°, 150°) are normalized by their mean values (P'/P_{mean}) and plotted against Reynolds number, as illustrated in Figure 2-12. At θ=60°, as portrayed in Figure 2-

12(a), where the boundary layer is expected to be attached and laminar, strong spanwise agreement can be seen among the results at all spanwise locations except within the Re range of 3.04×10^5 to 3.80×10^5, which was previously considered to be TrBL1 regime. This indicates that transition into TrBL1 regime could be detected from the upstream of separation region in terms of disruption of spanwise uniformity of the flow. Fluctuating surface pressures at $\theta=90^\circ$ are presented in Figure 2-12(b), where the same behavior as that at $\theta=60^\circ$ can be seen, except with higher amplitude and slightly more spanwise non-uniformity.

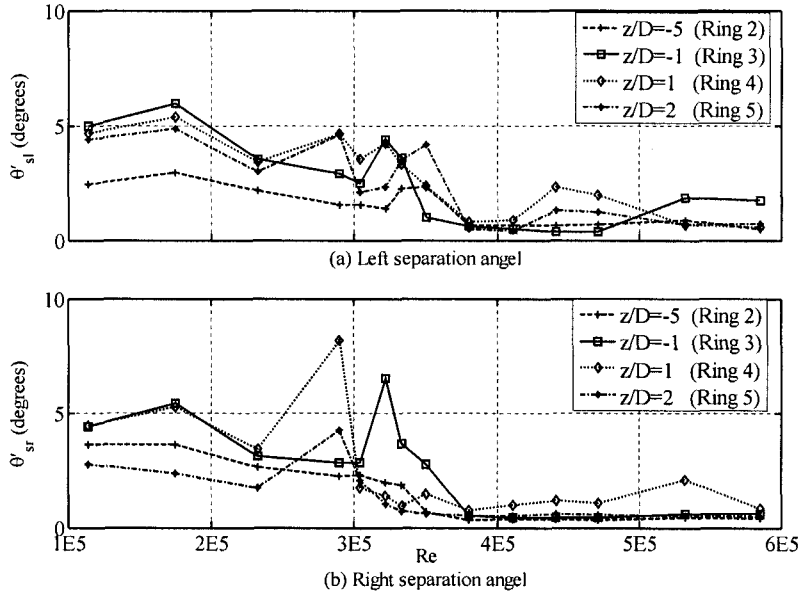

Figure 2-11 Standard deviations of fluctuations of (a) left separation angle, (b) right separation angle for the studied Reynolds number range

In Figure 2-12(c), at $\theta=110^\circ$, where the flow state is expected to be turbulent in the sub-critical range, there is still fairly good agreement among the results of all four spanwise locations for Re up to 2.33×10^5. The largest discrepancy among the results of four rings can be seen at Reynolds numbers corresponding to the TrBL1 and TrBL2

regimes. Considering the time-averaged separation angle results from Figure 2-6, this circumferential position (θ=110°) is most likely located in the separation bubble and highly three-dimensional flow structure could be detected around its neighborhood. Fluctuation amplitude of surface pressure at θ=150° is presented in Figure 2-12(d). Since it is located at the leeward side of the cylinder where the wake is present, the state of flow is expected to be turbulent over the entire tested Reynolds number range. Compared to Figure 2-12(c), spanwise uniformity appears to be increased. Transitions to the TrBL1 and TrBL2 regimes, however, are not clearly distinguishable in Figure 2-12(c) and 12(d) in terms of increase or decrease in the fluctuation amplitude like in Figures 2-12(a) to 2-12(b), except for those at z/D=-1 (Ring 3).

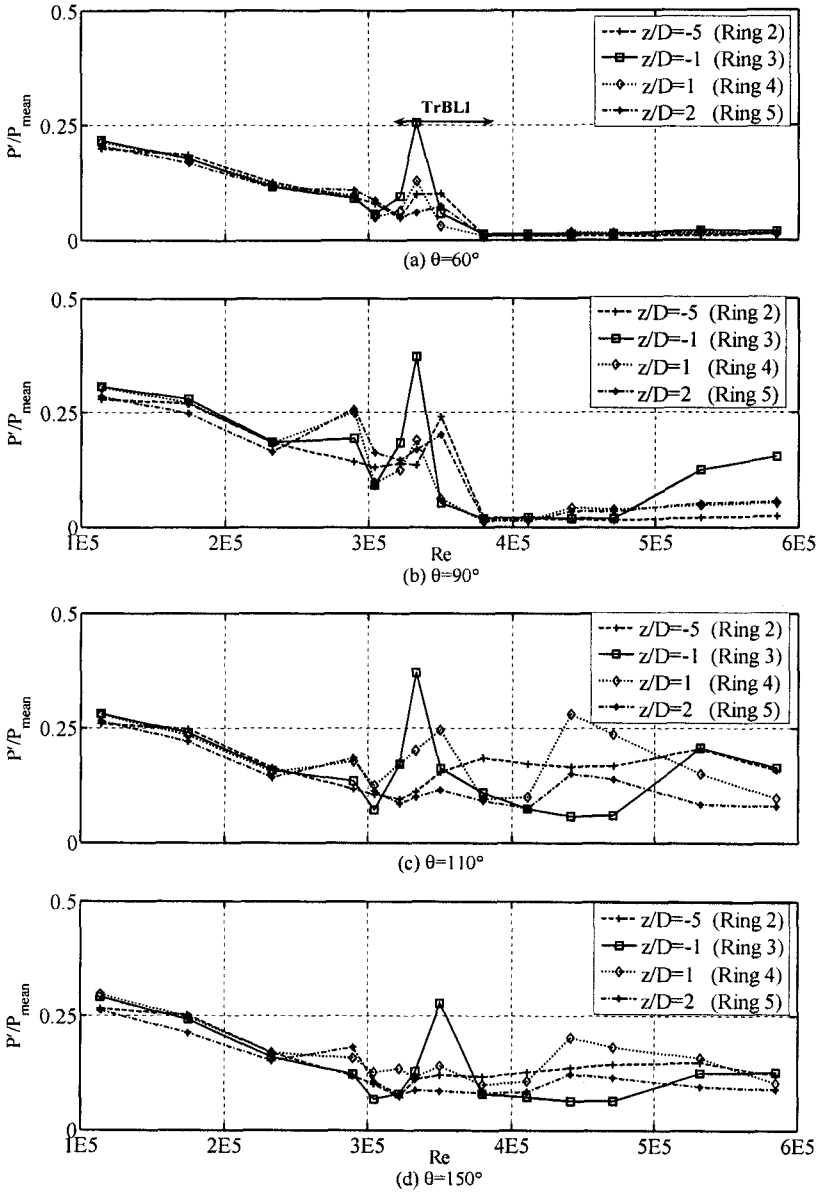

Figure 2-12- Standard deviations of fluctuations of surface pressures at four angular locations, (a) θ=60°, (b) θ=90°, (c) θ=110°, (d) θ=150°; normalized with their mean values for the studied Reynolds number range.

2.3.5 Spanwise correlations

Correlation coefficients of fluctuating separation angles, lift and drag forces, and surface pressures, are calculated and shown in Figures 2-13 to 2-15. The dimensionless distances between different pairs of rings used in the correlation analysis are listed in

Table 2-2. Figure 2-13 shows the correlation coefficients of the separation angles at nine different Reynolds numbers within the tested range. The correlations coefficients decrease with the increase of spanwise distance at $Re=1.75\times10^5$ within the TrBL0 regime. The same pattern can be observed in Figure 2-14 and Figure 2-15 at $Re=1.75\times10^5$, for the variation of correlation coefficient of lift and drag, and surface pressure at $\theta=110^\circ$ and $\theta=150^\circ$.

Table 2-2 Dimensionless distances between different pairs of rings

Pair of rings (i,j)	2,5	2,4	2,3	3,5	3,4	4,5
Dimensionless spanwise distance z(i,j)/D	7	6	4	3	2	1

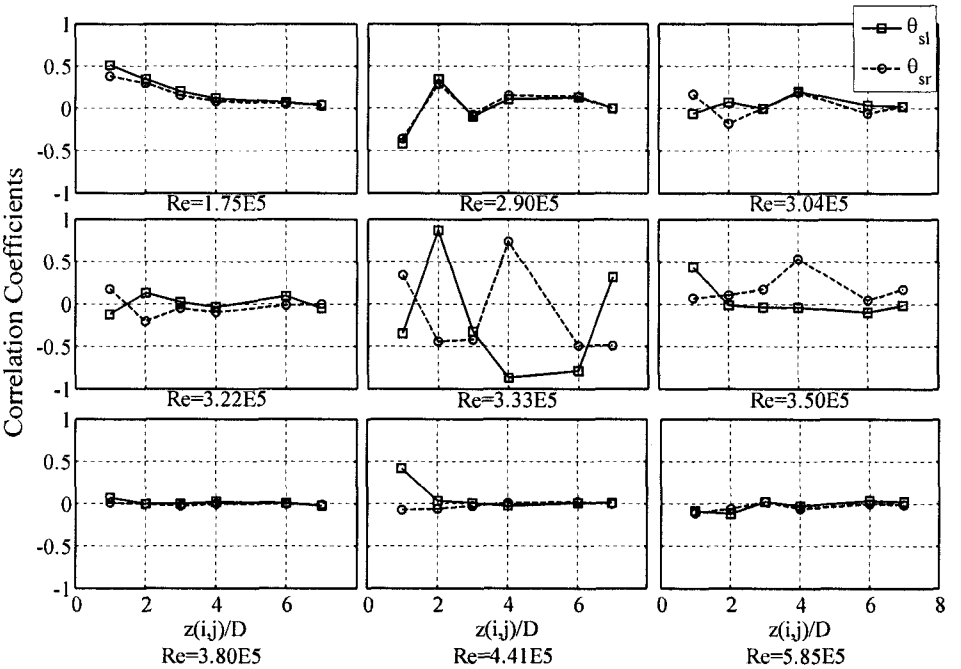

Figure 2-13- Correlation coefficients of left and right separation angles

Negative correlation coefficients is first identified at $Re=2.90\times10^5$. It is then followed by very low correlation coefficients at $Re=3.04\times10^5$ and $Re=3.22\times10^5$ after

the transition into TrBL1 regime, as can be observed in Figures 2-13 to 2-15. Different patterns of correlation coefficient against spanwise distance for Re=3.04~3.33×10^5, as illustrated in Figure 2-13, indicates that within TrBL1 regime, spanwise distances of higher correlation coefficient tend to vary, which suggests that different flow structures exist along the cylinder span. Also, the in-phase and out-of-phase correlation coefficients of left and right separation angles between the same spanwise distances suggest that the separation lines on the left and right side of the cylinder surface have different patterns. This is particularly considerable at Re=3.33×10^5.

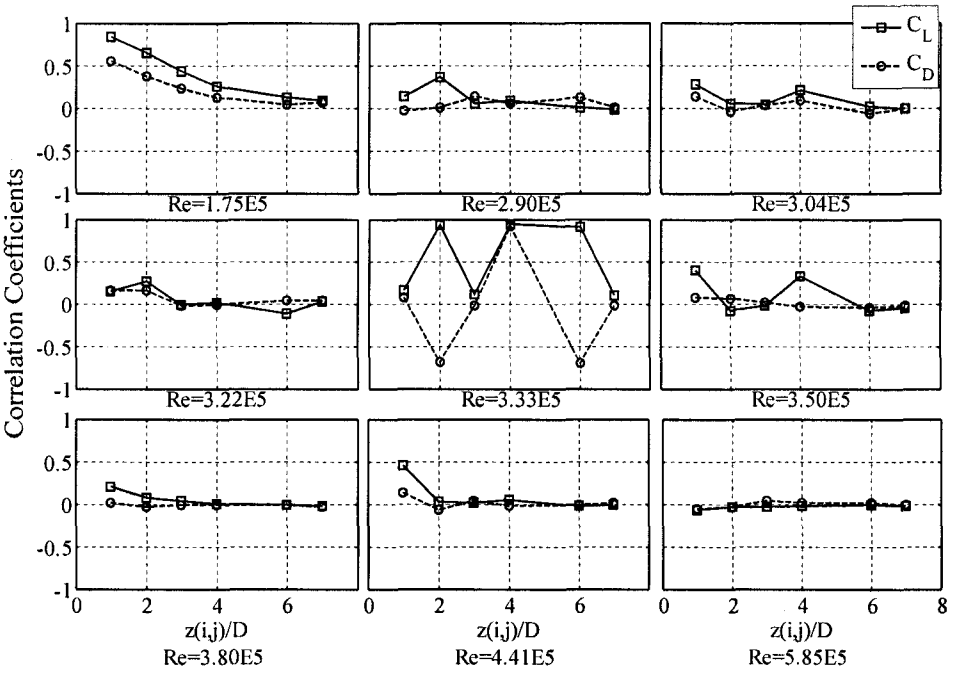

Figure 2-14- Correlation coefficients of lift and drag coefficients

Within TrBL1 regime, at Re=3.33×10^5, very large correlation coefficients, whether positive or negative, exist. This suggests very well-structured flow patterns around the cylinder at this Reynolds number. Very large in-phase correlation coefficients of the left separation angle, lift force, and surface pressures can be seen for spanwise distance

of 2D, while right separation angle and drag force exhibit strong out-of-phase fluctuations for the same spanwise distance. It can also be seen in Figures 2-14 and 2-15 that strong in-phase or out-of-phase correlation exists for spanwise distances of 2D, 4D and 6D; while for distances of 1D, 3D and 7D, almost zero correlation can be observed in the figures. It should be noted that there are no testing data available to conduct spatial correlation analysis for spanwise distance of 5D in the current study. The observed spanwise correlations suggest a size of the spanwise structures to be a multiple of two cylinder diameters at $Re=3.33\times10^5$ within the TrBL1 regime. The spanwise regions of strong in-phase correlation have a size of 2D for lift force and 4D for drag force. At $Re=3.33\times10^5$, the positive lift correlation coefficients suggests that there could be large overall instantaneous lift force acting on the cylinder, which is induced by the collaboration of the individual contributions from different spanwise structures. However, the summation of drag force correlation coefficients for different spanwise distances in Figure 2-14 yields to almost zero, indicating that the overall drag force on the circular cylinder does not experience large instantaneous values, but rather relatively small fluctuation amplitudes.

The second transition occurs when reaching $Re=3.80\times10^5$, which is the transition into TrBL2 regime marked by the formation of the second separation bubble. As observed from the third row of Figures 2-13 to 2-15, the spanwise correlations of the fluctuating flow characteristics are almost lost, except for left separation angles, lift forces, and surface pressure at $Re=4.41\times10^5$ when the two considered spanwise locations are separated only by one cylinder diameter. This is probably caused by the formation of the second separation bubble on the left side of the cylinder surface which

leads to intermittent fluctuations in the flow characteristics and thus, very poor correlation strength.

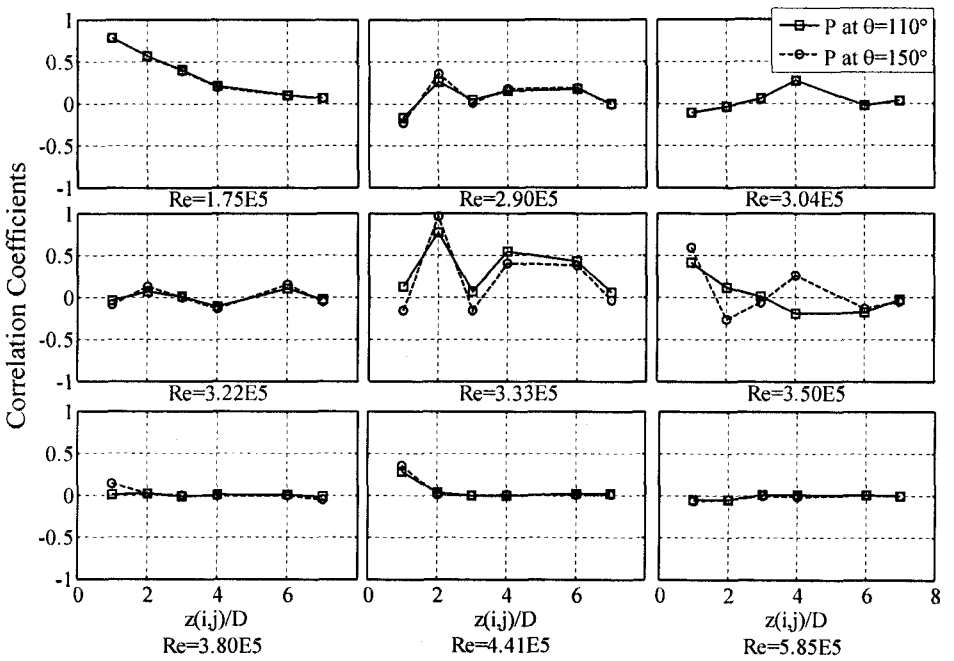

Figure 2-15- Correlation coefficients of surface pressure at θ=110° and θ=150°

2.3.6 Further discussion of spatial flow structure

It is now quite well-known that flow in the critical Reynolds number regime is extremely sensitive to flow conditions and experiment setup (Bearman, 1969). Different sub-regimes may emerge or disappear at different Re values, due to variation in experimental details such as free stream turbulence and model surface roughness. It should also be noted that by monitoring different spanwise locations, the Reynolds number range of TrBL1 regime and the overlap ranges could vary. This somewhat explains the differences among the results of different researchers within the critical regime.

As discussed earlier (see Section 3.2.3 and 3.3), an increase-decrease manner in the fluctuating characteristics amplitudes (Figures 2-11 and 2-12) and the energy levels in the power spectra of fluctuating separation angles (Figures 2-7 to 2-10) is observed just before and after each transition to TrBL1 and TrBL2 regimes. It is proposed that within the TrBL1 regime, by increasing Reynolds number, the flow regains energy while the circumferential location at which transition of boundary-layer into turbulent state occurs, is kept more or less constant within the separation bubble (e.g. as suggested by Tani, 1964, to happen at θ=110°). It leads to a better organized flow structure represented by relatively higher energy levels of PSD, fluctuation amplitudes and spanwise correlations (see Figures 2-7, 2-9, 2-11, 2-12 and 2-13 to 2-15).

In addition, stable spanwise structures have been reported in a few literatures. Humphreys (1960) identified it by using silk threads attached to the stagnation point at Reynolds numbers as low as 10^5. At the supercritical regime, Korotkin (1976) found some spanwise non-uniformity just before and in the region of separation. Further experiments by Dallman and Schewe (1987) using oil-film flow visualization, pressure measurements by Higuchi et al. (1989), and more recent work by Gölling (2004), showed cell-like patterns in flow structure with different cell sizes of 1.5 to 3.3 times of cylinder diameters in different studies. In the current study, the surface pressure contours presented in Figure 2-4 show no more traces of the two-dimensional constant pressure patterns in the critical Reynolds number regime but rather, cell-like constant pressure regions surrounded by wave-shaped contours. These cell-like structures are observed to form mostly within the circumferential regions between θ=60° to θ=100° and have relatively lower pressure at the center of the cell. A very small region of

favorable pressure gradient (as can be seen in Figure 2-4) within these cell-like patterns decreases the opposite force against the boundary-layer motion and thus delays the flow separation. As can be seen in Figures 2-4 and 2-6, at spanwise locations and Reynolds numbers which correspond to observed cell-like structures, flow separation is slightly delayed.

Within the sub-critical regime, the spanwise time-averaged separation angles (Figure 2-6) and their amplitude of fluctuation (Figures 2-11 and 2-12) are detected to be more or less constant. Considering the correlation coefficients in the sub-critical regime ($Re=1.75\times10^5$ in Figures 2-13 to 2-15), it implies that the separation lines along the cylinder span in the sub-critical regime are straight lines, or wave-shaped with very large wavelength, oscillating around their time-averaged values with almost the same amplitudes.

The observed three-dimensionalities in the flow within TrBL1 regime can also be discussed on the basis of the fluctuating component of surface pressures (Figure 2-12). Transition into TrBL1 regime could be characterized at all angular positions considered ($\theta=60^\circ$, 90°, 110°, and 150°) by the presence of spanwise non-uniformity in the fluctuating component of surface pressure. Even at the upstream region of $\theta=60^\circ$, where the boundary layer is expected to be attached and laminar, the spanwise non-uniformity can be observed within the TrBL1 regime. This implies that strong three-dimensional flow structure around the circular cylinder in this range is associated with different circumferentially symmetric or asymmetric flow structures along the span of circular cylinder. Consequently, it could be observed that a large circumferential area of the cylinder is affected in the TrBL1 regime in terms of disruption of spanwise uniformity,

while in the TrBL2 regime, the lack of spanwise uniformity could be seen in a narrower circumferential area. However, this effect only lasts to the upper limit of the TrBL1 regime. Another three-dimensionality in the flow structure can be detected from the surface pressure fluctuation amplitude at θ=110° and θ=150° within the TrBL1 and TrBL2 regimes (in Figures 2-12(c) and 2-12(d)). Within this circumferential range, the largest spanwise non-uniformities are seen at θ=110°, where it is expected to be located within the separation bubble. This effect which endures within the TrBL2 regime indicates a different type of three-dimensionalities. It was suggested by Higuchi et al. (1989) that the interactions of the separation-reattachment bubble that involves intermittent movement of the separation angles, has a great three-dimensional effect along the cylinder span. This effect is detected throughout Figures 2-7 to 2-10 and Figures 2-11 and 2-12 as long as separation bubbles exist on the cylinder surface (i.e. within TrBL1 and TrBL2 regimes).

2.4 Conclusions

Spatial structure of flow past a circular cylinder placed normal to the on-coming flow in the critical Reynolds number regime is investigated based on a set of wind tunnel experimental data. Instantaneous surface pressures sampled at five different locations along the cylinder span reveal the existence of the spanwise three-dimensional flow patterns in terms of cell-like structures at Reynolds numbers larger than 2.90×10^5. The following main findings were obtained:

- Two regions of overlap were found at both upper and lower limits of TrBL1 regime where the characteristics of dual flow sub-regimes were observed along the span of circular cylinder.

- The three-dimensional structure of flow within the TrBL1 regime is found to be associated with different circumferentially asymmetric flow patterns along the cylinder span, in addition to the effect of intermittent motions within the laminar separation bubble.

- The relatively strong spanwise correlation and hence organized flow structure, is observed before the transitions into the TrBL1 and TrBL2 regimes. Both transitions are marked with disruption of these organized flow structures.

- Large positive, spanwise lift correlation coefficients at $Re=3.33\times10^5$ implies that greater overall instantaneous lift force could be induced on the cylinder because of the collaboration of different spanwise sub-systems, which might potentially cause unstable flow-induced vibration.

- Size of the spanwise sub-systems with in-phase fluctuations is found to be two cylinder diameters for lift force and four cylinder diameters for drag force.

References

Achenbach, E., 1968. Distribution of local pressure and skin friction around a circular cylinder in cross-flow up to $Re=5\times10^6$. J. Fluid Mech., 34(4), 625-639.

Batham, J. P., 1972. Pressure distribution on circular cylinders at critical Reynolds numbers. J. Fluid Mech. 57, 209-228.

Bearman, P.W., 1969. On vortex shedding from a circular cylinder in the critical Reynolds number regime. J. Fluid Mech. 37, 577-585.

Cheng, S., Tanaka, H., 2005. Correlation of aerodynamic forces on an inclined circular cylinder. Wind and Structures an Int. J. 8(2), 135-146.

Dallman, U., and Schewe, G., 1987. On topological changes of separating flow structures of transition Reynolds numbers. Proceedings of AIAA '19 Fluid Dynamics, Plasma Dynamics and Lasers Conference, Honolulu, Hawaii, July.

Despard, R. A., Miller, J. A., 1971. Separation in oscillating boundary layer flows. J. Fluid Mech. 47, 21-31.

Fage, A., 1928. The air flow around circular cylinder in the region where boundary layer separates from the surface. (British) Aero. Res. Coun. Report & Memo. 1179.

Farell, C., and Blessman, J., 1983. On critical flow around smooth circular cylinders. J. Fluid Mech. 136, 375-401.

Gölling, B., 2004. Three-dimensional vortex flow of a circular cylinder. Proceedings of the IUTAM Symposium on One Hundred Years of Boundary Layer Research, DLR-Göttingen. Germany, August.

Higuchi, H., Kim, H.J., and Farell, C., 1989. On flow separation and reattachment around a circular cylinder at critical Reynolds numbers. J. Fluid Mech. 200, 149-171.

Humphreys, J. S., 1960. On a circular cylinder in a steady wind at transition Reynolds numbers. J. Fluid Mech. 9, 603-612.

Korotkin, A.I., 1976. The three dimensionality of the flow transverse to a circular cylinder. Fluid Mechanics-Soviet Research, Vol. 5, No. 2, 96-103.

Nishimura, H., and Taniike, Y., 2001. Aerodynamic characteristics of fluctuating forces on a circular cylinder. J. Wind Eng. and Ind. Aerodyn. 89, 713-723.

Norberg, C., 2001. Flow around a circular cylinder: Aspects of fluctuating lift. J. Fluid and Struc. 15, 459-469.

Norberg, C., 2003. Fluctuating lift on a circular cylinder: Review and new measurements. J. Fluid and Struc. 17, 57-96.

Roshko, A., 1954. On the development of turbulent wakes from vortex streets. NACA Report No., TR1191.

Roshko, A., 1961. Experiments on the flow past a circular cylinder at very high Reynolds number. J. Fluid Mech. 10, 345-356.

Roshko, A., 1993. Perspectives of bluff body aerodynamics. J. Wind Eng. and Ind. Aerodyn. 49, 79-100.

Schewe, G., 1983. On the force fluctuations acting on a circular cylinder in cross-flow sub-critical up to transcritical Reynolds numbers. J. Fluid Mech. 133, 265-285.

Sears, W. R., and Telionis, D. P., 1975. Boundary layer separation in unsteady flow. SIAM J. Appl. Maths. 28, 215-235.

Simiu, E., Scanlan, R. H., 1996. Wind Effects on Structures, an Introduction to Wind Engineering, John Wiley & Sons.

Slaouti, A., and Gerrard, J. H., 1980. An experimental investigation of the end effects on the wake of a circular cylinder towed through water at low Reynolds number. J. Fluid Mech. 112, 297-314.

Tani, I., 1964. Low speed flows Involving bubble separations. Prog. Aeronautical Science. 5, 70-90.

Williamson, C. H. K., 1997. Advances in our understanding of vortex dynamics in bluff body wakes. J. of wind Eng. And Ind. Aerodyn. 69-71, 3-32.

Zdravkovich, M.M., 1997. Flow around circular cylinders, Fundamentals, Vol. 1, University Press, Oxford, England.

Chapter 3

Some insight into the wind-induced phenomena of stay cables in the context of rigid static inclined circular cylinder

3.1 Introduction

For over a century, flow past a circular cylinder has been extensively studied because of its association with numerous important phenomena. It has many direct engineering applications, such as effects of wind past stay cables on cable-stayed bridges and ocean current past marine guy cables. Besides, it is extremely rich of fundamental fluid dynamics phenomena which are yet to be uncovered. A good appreciation of physics behind the phenomenon is a priori to unveiling the mechanisms associated with a broad range of flow-induced structural vibration problems. When flow passes a structure, various flow-induced vibration phenomena could occur due to interaction between the structure and the passing flow. The wind-induced vibrations of bridge stay cables reported from many bridge sites in recent years is a typical example (Hikami and Shiraishi, 1988; Irwin et al, 1999; Main and Jones, 2001; Bosch, 2006). In addition, it has been noticed that when a cylinder-like structure has different orientations with respect to the oncoming flow direction, flow-induced vibration of the structure would exhibit different response characteristics. As a decent priori for investigating such phenomena, comprehensive reviews by Simiu and Scanlan (1996) on

the wind-structure interaction, by Zdravkovich (1997) on the aspects of cross-flow past circular cylinders, and by Norberg (2003) on fluctuating lift force aspects could be used.

In the case of an inclined circular cylinder in uniform flow, the flow direction is no longer perpendicular to the cylinder axis. The relative angle ϕ between the cylinder axis and the wind direction is determined by two independent orientation angles, i.e. the inclination angle α, and the yaw angle β by Equation (3-1). As portrayed in Figure 3-1(a), the inclination angle α is the angle between the cylinder axis and its horizontal projection, whereas the yaw angle β is the angle between the horizontal projection of the cylinder axis and the mean flow direction.

$$\cos\phi = \cos\alpha \cdot \cos\beta \tag{3-1}$$

In such case, the effect of wind-cylinder relative angle on the features of flow characteristics around the inclined circular cylinder and vortex shedding in the wake becomes an important issue. This is somewhat explained by the so called Independence Principle (after Hoerner, 1965) which states that flow past an inclined circular cylinder could be considered as quasi-two dimensional. This means that the flow characteristics could be detected based on cross-flow assumptions using only the normal component of flow to the cylinder axis. The applicable ranges of Reynolds number and yaw angle of this principle is the main reason of existing discrepancies in different studies. The breakdown of Independence Principle in the subcritical Re range is reported by a few investigators, including Van Atta (1968), Ramberg (1983) and Hayashi and Kawamura (1995), when the flow deviates from normal direction. The breakdown of the

Independence Principle was investigated by Marshal (2003) and Snarsky (2004) within the subcritical Re range. Two possible mechanisms were proposed for the breakdown of this principle by Marshal (2003). The first one was due to the Kelvin-Helmholtz instability in the near-wake. The second possible mechanism, i.e., the instability of the downstream Karman vortices, was proposed to be due to the axial velocity deficit in the vortex cores. Snarski (2004) introduced three different flow regimes which could be altered by changing the yaw angle while having no inclination angle. The first regime (for β=60°~90°) was characterized by the same vortex shedding features as those in the cross-flow case, which, somehow could be detected by the Independence Principle. The second regime (for β=30°~60°) was featured by broadband high-level energy spectra corresponding to a fully separated (turbulent) flow behind the cylinder. The third regime (β=0°~30°) was essentially controlled by axial boundary layer characteristics.

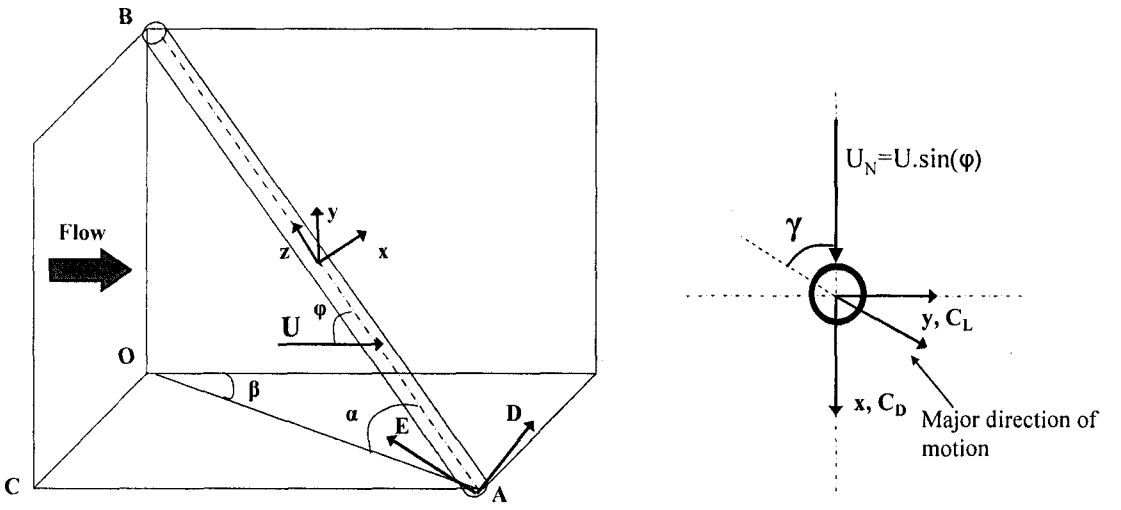

a) Definition of cylinder orientation angles

b) Major direction of motion

Figure 3-1- The angle definitions and directions of motion in the normal plane

Most previous studies on flow past inclined circular cylinders in the critical regime were focused on its engineering applications. In particular, the aerodynamic characteristics of cables on cable-stayed bridges, is a very common scenario. Various wind-induced vibration phenomena have been observed either on bridge sites or in wind tunnel tests, such as divergent type of motion (Miyata et al., 1994; Honda et al., 1995; Matsumoto et al., 1995; Matsumoto, 1998; Cheng et al., 2008a), and limited-amplitude high-speed vortex induced vibration (Matsumoto, 1998; Matsumoto et al., 1999 & 2007a; Cheng et al. 2008a). Shirakashi et al. (1986) were perhaps the first who noted the role of axial flow along an inclined circular cylinder model on disturbing regular Karman vortex shedding. It was subsequently confirmed by Mastsumoto et al. (1990). They also proposed that the role of the secondary axial flow in aerodynamic excitation of cylinder model was similar to an "air-curtain". It would prevent the inner-circulatory flow on both sides of the cylinder to interact. Thus, it could result in higher oscillatory aerodynamic forces and consequently, violent vibration of inclined cylinder model. Later, it was also noted (Matsumoto, 1998; Matsumoto, et al., 1999) that the interaction between conventional "Karman vortex shedding" and the so-called axial vortex shedding, with the frequency of the latter being about one-third of the former. This implied that the cylinder response would be amplified when the axial vortex shed once every three Karman vortices from both sides of the cylinder model. In their persisting effort on revealing mechanisms of wind-induced inclined cable vibrations, they (Matsumoto et al., 2007a & 2007b) also pointed out the impact of mitigating Karman vortex shedding on the onset of self-excited cable vibrations. Based on such

effect, it was concluded that the secondary axial flow could be fundamental to the vibration mechanism of inclined cables.

On the other hand, in their efforts to reveal the mechanisms of divergent type response of inclined and/or yawed cable, Matsumoto (1998) proposed one possible mechanism to be the combined effect of wind and rain. Because of the rain and hence the formation of upper water-rivulet on the surface of the model, geometrical imperfection could exist which would lead to divergent cable response observed in field and wind-tunnel tests. Matsumoto et al (2007a & 2007b) also proposed a division of galloping response as quasi-steady galloping, which corresponded to negative lift slope, and unsteady galloping, which was mostly non-divergent type and in relation to mitigation of Karman vortex shedding.

The divergent motion in the absence of rain was observed in a few studies such as by Saito et al. (1994) and Honda et al. (1995) in the subcritical Re regime; while by Miyata et al. (1994) and Cheng et al. (2005, 2008a, 2008b) in the transition and critical Re regime. In a series of dynamic and static wind tunnel tests, Cheng et al. (2005, 2008a, 2008b) observed both limited-amplitude high-speed vortex excitation and divergent motion on a dry inclined and yawed circular cylinder model. They noted that the possible mechanism for the latter phenomenon could be explained similarly by the classical Den Hartog criterion for iced-cable galloping (Cheng et al. 2008b). Further, it was pointed out that the flow within the critical Reynolds number regime was spatially better-correlated (Cheng and Tanaka, 2005). This was also observed in the cross-flow case (Raeesi et al., 2008) which would correspond to larger unsteady aerodynamic forces acting on the cylinder.

It is obvious from the above reviewed literatures that there were only a few studies dedicated to revealing the physics lying behind various flow-induced inclined and/or yawed circular cylinder vibration phenomena and the impact of critical Reynolds number on the flow pattern surrounding an inclined and/or yawed circular cylinder. In fact, most of the fundamental studies on this issue were conducted within the subcritical Reynolds number range. It seems that there is a serious lack of studies on flow past inclined-yawed circular cylinder within the critical regime from a fundamental fluid dynamics framework.

3.2 Experimental details and remarks from an earlier study

A series of dynamic and static tests were conducted at National Research Council of Canada by one of the co-authors (Cheng and Tanaka, 2005; Cheng et al., 2008a). The key motivation for this set of experimental work was to investigate the possible mechanisms behind the wind-induced vibration of bridge stay cables. The experimental setup of dynamic and static tests was described in details by Cheng et al. (2008a). The testing conditions are summarized in Table 3-1. In both tests, despite the size limitations of wind tunnel facilities and the difference in model support conditions, the relative angle ϕ between the model axis and the wind direction, and the model motion direction were kept consistent in the dynamic and static tests, as well as that in the simulated full-scale case. Direction of motion and positive lift and drag forces in the plane normal to the cylinder axis are shown in Figure 3-1(b), where γ is the angle between the major direction of cable motion and the wind velocity component U_N normal to cable axis. It is a common practice to decompose the response of bridge stay

cables into in-plane and out-of-plane components. The in-plane motion occurs in the plane of cable axis and its horizontal projection and normal to the cable axis, i.e. coincides with vector AD in Figure 3-1(a). The out-of-plane component, however, is normal to the cable plane. It is represented by vector AE in Figure 3-1(a) which is normal to plane BOA. The in-plane and out-of-plane terms will be used in the present paper to address the two components of cable response in the plane normal to its axis. If wind blows along an inclined but non-yawed cable (i.e. $\alpha \neq 0°$, $\beta = 0°$), the major direction of response is out-of-plane (i.e. coincides with direction of lift force) and thus $\gamma = 90°$. When wind is skewed to the cable (i.e. $\alpha \neq 0°$, $\beta \neq 0°$), however, the out-of-plane direction (across-wind) is no longer perpendicular to U_N. Details of the transformation of full-scale cable orientations to wind tunnel model setup are fully explained by Cheng et al. (2008a & 2008b).

Two different types of response were observed in the dynamic tests (Cheng et al. 2008a). Each type of unstable response differed in terms of amplitude of vibrations, dominant direction of motion, and Reynolds number range. However interestingly, the cable-wind relative angle ϕ in these two cases was both 60°.

Table 3-1 Testing conditions of wind tunnel experiments by Cheng et al. (2008a)

Test	Parameter measured	Model diameter (mm)	Model aspect ratio	ϕ range (°)	Wind speed (m/s)	Re range ($\times 10^5$)
Dynamic	displacement	160	≈40	35-60	10-36	1~3.4
Static	Pressure	88.9	≈22-27	54.7-107	10-95	0.8~6

The divergent type of motion with increasing amplitude (unless suppressed manually) was observed in an experimental setup corresponding to a full-scale cable inclined and yawed both with 45° with respect to the wind ($\alpha=\beta=45°$, thus $\phi=60°$). The major motion direction of this response was along the in-plane direction. Refer to Figure 3-1(b), it occurred at an angle $\gamma=54.7°$ with respect to the normal velocity component U_N. The contribution of out-of-plane motion is considerable, which made the motion trajectory of the total model response an elliptical path (Cheng et al., 2008a). Such a divergent type of response on an inclined and yawed cable was also observed in the wind tunnel studies by Miyata et al. (1994), Saito et al. (1994), and Honda et al. (1995) when investigating the rain-wind induced cable vibration. Since this divergent type response occurred without the presence of precipitation and had similar characteristics of galloping, it was thus called "dry inclined cable galloping" in the subsequent studies. When it occurred, the cable model orientation in the tests by Miyata et al. (1994) was identical to that by Cheng et al. (2008a), while those in the tests by Saito et al. (1994) and Honda et al. (1995) corresponded to a non-yawed full-scale cable inclined at 45° to wind. This would result in a relative cable-wind angle ϕ of 45°. The circular cylinder models used in all these studies had diameters of typical bridge stay cables but differed in terms of Reynolds number range, length, and unit mass. As for Reynolds number, the divergent motion was detected in the subcritical (Saito et al, 1994; Honda et al, 1995), transition (Miyata et al, 1994), and critical Reynolds number range (Cheng et al, 2008a). This suggests that the divergent type response or the so-called dry-inclined cable galloping is very sensitive to a broad range of onset conditions and hence it is likely to be triggered to occur over a broad Reynolds

number range. Although there is no field report of this phenomenon yet, the possibility of such divergent response should not be totally disregarded.

The second type of response, which had limited amplitude, was observed in a number of different setups. The most violent one occurred at a setup equivalent to a non-yawed full-scale cable inclined at 60° with respect to the oncoming wind (α=60°, β=0°). This response only occurred in the out-of-plane direction, which, in Figure 3-1(b), coincided with the direction of lift force or the across-wind direction in this specific case (γ=90°). It was found to be relatively easily suppressed by increasing structural damping (Cheng et al, 2003). This type of limited-amplitude response was more similar to that observed by Matsumoto (1998) and Matsumoto et al. (1999 & 2007a). The characteristics and critical onset conditions of the two types of responses identified in the dynamic tests are summarized in Table 3-2.

Static model tests were then designed to investigate the possible mechanisms associated with the two different types of response observed in the dynamic tests. Unsteady surface pressure measurements were carried out at five axial locations along the span of a rigid circular cylinder model. Figure 3-2 schematically illustrates the location of pressure tap rings along the cylinder span and array of pressure taps on a typical ring. As shown in the figure, five pressure tap rings were arranged along the cylinder model with 32 pressure taps installed on each ring in the circumferential direction θ. Previous analyses (Raeesi et al., 2008), however, showed that the data sampled at z/D=-10.5 (Ring 1) could be slightly distorted due to its proximity to the end plate. Therefore, data measured at the remaining four spanwise locations will be used for further analysis in this paper. Tests were conducted under three different cylinder

inclination angles of 54.7°, 60° and 90°, with a yaw angle range of 0°-120° for the first two inclination angles. The 90° inclination angle case corresponded to the classical problem of cross-flow past a circular cylinder.

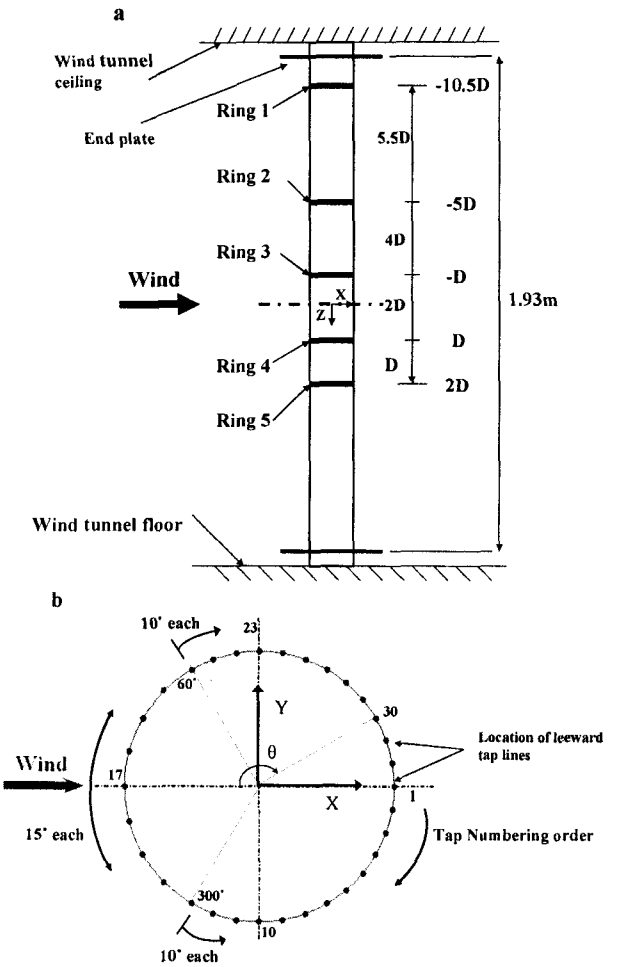

Figure 3-2- Experimental setup of static model test; a) Arrangement of pressure tap ring along the cylinder span (when α=90°) b) Array of pressure taps on a typical ring

It is interesting to note that though in both cases, the relative cable-wind angle was 60°, the observed response characteristics and onset conditions were different. This needs to be further studied from a more fundamental fluid dynamics point of view. The focus of the current study is then to utilize the unsteady surface pressure data from the

static tests to explore the difference in the possible mechanisms and onset conditions of the two types of unstable responses observed in the dynamic tests.

Table 3-2 Response characteristics of the two observed critical cases

Setup	Response type	Full-Scale cable angles(°)		Cable-wind relative angle (°)	Major motion direction (°)	Unstable Range	
		α	β	ϕ	γ	Re ($\times 10^5$)	U_r
2C	Divergent	45	45	60	54.7	3.16~3.37	79~84
2A	Limited amplitude	60	0	60	90	1.86~1.96	106~114

3.3 Discussion of observed phenomena

To investigate the flow structure around the cylinder model when the unstable responses occurred, and to unveil the possible mechanisms associated with them, in this section, wavelet analysis is first applied to the displacement data recorded in the dynamic tests to verify the onset conditions and dominant motion direction for the unstable response observed in Setups 2C and 2A (Table 3-2). Then, the applicability of a general expression for estimating aerodynamic damping ratio proposed by McDonald and Larose (2006) in explaining the unstable responses will be investigated using the surface pressure data sampled in the static tests. The axial correlation and power spectra of lift and drag forces on the cylinder are calculated and presented in the following sub-sections.

3.3.1 Wavelet analysis of cable motion

The wavelet coefficients of cylinder model displacement in the in-plane direction in Setup 2C are shown in Figure 3-3. The cylinder-wind relative angle ϕ is 60°, and the Reynolds number varies from upper limit of subcritical regime into critical flow state ($2.53\times10^5<Re<3.37^5$). It is evident from Figure 3-3(a) and (b) that within the subcritical range ($Re<3.16\times10^5$), response in the in-plane direction is weak. It is enhanced when Re reaches 3.16×10^5 (Figure 3-3 (c)). Once it is fully in the critical Re regime, at $Re=3.37\times10^5$, organized harmonic motion with increasing strength can be observed in Figure 3-3(d) which suggests the onset and occurrence of divergent type response. The response amplitude in Figure 3-3(d) shows continuous growth until the model vibration had to be manually suppressed due to clearance restriction of the wind tunnel. In the frequency domain, at $Re=3.37\times10^5$, the frequency of vibration was detected to be 1.465Hz, which is very close to 1.415Hz, the natural frequency of the cylinder model in-plane vibration. The wavelet coefficients of the out-of-plane response of the cylinder model are depicted in Figure 3-4 for the two critical Reynolds numbers of 3.16×10^5 and 3.37×10^5. By comparing to Figure 3-3, it shows that the divergent type motion initiated along the in-plane direction at $Re=3.16\times10^5$. Subsequently, the out-of-plane motion was triggered at a higher Reynolds number of 3.37×10^5 and built up quickly. Though the major direction of motion was within the cable plane, there was a considerable motion component perpendicular to the cable plane. Therefore, once the divergent motion initiated, the cable model vibrated following an elliptical trajectory with increasing amplitude.

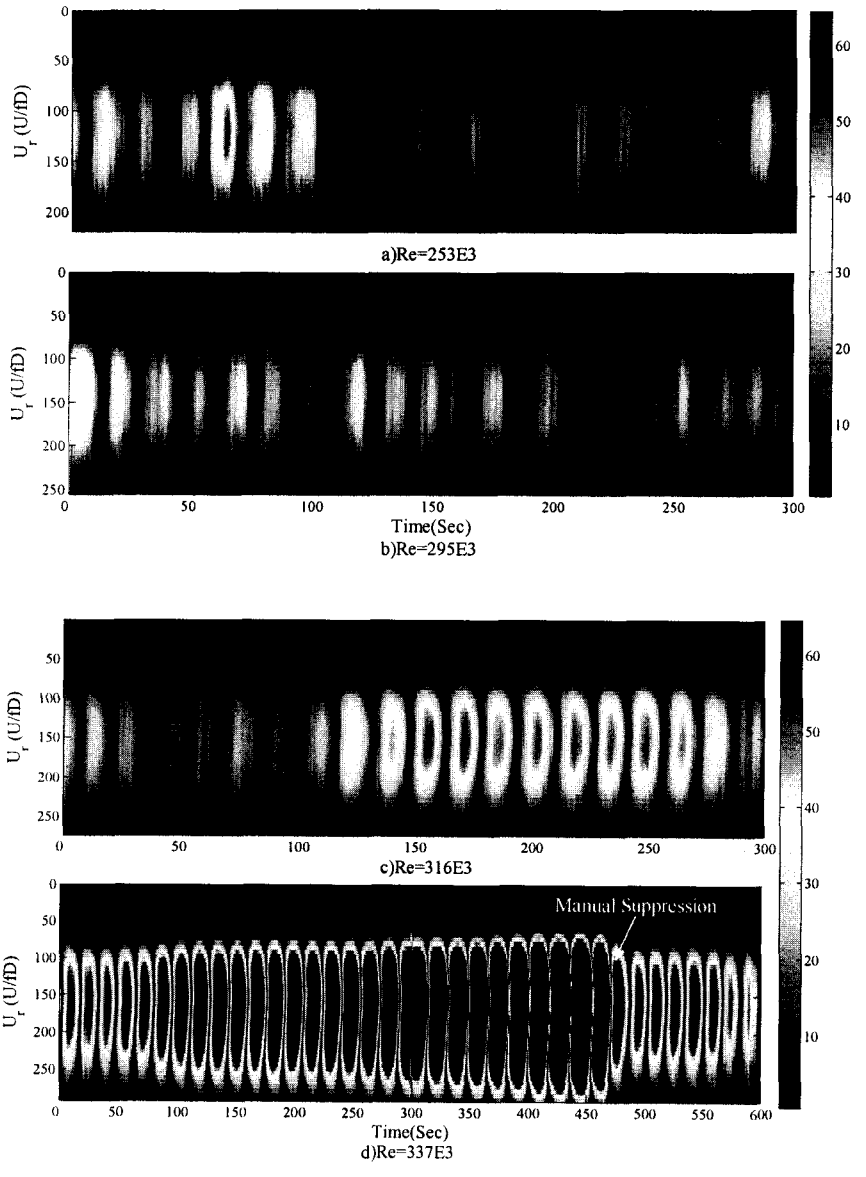

Figure 3-3- Wavelet of in-plane displacement component under Setup 2C condition (ϕ=60°, γ=54.7°)

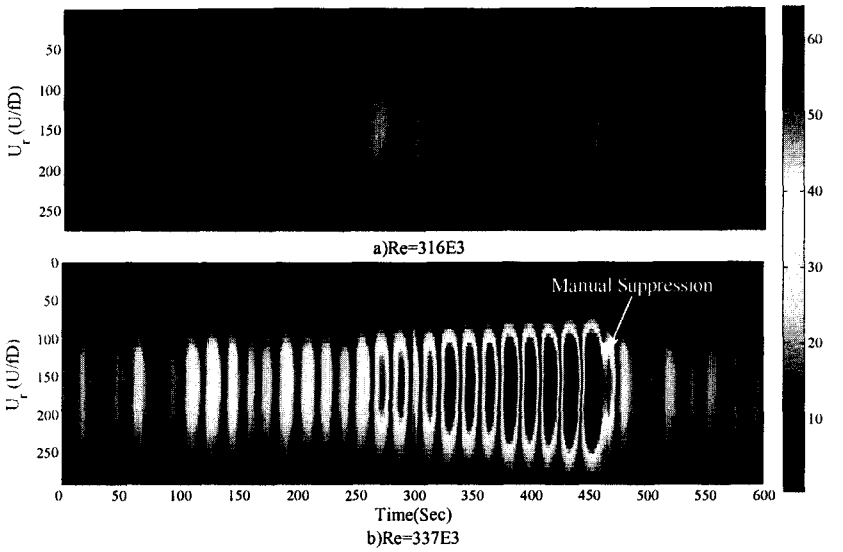

Figure 3-4- Wavelet of out-of-plane displacement component under Setup 2C condition (ϕ=60°, γ=54.7°)

The wavelet coefficients of out-of-plane and in-plane model displacements in Setup 2A are shown respectively in Figures 3-5 and 3-6 where limited-amplitude unstable response was observed. As can be seen from the figures, instability occurs along the out-of-plane direction and is very distinct at Reynolds numbers of 1.90×10^5 and 2.00×10^5 (Figure 3-5(c) and Figure 3-5(d)). The response is a very organized harmonic motion which is suppressed automatically when reaching Re=2.11×10^5. The in-plane component of motion within this critical range, however, shows no sensible excitation as depicted in Figure 3-6. It should be noted that the magnitude of the wavelet coefficients in Figure 3-3 to Figure 3-6 directly reflect how well the motion is organized. These coefficients are not the index of displacements.

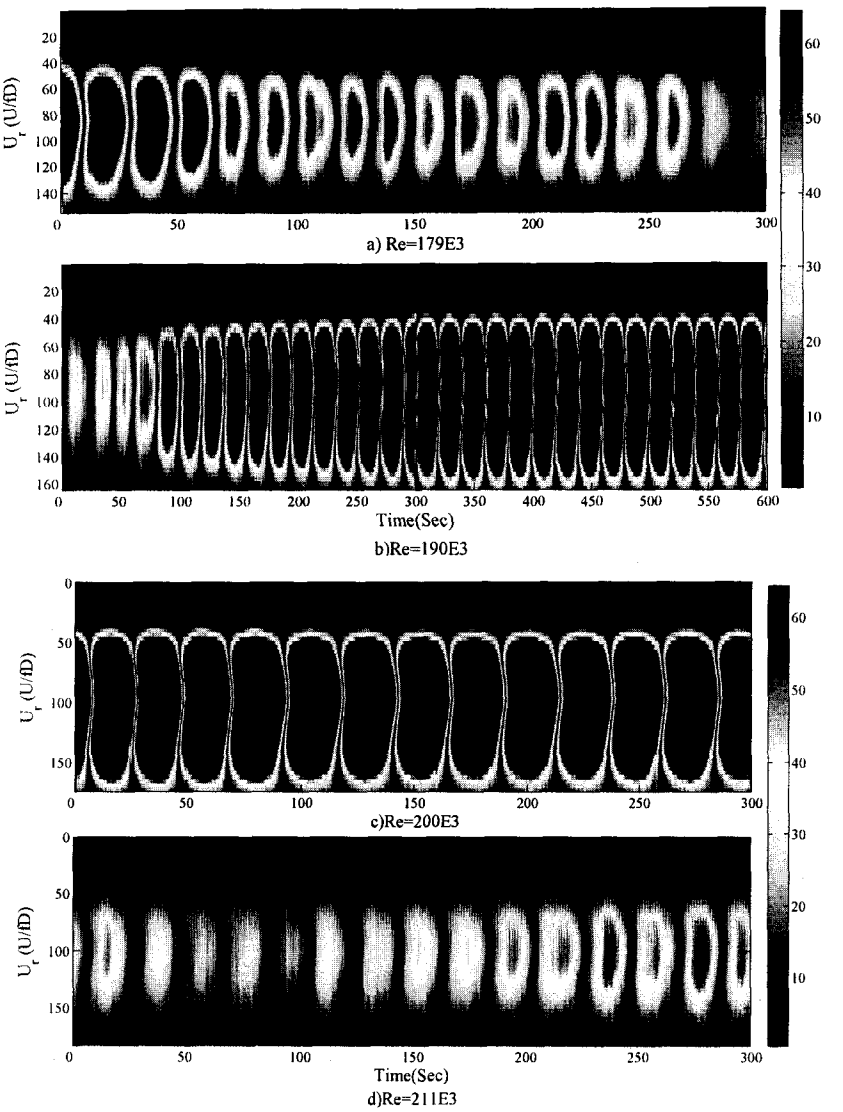

Figure 3-5- Wavelet of out-of-plane displacement component under Setup 2A condition (ϕ=60°, γ=90°)

On real bridges, Setup 2C is equivalent to a full-scale cable inclined and yawed both at 45° with respect to the mean wind direction. The observed unstable response contains both in-plane and out-of-plane components, with the former being predominant. This suggests that the direction of cable motion does not coincide with the wind direction, i.e. both lift and drag contribute to the excitation of the cable. On

the other hand, Setup 2A is designed to reproduce the real scenario of wind blowing along the stay cable, and the cable inclined at 60° towards the oncoming wind with no yaw. The observed motion direction is out-of-plane, i.e. across-wind. Therefore, the source of excitation comes from lift force.

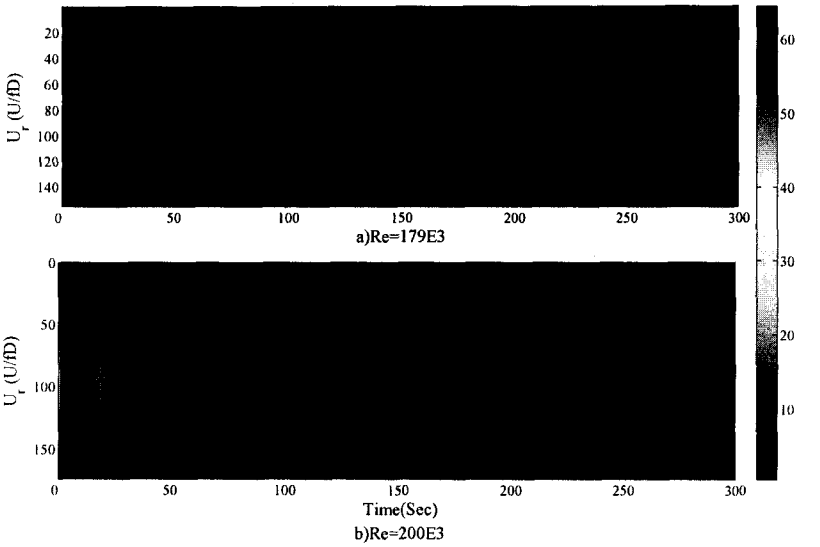

Figure 3-6- Wavelet of in-plane displacement component under Setup 2A condition (ϕ=60°, γ=90°)

3.3.2 Aerodynamic damping

3.3.2.1 Application of a general expression of aerodynamic damping ratio

When a structure undergoes wind-induced vibration, the total damping contained in the oscillating system includes two parts, i.e. the inherent structural damping and the aerodynamic damping contributed by wind. In the classical galloping theory, which was proposed by Den Hartog (1956), the structure is modeled as a single-degree-of-freedom system. The aerodynamic damping is then proportional to $(\partial C_L / \partial \alpha_a + C_D)$, where C_L and C_D are respectively the lift and drag force coefficients, and α_a is the wind angle of

attack. For a structure that has non-circular cross-section, negative slope of lift against wind angle of attack could exist at certain orientations and Reynolds numbers, resulting in negative aerodynamic damping. Once it overcomes the positive structural damping, the overall effective damping of the vibrating structure will become negative, and divergent motion will be initiated. This criterion well explained the necessary onset condition of iced-cable galloping. Its applicability in explaining the divergent motion observed in Setup 2C was investigated and confirmed by Cheng et al (2008b). However, it should be noted that the classical Den Hartog criterion is derived based on a single-degree-of-freedom model, whereas the unstable motion observed in Setup 2C follows an elliptical trajectory, i.e. contains both in-plane and out-of-plane components. Further, in the case of an inclined and/or yawed circular cylinder, the aerodynamic forces and surrounding flow patterns are extremely sensitive to model orientation and Reynolds number, which are not considered in the formulation of the classical Den Hartog criterion.

Some recent efforts made to derive a general expression for the quasi-steady aerodynamic damping of an arbitrary cross-section cylinder inclined and/or yawed to wind includes McDonald (2002) and McDonald and Larose (2006). These works include contributions of lift, drag, Reynolds number, and wind-cylinder relative angle in the formulation. It is applicable to small amplitude vibrations of cylinder in any direction which is induced by flow. In the current study, to estimate the aerodynamic

damping of the circular cylinder under the physical conditions simulated in the static tests, this general expression can be simplified as[1]:

$$\zeta_a = \frac{\mu \mathrm{Re}}{4m\omega_n}\cos\gamma\left\{\cos\gamma\left[C_D\left(2\sin\phi+\frac{\tan^2\gamma}{\sin\phi}\right)+\frac{\partial C_D}{\partial \mathrm{Re}}\mathrm{Re}\sin\phi+\frac{\partial C_D}{\partial\phi}\cos\phi\right]\right. \\ \left.\pm\sin\gamma\left[C_L\left(2\sin\phi-\frac{1}{\sin\phi}\right)+\frac{\partial C_L}{\partial \mathrm{Re}}\mathrm{Re}\sin\phi+\frac{\partial C_L}{\partial\phi}\cos\phi\right]\right\} \tag{3-2}$$

where ζ_a is the aerodynamic damping ratio, μ is the dynamic viscosity, ω_n is the undamped natural circular frequency of the model, m is the mass per unit length of cylinder, γ is the angle between the major direction of motion and normal velocity component, and ϕ is the wind-cylinder relative angle (Figure 3-1). The terms included inside the first and the second square brackets are referred as drag and lift term, respectively. The dual sign of the lift force term in the equation is associated with the asymmetric flow regime when flow enters the critical range. Within the critical Reynolds number range, a single separation bubble forms on one side of the cylinder surface. Depending on at which side it occurs, the lift force could be either positive or negative (see for example Zdravkovich (1997) or Schewe (1983)).

[1] Please note that Mcdonald and Larose (2006) used different nomenclatures in their study.

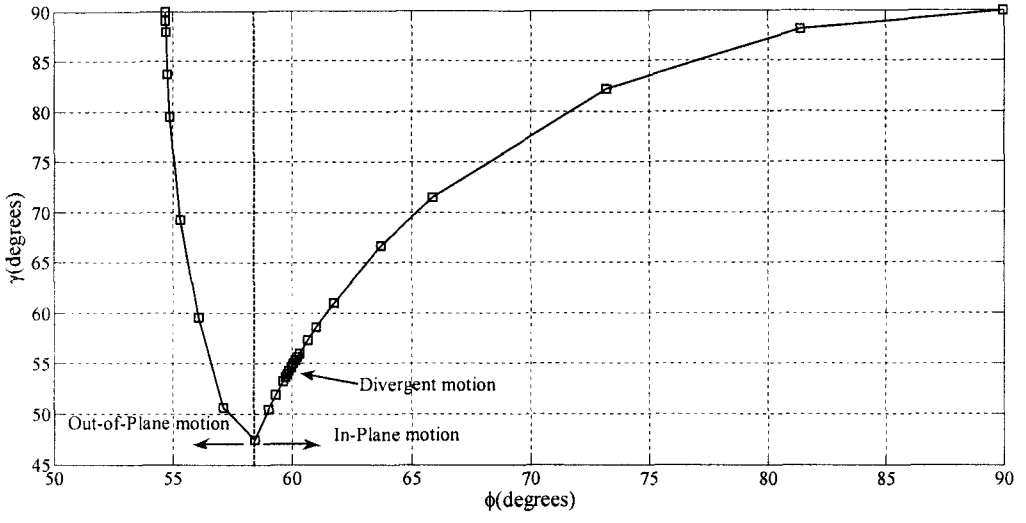

Figure 3-7- Major direction of motion predicted for the range of ϕ in the static tests when model is inclined by 54.7° against wind, including Setup 2C condition (ϕ=60°, γ=54.7°)

When a circular cylinder is both inclined and yawed with respect to wind, the aerodynamic damping can be estimated by Equation (3-2). As of the interest of current study, the aerodynamic damping is investigated for the range of Reynolds number and relative angle used in the static tests, i.e. $Re=1.15\times10^5$~3.54×10^5 and ϕ=54.7°~90°. This angle range corresponded to α=54.7° and β=0°~90°, while the range of γ, which represents the predominant motion direction, varies between 47° and 90° as shown in Figure 3-7. The minimum of γ≈47° occurs at ϕ≈58°, where lift and drag contribute almost equally to excite the cable. For the divergent response observed in Setup 2C, the major direction of motion is γ≈54.7°. This γ value is close to 47°. Thus, it has two considerable components in the in-plane and out-of-plane directions. When γ deviates further from the minimum value of 47°, however, the role of lift force becomes more important in the excitation of the cable. For ϕ<58°, the major direction of response is out-of-plane, which is closer to the direction of lift force. Whereas for ϕ>58°, the major

direction of response is in-plane. For the extreme cases of ϕ=54.7°, the direction of response is purely out-of-plane. This is similar to the response characteristics of a non-yawed but inclined cylinder, as observed in Figure 3-5 for in Setup 2A (when ϕ=60°). Therefore, the response direction coincides to the direction of lift force. For ϕ=90°, however, the assumed response direction is in-plane, similar to a freely vibrating cylinder in cross-flow which is excited by the fluctuating lift force. In fact, the direction of response for both extreme cases, be it in-plane or out-of-plane, coincides with the direction lift force and thus γ equals to 90° for both cases as shown in Figure 3-7.

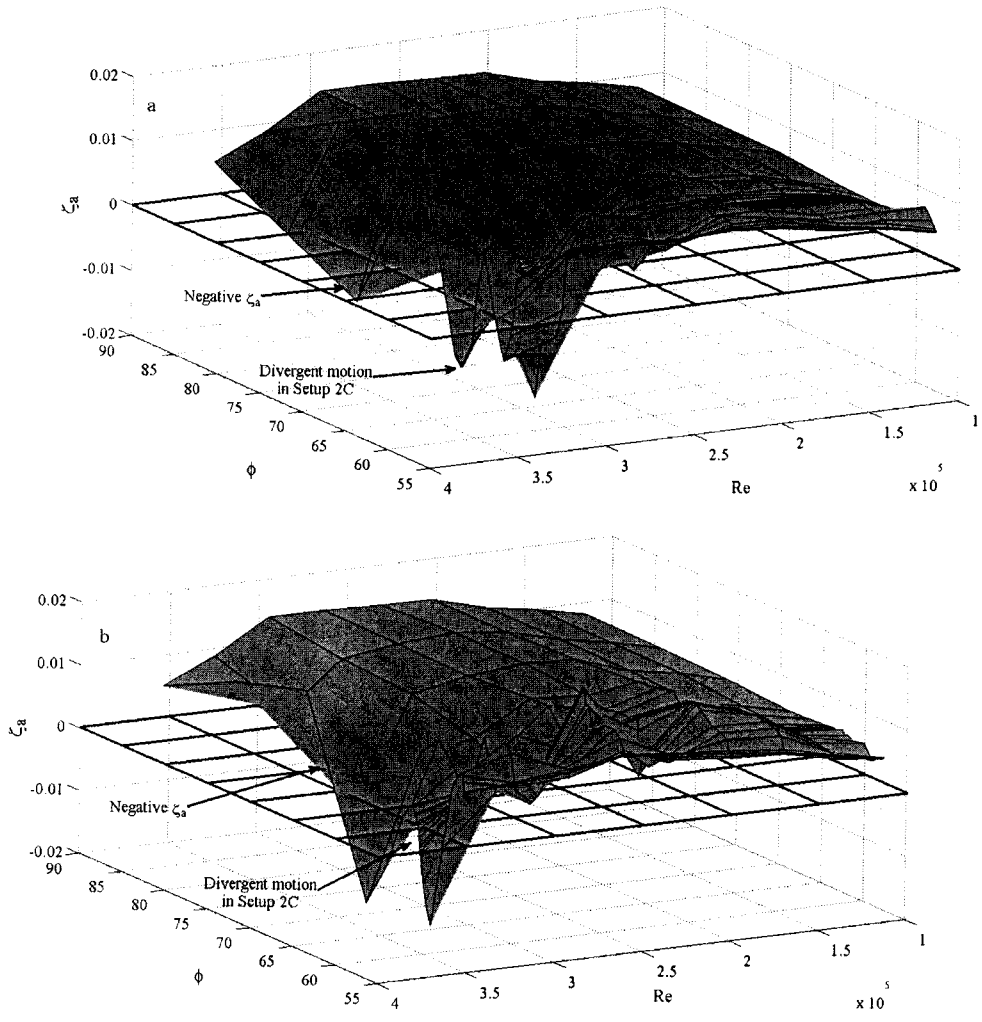

Figure 3-8- Aerodynamic damping ratios of the cylinder in the static tests when model is inclined by 54.7° against wind, including Setup 2C condition (ϕ=60°, γ=54.7°); a) For +sin γ b) For –sin γ

To calculate the aerodynamic damping of the cylinder under Setup 2C condition (ϕ=60°, γ=54.7°), lift and drag forces obtained in the equivalent static tests are utilized in Equation (3-2). The results are presented in Figure 3-8. Both positive and negative signs of the lift force terms were considered and illustrated respectively in Figure 3-8 (a) and Figure 3-8 (b). As can be seen from these two figures, in the subcritical Reynolds number range, aerodynamic damping ratios are positive. In fact, no negative

value of ζ_a is observed for $Re<3\times10^5$. Large negative aerodynamic damping ratios can be seen in the figure for $\phi\approx60°$ (i.e. $\alpha=54.7°$, $\beta\approx30°$) and $Re>3\times10^5$ which corresponded to the critical onset condition of the divergent response in Setup 2C.

Another range of negative ζ_a values in Figure 3-8 (a) and Figure 3-8 (b) can be observed at $\phi\approx63°$-$81°$ and $Re>3\times10^5$. Within this range, the time-averaged lift forces that already exist due to asymmetry in the cylinder orientation become relatively small and the formation or burst of a single separation-bubble on one side of the cylinder could alter the lift force dramatically. Therefore, it seems that within this range, the term $\partial C_L/\partial Re$ in Equation (3-2) has major contribution to negative ζ_a values. However, unfortunately there are no dynamic test data to verify the occurrence of divergent motion for this range.

Substituting $\gamma=90°$ to simulate Setup 2A conditions in the dynamic tests, Equation (3-2) reduces to:

$$\zeta_a = \frac{\mu \mathrm{Re}}{4m\omega_n}\left[\frac{1}{\sin\phi}C_D\right] \tag{3-3}$$

This equation is valid when a non-yawed circular cylinder is inclined at an angle ϕ with respect to wind and vibrates in the across-wind direction. The outcome of this equation is always positive. This indicates that the observed limited-amplitude instability in Setup 2A (Figure 3-5 and Figure 3-6) would never become divergent. In other words, this Equation (3-3) suggests that on a real bridge site, when wind blows along bridge axis (i.e. $\beta=0°$), cable vibration would not become divergent due to the existence of positive aerodynamic damping. Accordingly, the limited-amplitude

instability occurred in Setup 2A does not have the same mechanism as that in Setup 2C, but rather, is associated with the existence of shear-layer instability that causes the regular Karman vortex shedding and oscillatory lift force on a circular cylinder (see for example Snarski (2004)).

It appears from the results that the negative aerodynamic damping ratios predicted by Equation (3-2) are able to successfully predict the onset of divergent type of response as in Setup 2C (ϕ=60°, γ=54.7°). At the same wind-cylinder relative angle as in Setup 2C, however, no divergent response was observed in Setup 2A (ϕ=60°, γ=90°). This is because Equation (3-2) is greatly affected by the direction of motion γ, which is along the across-wind direction (γ=90°) in Setup 2A and thus the aerodynamic damping ratio is given by Equation (3-3) which would never result in a negative value.

3.3.2.2 Contributions of different terms to negative aerodynamic damping

In order to investigate the flow structure around the cylinder within the range of observed negative aerodynamic damping ratio, circumferential surface pressure distribution around the cylinder at different axial locations of z/D=-5, -1, 1, 2 (Rings 2-5 as shown in Figure 3-2) were first averaged and then plotted against Re for different yaw angles in Figure 3-9. It could be seen from Figure 3-9(a) that at Re=3.25×10^5, when β=0° (ϕ=54.7°), pressure distribution is slightly asymmetric which seems to be more affected by the orientation of cylinder than critical regime. When β is increased to 30° (ϕ=60°), pressure distribution becomes more symmetric whereas by reaching β=40° (ϕ=63.7°), the asymmetric pressure distribution reappears. The asymmetry of circumferential surface pressure distribution is strengthened with further increase of

yaw angle to β=60° (ϕ=75.5°) and β=90° (ϕ=90°). At a higher Reynolds number of 3.54×10^5, as shown in Figure 3-9(b), the sharp drop of C_P at one side of the cylinder at β=0° (ϕ=0°) states the formation of a single separation bubble. This regime is accompanied by clearly asymmetric circumferential pressure distribution. By reaching β=20° (ϕ=57.1°), however, the symmetric pattern reappears with another sharp drop of C_P value on the other side of the cylinder. This is more obvious for β>40° which states that by decreasing ϕ (or increasing the yaw angle β), transition from a single separation bubble regime to double separation bubble regime could occur while the Reynolds number is kept constant.

The physical condition under which asymmetric surface pressure distribution occurs is consistent with those where negative aerodynamic damping was identified in Figure 3-8. Further, it indicates that if keep Reynolds number as a constant, even by introducing a small change of cylinder orientation would cause a dramatic change in the flow structure. This could lead to a significant negative value of $\partial C_L/\partial\phi$ term. Accordingly, it might be concluded that the range of $\phi\approx$55°~64° (β=0°~40°, while α=54.7°) is a breakdown range within and/or beyond which considerable changes may occur in the flow structure which could lead to negative $\partial C_L/\partial\phi$.

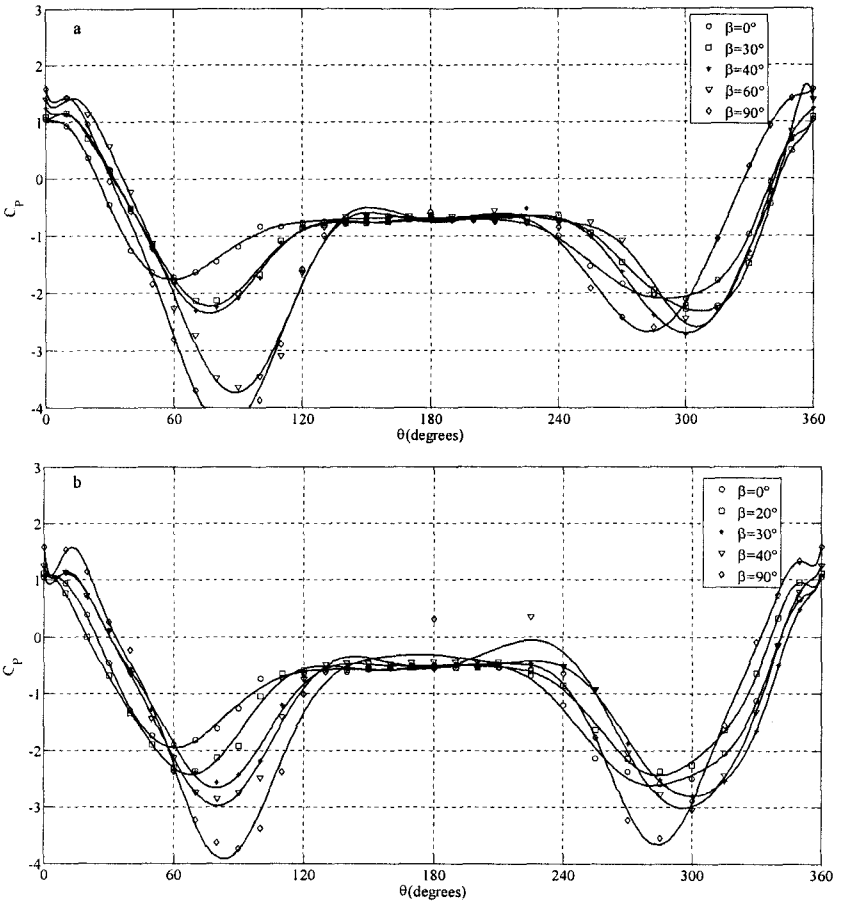

Figure 3-9- Circumferential pressure distribution in the static tests when model is inclined by 54.7° against wind, including Setup 2C condition (ϕ=60°, γ=54.7°); a) Re=3.25×10^5 b) Re=3.54×10^5

It is evident from Figure 3-8 that in Setup 2C, when Re>3×10^5 and ϕ is around 60°, both negative and positive aerodynamic damping ratios could be achieved. This suggests that the flow is extremely sensitive within this relatively narrow range of wind-cylinder relative angle where formation or burst of separation bubbles occurs. In Equation (3-2), the weight functions of the lift and drag terms in the expression of aerodynamic damping are $\pm\sin(\gamma)\cos(\gamma)$ and $\cos^2(\gamma)$, respectively. To evaluate the contributions of these two terms to the aerodynamic damping ratio when the cylinder

vibrates along any arbitrary direction, the lift and drag terms, and the variation of the corresponding weight functions are plotted in Figure 3-10 for γ=0°-90°, i.e. for a full sweep of possible predominant motion direction from in-plane to out-of-plane. As can be seen from Figure 3-10(a), the lift term is mostly negative for the range of Reynolds number studied (i.e. Re=0.86×10^5-3.54×10^5). In particular, a significant increase-decrease manner is detected within the range ϕ=63°-81° when Re>3×10^5. This could be due to the formation of the single separation bubble on one side of the cylinder surface, giving rise to a relatively large positive C_L (Re=3.25×10^5). As the Reynolds number is further increased (Re=3.55×10^5), the second separation bubble on the other side of circular cylinder surface forms and thus symmetric distribution of surface pressure reappears. This causes a significant drop in the lift force value accompanied by a negative $\partial C_L/\partial Re$ term. However, the drag term, as shown in Figure 3-10(b), are positive within the subcritical Re range. Once the flow enters the critical state, $\partial C_D/\partial Re$ term becomes negative for the entire range of ϕ and, the contribution of this term to the negative aerodynamic damping becomes more significant (Figure 3-10(b)). The direction of motion is considered in the total aerodynamic damping ratio as the weight functions of lift and drag terms. They are presented in Figure 3-10(c). At γ=0° (i.e. in-plane motion), the weight function of drag term has its maximum value while that for lift term is zero. This suggests that when the vibration is within the cable plane, negative aerodynamic damping could occur in the critical Re regime. However, to the knowledge of the authors, pure in-plane vibration (γ=0°) has never been observed in field and experimental studies. The maximum (or minimum) value of the weight function of the lift term occurs at γ=45° which equals to 0.5 (or -0.5). It is noted that

when γ=45°, the weight function of the drag term also equals to 0.5. Therefore, if lift and drag terms are negative, their weighted values in Equation (3-2) could still be kept as negative and results in negative aerodynamic damping ratio. In other words, it suggests that when $\gamma \approx 45°$ vibration contains almost the same components along the in-plane and out-of-plane directions, the total aerodynamic damping ration is likely to become negative in the critical Re regime. In the current study, the γ values closest to 45° was 47.5°, which occurred at ϕ=58.4° (Figure 3-7). This is in fact very close to the setup condition of 2C, where ϕ=60° and γ=54.7°. However, for across-wind vibration, as in the case of Setup 2A, the direction of motion is along γ=90°. Therefore, weight functions of both lift and drag terms would become zero. In such case, the resulting total aerodynamic damping ratio given by Equation (3-3) is always positive. McDonald and Larose (2006) also investigated contributions of different terms in Equation (3-2) and pointed out that at $\phi \approx 60°$, the $\partial C_L/\partial \phi$ and $\partial C_D/\partial Re$ terms have the most significant contribution to negative ζ_a values due to the emergence of critical Re regime as shown in Figure 3-9. Within the range of ϕ=65°~81°, however, $\partial C_L/\partial Re$ and $\partial C_D/\partial Re$ contribute more considerably.

It should be noted that, the lift and drag values used in the above analysis are the averaged values of sectional forces sampled at four different longitudinal locations of the cylinder model. They may not express the effects by the total instantaneous lift and drag forces. As it was observed in Figure 3-3 and Figure 3-4, the divergent type response was triggered after about 100s in the dynamic tests. This suggests that instantaneous values of aerodynamic forces and their correlation along the cylinder length are also important fa for the triggering of unstable motion. The spatial

correlation of instantaneous aerodynamic forces will be investigated in the following section.

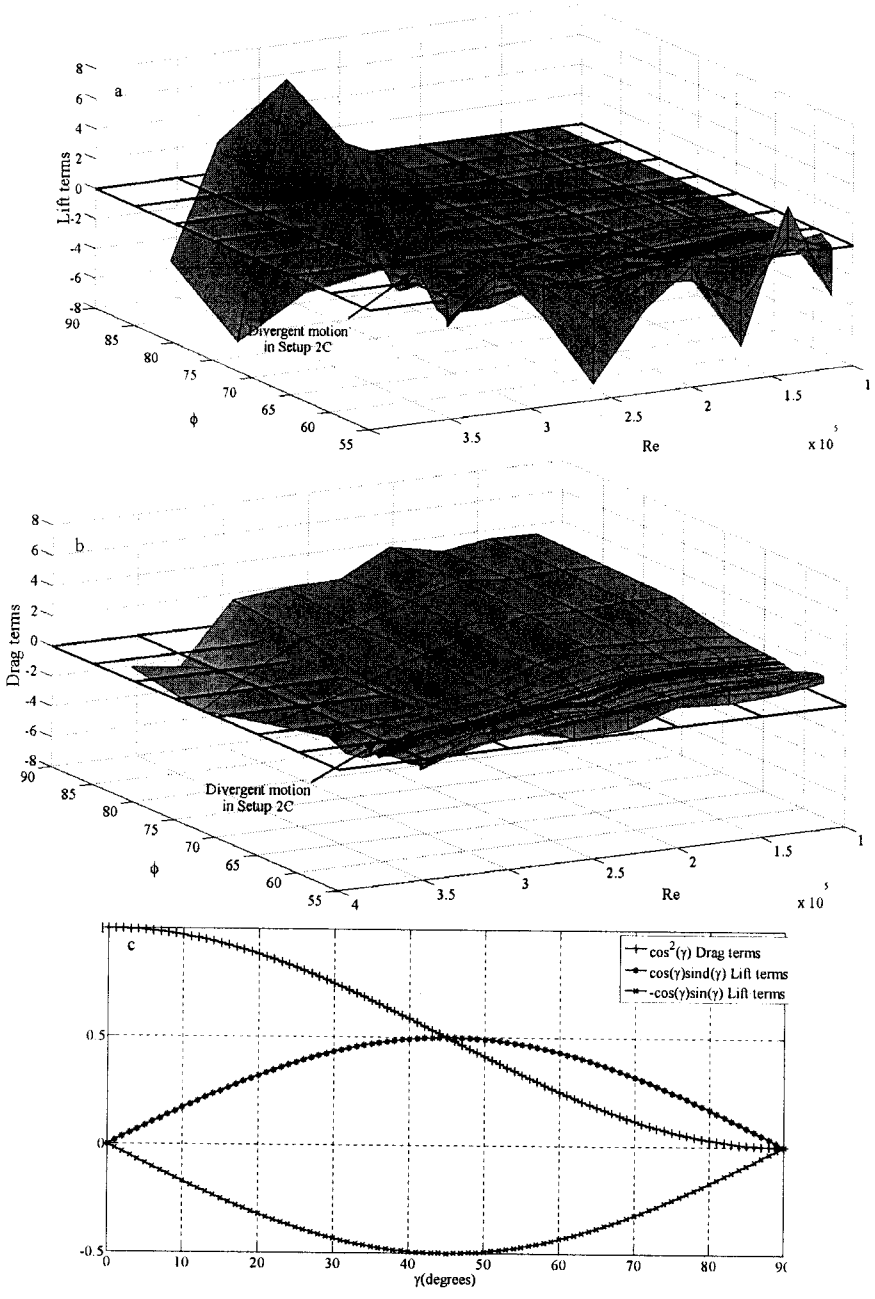

Figure 3-10- Contribution of lift and drag terms in total aerodynamic damping; a) Lift term=$\left[C_L\left(2\sin\phi-\frac{1}{\sin\phi}\right)+\frac{\partial C_L}{\partial \mathrm{Re}}\mathrm{Re}\sin\phi+\frac{\partial C_L}{\partial\phi}\cos\phi\right]$ b) Drag term=$\left[C_D\left(2\sin\phi+\frac{\tan^2\gamma}{\sin\phi}\right)+\frac{\partial C_D}{\partial \mathrm{Re}}\mathrm{Re}\sin\phi+\frac{\partial C_D}{\partial\phi}\cos\phi\right]$ c) Weight functions

3.3.3 Spatial correlation

Spatial correlation of sectional aerodynamic forces is greatly affected by spanwise non-uniformities of flow separation process (Zdravkovich, 1997). Within the lower subcritical Reynolds number range (say up to a couple of thousands), where the separation line is relatively straight or somewhat wavy but with a very long wavelength, nearly perfect spatial correlation was observed (see for example Roshko, 1954; Williamson, 1989). This is because the transition to the turbulence point is not close enough to the cylinder surface to alter the separation process. In the higher subcritical Reynolds number range (Re up to 2×10^5), the transition to turbulence occurs in the near-wake eddies. The irregular turbulent eddies induce larger scale non-uniformity along the separation line, resulting in wavy shape separation line and eddy filaments. These are responsible for the phase lag between aerodynamic properties along the cylinder axis. In such situations, the straight separation line is disturbed and thus the axial correlation of aerodynamic properties is weakened (Shimuzo and Kawamura, 1972). Compared to the monotonically decreasing pattern in the subcritical Re range, when entering the critical Re range, the spatial correlation of aerodynamic properties becomes very sensitive to the axial distance between two measurement locations. It has been noted in a few studies that this phenomenon is attributed to the presence of cell-like structures along the span of cylinder in the upper subcritical and critical Re range (Humphreys, 1960; Higuchi et al, 1989). In a recent study by Raeesi et al. (2008) it was found that the spatial correlations are considerably enhanced for certain spanwise distances which are multiples of cell size (Raeesi et al, 2008).

A parameter which signifies the spanwise uniformity of flow past a cylinder is the correlation length, L_C. It represents the axial range over which the variation of aerodynamic properties at one station are correlated with those at another. It can be defined as (Zdravkovich, 1997):

$$L_C = \int_0^\infty R_{12}(z)dz \tag{3-4}$$

where R_{12} is the spatial correlation between the two measurement points 1 and 2. In fact, this parameter shows the deviation of flow field from an assumed two-dimensional one of which the straight separation line oscillates on the surface of the cylinder and all aerodynamic forces correlate perfectly.

Using the surface pressure data sampled at z/D=-2, -1, 1, and 2 (Rings 2-5 as in Figure 3-2(a)), yields six combinations of spatial distances between the two measurement locations. The definition of correlation length L_C given by Equation (3-4) is modified due to the finite number of measurement points as:

$$L_C = \sum_{k=1}^{6} R_{ij}(k)Z_{ij}(k) \tag{3-5}$$

where

$$Z_{ij}/D = [1 \quad 2 \quad 3 \quad 4 \quad 6 \quad 7] \tag{3-6}.$$

If the aerodynamic properties along the cylinder span are perfectly correlated, i.e. $R_{ij}=1$ for any two arbitrary locations i and j, Equation (3-5) would reduce to:

$$Z_{\max} = \sum_{k=1}^{P} Z_{ij}(k) \tag{3-7}$$

Thus, the maximum correlation length would be 23D. In the following analysis, the computed correlation length will be normalized by this value.

The normalized correlation length of sectional lift and drag force coefficients versus the cylinder-wind relative angle ϕ in Setups 2C (ϕ=60°, γ=54.7°) and 2A (ϕ=60°, γ=90°) are respectively shown in Figure 3-11 and Figure 3-12. The correlation coefficients are first calculated using time-histories of sectional lift and drag force coefficients at z/D=-5, -1, 1, and 2 (Rings 2-5 as in Figure 3-2(a)). Then, they are summed along the span of the cylinder using Equation (3-5) and normalized by Z_{max}. The second horizontal axis in these two figures represents the strength of axial component of flow in terms of the ratio between the axial flow speed and the total oncoming flow speed. It is equal to $\cos\phi$. In Figure 3-11(a), the correlation length of lift force in static test including Setup 2C conditions is shown for three critical Reynolds numbers of Re=2.94×10^5~3.55×10^5. The correlation length shows a significant increase in the range of $\phi\approx$55°~64° and reaches peak at ϕ=60°, which was equivalent to the critical condition of Setup 2C (ϕ=60°, γ=54.7°). Interestingly, this range coincides with the breakdown range observed in Figure 3-9. This suggests that the dramatic changes in the symmetry of flow field surrounding the cylinder model are associated with spatially correlated flow patterns around the cylinder model. This phenomenon, however, was only observed at Re=3.55×10^5, the highest critical Reynolds number tested in Setup 2C condition. In addition, the correlation length L_C of sectional drag force is plotted for the same range of Re. The observed peak is evident at Re=3.55×10^5, though to a smaller degree as compared to the lift case.

Large negative and positive values of spatial correlation coefficients within the single separation bubble regime were observed in the previous study by Raeesi et al. (2008) for ϕ=90°. These positive and negative values would somewhat cancel out when using Equation (3-5) to compute the correlation length. However, when ϕ=60°, as illustrated in Figure 3-11, the enhanced correlation length at critical conditions is risen from the summation of positive correlation values. This could also be interpreted in terms of the deviation from an assumed quasi two-dimensional flow field, i.e. the higher L_C values indicate that the surrounding flow structure is closer to the ideal quasi two-dimensional flow assumption. In such situation, the maximum instantaneous lift and drag force would occur simultaneously at different longitudinal locations and lead to larger instantaneous aerodynamic forces.

The mathematical form of Equation (3-2) shows that negative ζ_a value of a constant cross-section cylinder in the uniform flow is solely a function of Re, γ, and ϕ. This is because Equation (3-2) is derived based on the assumption of quasi-steady aerodynamic forces which are independent of mode shape and modal frequency of the cylinder (McDonald and Larose, 2006). Also, noting the fact that the aerodynamic damping ratio in Equation (3-2) is inversely proportional to the natural frequency of the excited mode, a mode with lower frequency will yield a larger negative value of ζ_a, and thus the cylinder is more likely to be excited (McDonald and Larose, 2006). The model used in the dynamic tests was a rigid circular cylinder. It was elastically supported at each end by two sets of springs along the in-plane and out-of-plane directions. When divergent type response occurred, the first vibration mode of the cylinder model was excited. Considering these facts, it appears that in practice, a highly correlated flow field along

the cylinder, in collaboration with negative aerodynamic damping, might be a determining factor or even a necessary onset condition for exciting the divergent motion of a cable model in the first mode.

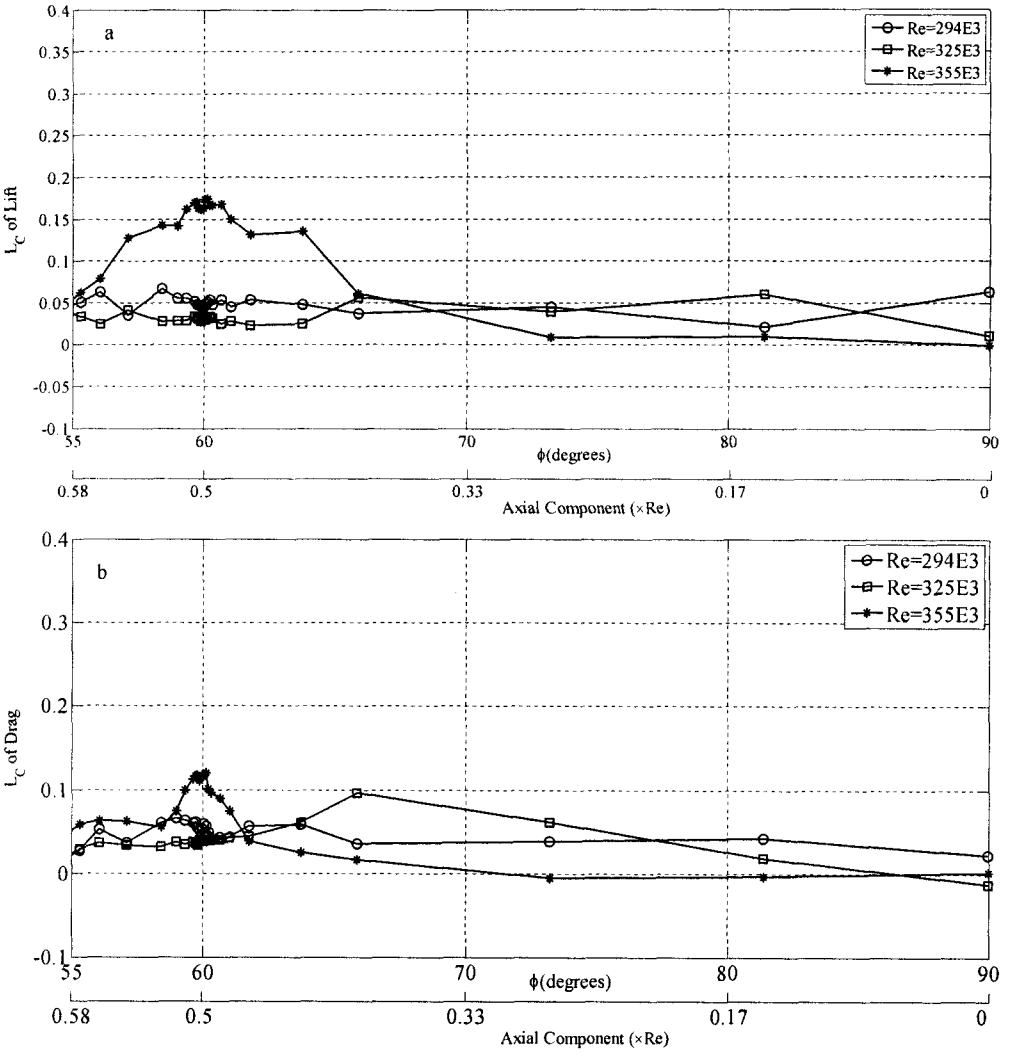

Figure 3-11- Correlation length of sectional aerodynamic forces acting on cylinder in the static tests when model is inclined by 54.7° against wind, including Setup 2C condition (ϕ=60°, γ=54.7°); a) Subcritical Reynolds number range b) Critical Reynolds number range

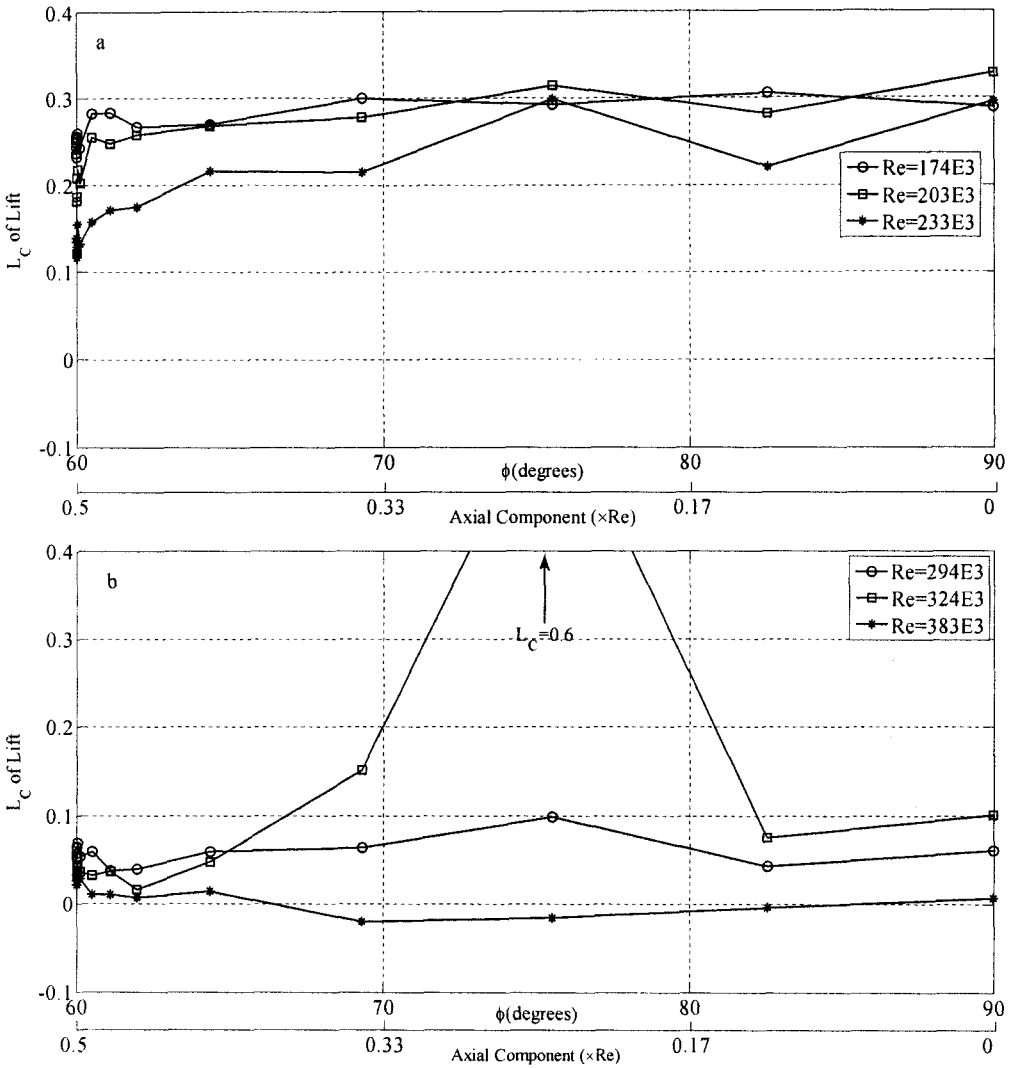

Figure 3-12- Correlation length of sectional lift forces acting on cylinder in the static tests when model is inclined by 60° against wind, including Setup 2A condition (ϕ=60°, γ=90°); a) Subcritical Reynolds number range b) Critical Reynolds number range

To investigate the observed limited-amplitude response in Setup 2A (ϕ=60°, γ=90°) in Figure 3-12, the correlation length of sectional lift forces are plotted against the cylinder-wind relative angle ϕ, for the Re range of 1.74×10^5~3.83×10^5. The first three Reynolds numbers in Figure 3-12(a) fall within the Re range of which the limited-amplitude response was observed in the dynamic tests. Within this range, L_C has a

slightly increasing trend against ϕ. For ϕ=60°~90°, L_C increases about 100% at Re=2.33×10^5 and about 50% for Re=1.74×10^5 and 2.03×10^5. At ϕ=90°, the correlation lengths for all three Reynolds numbers are more or less in the same range ($L_C\approx$0.29~0.33), while at $\phi\approx$60°, L_C differs almost about 100% for three different Reynolds numbers ($L_C\approx$0.12~0.25). This indicates that in the subcritical state, the introduction of axial flow reduces the spatial correlation and promotes the emergence of critical flow at a Reynolds number lower than that in the cross-flow case (ϕ=90°). The axial flow, which serves to destroy spatial correlation of flow, is weakened by the increasing ϕ. In the critical range, however, the axial flow does not alter the correlation length considerably (Figure 3-12(b)). Interestingly, a significant increase of correlation length is observed at ϕ=75° ($\alpha=\beta$=60°) when Re=3.22×10^5. This, and considerable increase in correlation length observed in Figure 3-11 at ϕ=60° are perhaps linked with a drastic modification of flow patterns in the critical flow regime when Re is kept constant but ϕ varies. Further experimental study is required to confirm and clarify this speculation.

3.3.4 Power spectra density of aerodynamic forces

The shear-layer instability is responsible for the fluctuating flow field and thus fluctuating lift and drag forces acting on cylinder which causes flow-induced vibrations. Fast Fourier Transform (FFT) is applied to the time-histories of lift and drag forces to obtain their power spectra. In Figure 3-13, the Power Spectra Density (PSD) surfaces of fluctuating lift force at z/D=1 (location of Ring 4, the ring closest to the mid-span) are shown. The frequency domain is normalized by U/D, where U is the free

stream wind tunnel flow speed and D is the cylinder diameter. The lift power spectra at four different Reynolds numbers are presented in Figure 3-13 from the lowest subcritical Re=0.86×10^5, to the highest studied critical Reynolds number Re=3.83×10^5.

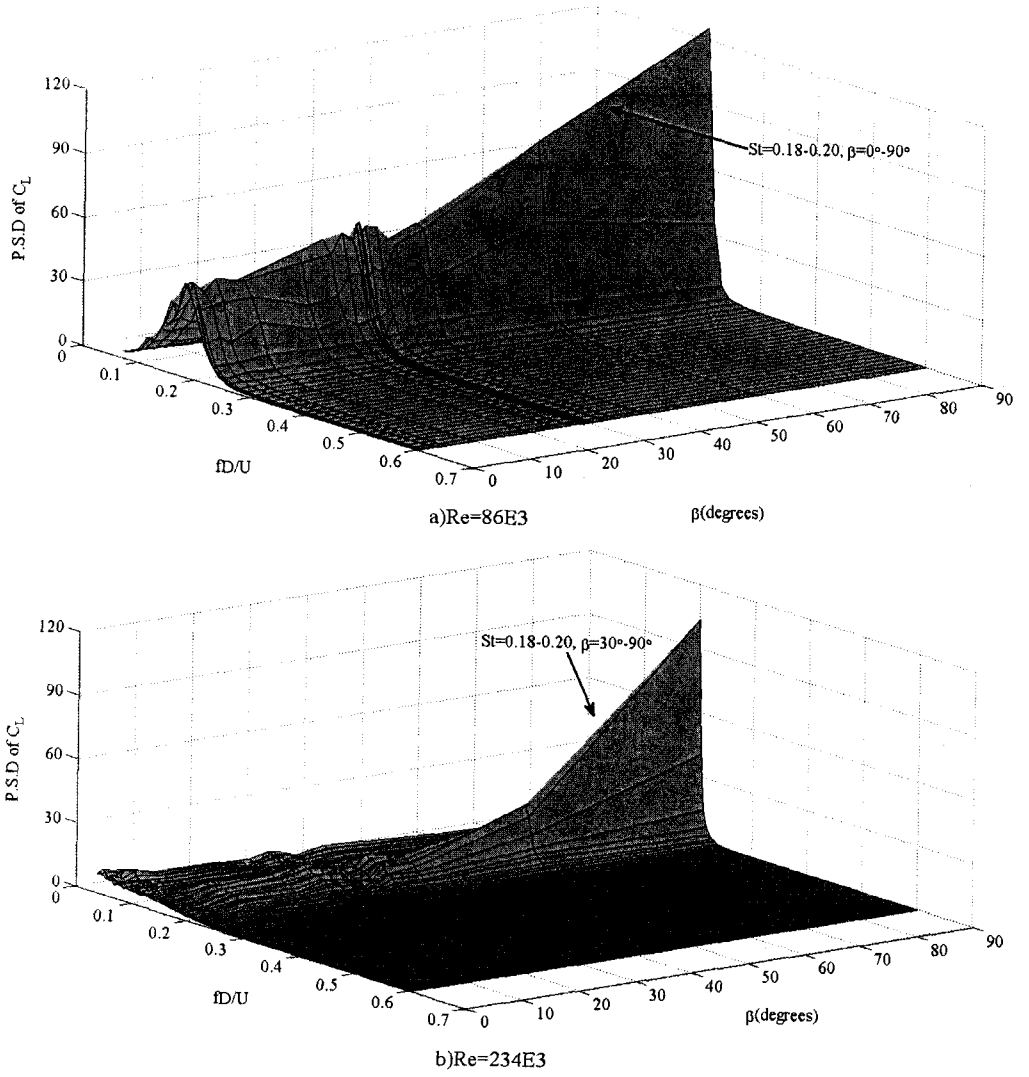

Figure 3-13- Power spectra analysis of lift force coefficient at z/D=1 (Ring 4) in the static tests when model is inclined by 54.7° against wind, including Setup 2C condition (α=54.7°, β=30°, γ = 54.7°);

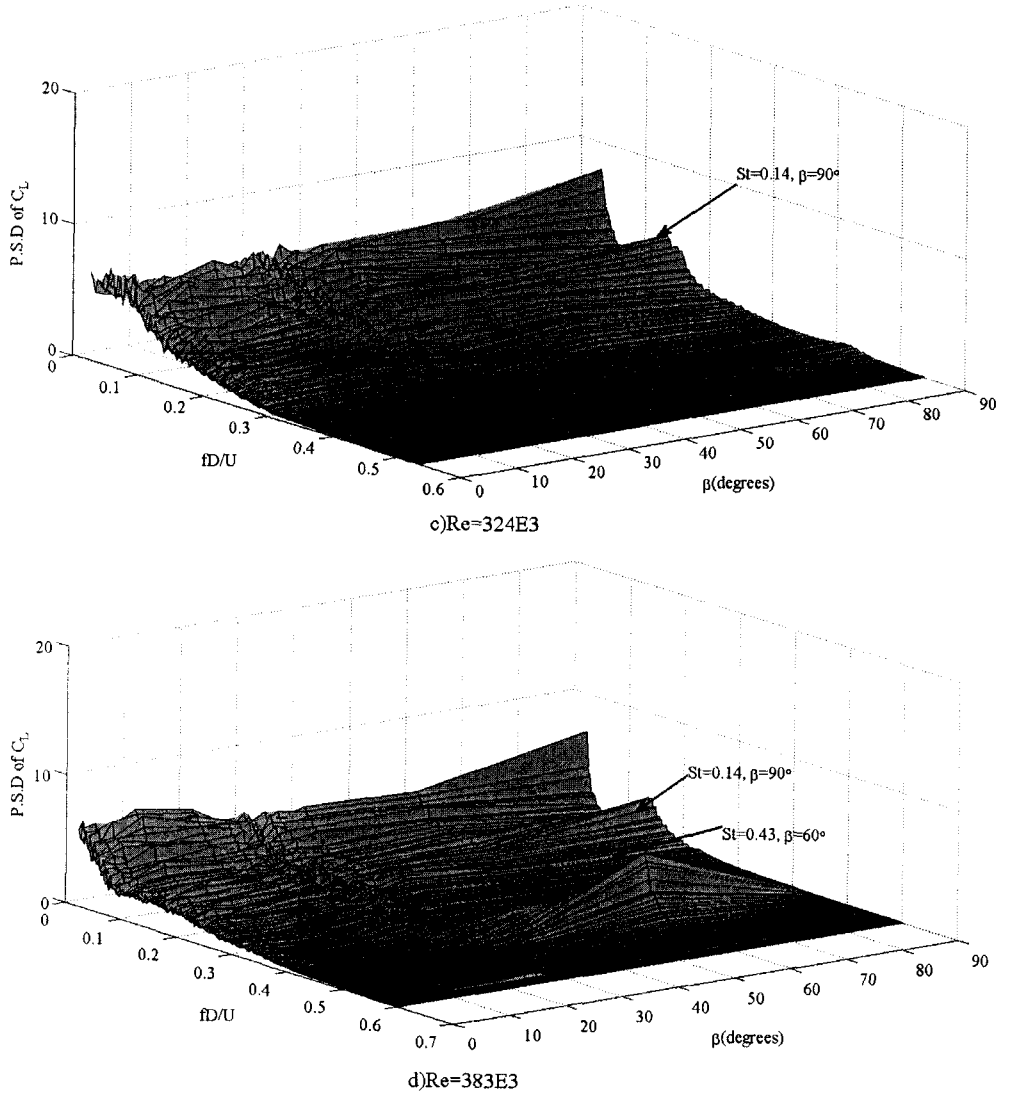

Figure 3-13- Power spectra analysis of lift force coefficient at z/D=1 (Ring4), in the static tests when model is inclined by 54.7° against wind, including Setup 2C condition (α=54.7°, β=30°, γ = 54.7°); (Contd.)

As it can be seen from Figures 3-13(a) and 3-13(b), within the subcritical Re range, for the yaw angles up to β≈40° (ϕ≈64°), the power spectra energy level does not change considerably. However, for β>40°, the growth in the energy levels is apparent. At Re=2.34×10^5, which is close to the upper limit of subcritical Re range, regular narrow banded vortex shedding occurs only for β>40° (ϕ>64°) more or less at the same

energy level as in Figure 3-13(a). In contrast, for $\beta<40°$, the vortex shedding becomes broad banded as shown in Figure 3-13(b).

As expected, when flow enters the critical regime as depicted in Figure 3-13(c) and Figure 3-13(d), at yaw angle close to 90°, the lift power spectra loses its dominance and drops almost by one order of magnitude. This drop occurs to a smaller degree for other yaw angles. The energy becomes more concentrated in the lower frequency range, though minor energy concentration peaks could still be observed at $fD/U=0.14\sim0.16$ and at $fD/U=0.43$. Unlike the subcritical case, in the critical range, decreasing yaw angle and hence increasing the intensity of axial flow component does not significantly alter the energy level. At $\beta\approx0°$, the power spectra moderately reduces to broadband low energy-level.

Since the observed divergent motion is not across-wind response, the power spectra of drag force is also investigated in the critical regime and presented in **Figure** 3-14. It can be seen that for smaller yaw angles ($\beta<40°$), the energy contained in drag has a broadband distribution. In the cross-flow case ($\beta=90°$), majority of the energy is concentrated in low frequency range without any distinctive peak. This is consistent with the phenomenon observed in the power spectra of lift force in the critical range (Figure 3-13(d)). The flow transition in the boundary layer is accompanied by low frequency intermittent motions destroying the regular vortex shedding caused by shear layer instability (Higuchi et al, (1989)). The low energy-level low frequency oscillations of flow field are associated with these intermittent motions in the boundary layer. For an inclined and/or yawed ($\beta\neq90°$) cylinder in flow, however, the broadband low energy-level oscillations corresponds to both axial and circumferential boundary-

layer instabilities. It is also interesting to note that at $Re=3.83\times10^5$, the highest critical Reynolds number studied, a broadband peak occurs around $\beta=30°$. The frequency corresponding to St=0.2 dominates the energy level.

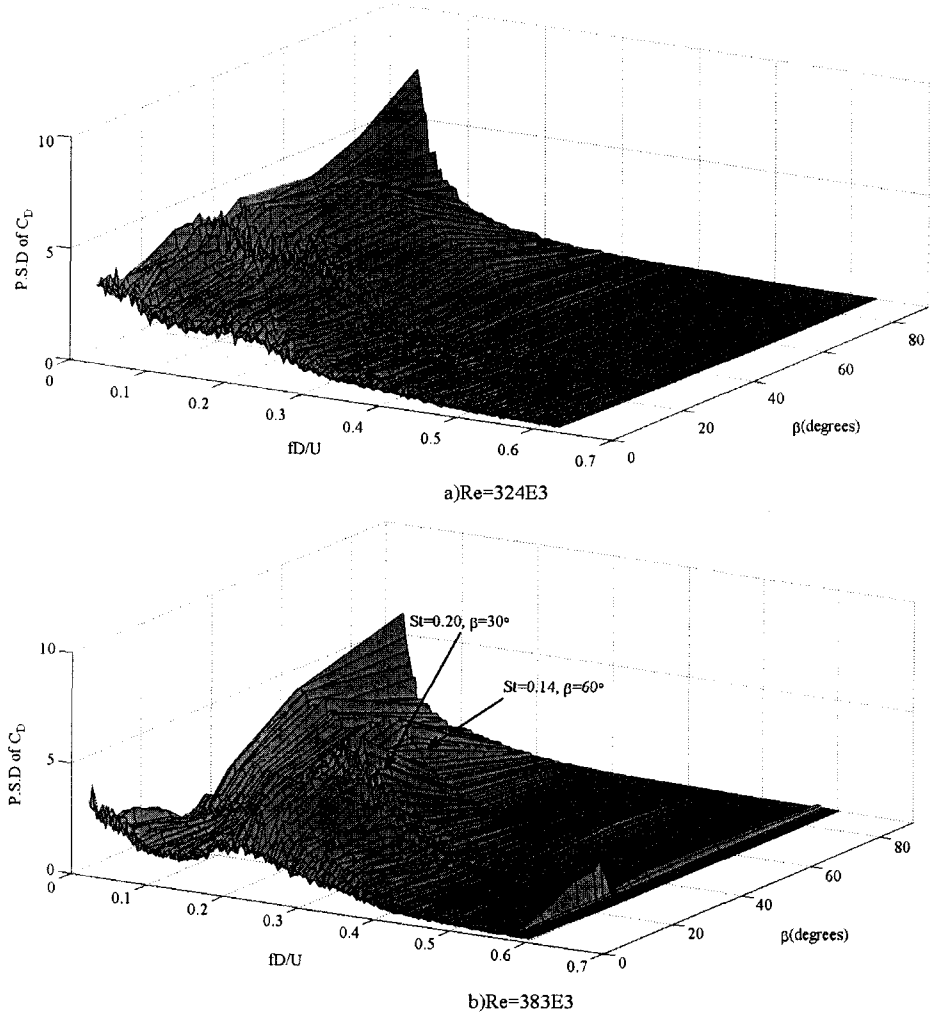

Figure 3-14- Power spectra analysis of drag force coefficient at z/D=1 (Ring4), in the static tests when model is inclined by 54.7° against wind, including Setup 2C condition ($\alpha=54.7°$, $\beta=30°$, $\gamma=54.7°$)

The power spectra of lift force for the limited-amplitude response observed in Setup 2A is presented in Figure 3-15, for the subcritical Re range of 1.74×10^5 to 2.34×10^5 where the unstable motion occurred. It is clear in the figure that the lift power spectra

changes from narrowband for $\beta \approx 0°\sim40°$ ($\phi \approx 60°\sim64°$) to more broadband with the increase of Reynolds number in this range which is consistent with the subcritical Re results in Figure 3-13 at $\phi \approx 60°$. This seems to affect the regular shear layer instability which causes regular Karman vortex shedding and leads to a breakdown in regular Karman vortex shedding. This breakdown is believed to be caused by the induced axial flow, i.e. for the wind-cylinder relative angle $\phi < 64°$, the normal-to-cylinder component of net vorticity vector due to axial boundary-layer becomes important. The net vorticity vector in such situation would not be parallel to the cylinder axis and therefore could weaken the regular shear layer instability caused by the parallel component of vorticity vector. Larger axial flow component would promote the flow transition from laminar to turbulence and serve to destroy the narrowband vortex shedding and broadens the power spectra (see Ramberg (1983) and Snarski (2004)). It is also revealed in Figure 3-13(a) and (b) and Figure 3-15 that as the yaw angle is swept from $\beta=90°$ to 0°, the peak frequency of vortex shedding varies gradually from $St \approx 0.20$ to 0.17. This appears to be caused by the same mechanism owing to the fact that the net amount of unparallel vorticity discharged to the wake is no longer parallel to the cylinder axis (Ramberg, 1983). Consequently, the vortex shedding frequency of an inclined circular cylinder in the current study would be less than that in the cross-flow case. Current results are fairly consistent with those by Snarski (2004) within the subcritical range. He introduced a Strouhal vortex regime for $\phi=60°\sim90°$ within which the vortex shedding became narrow banded. The narrowband energy distribution of regular vortex shedding regime was then replaced by high-level broadband energy for $\phi=45°\sim60°$. This was attributed to a fully separated turbulent flow behind the circular cylinder.

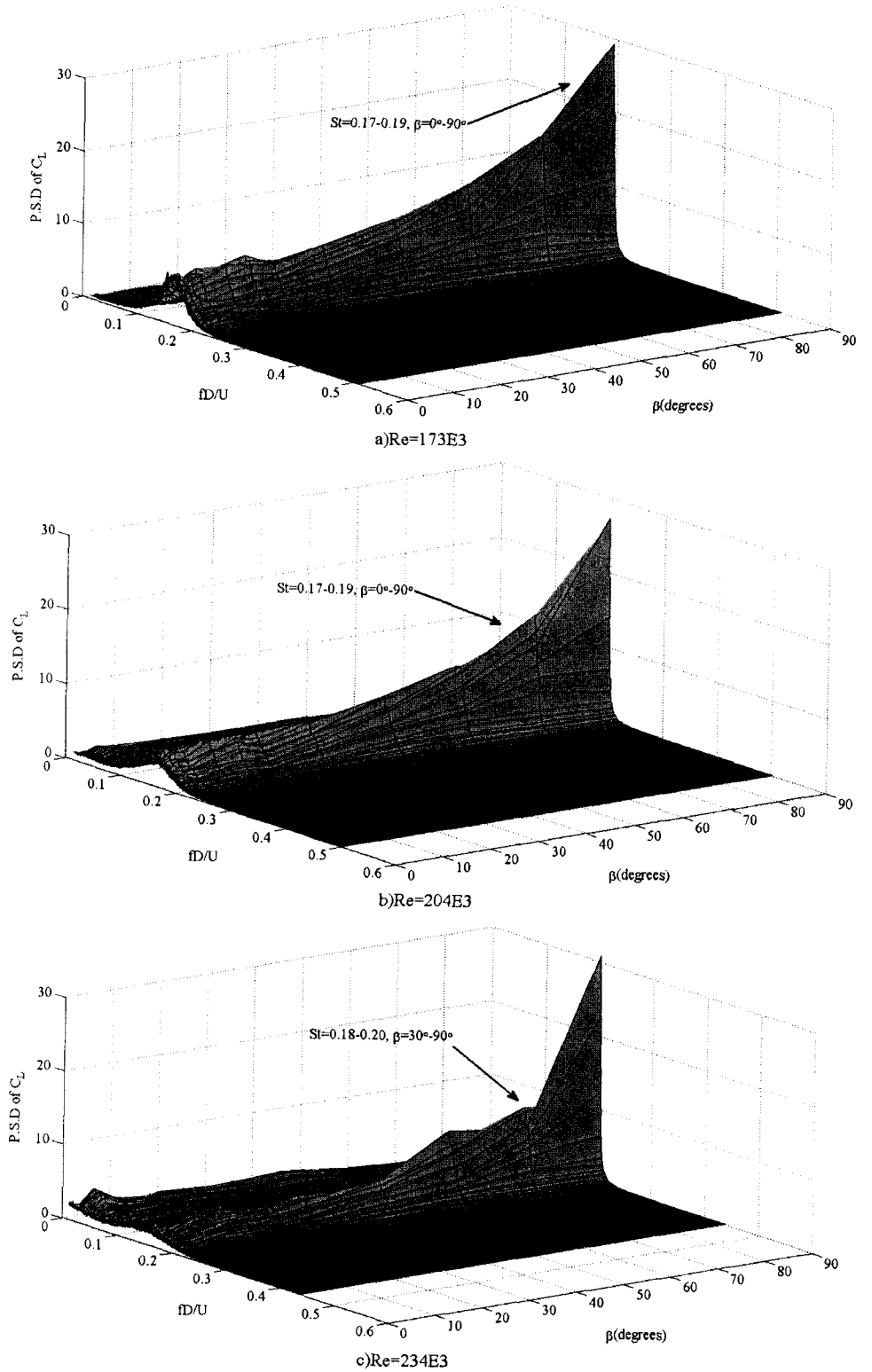

Figure 3-15- Power spectra analysis of lift force coefficient at z/D=1 (Ring4), in the static tests when model is inclined by 54.7° against wind, including Setup 2A condition (α=60°, β=0°, γ=90°)

Matsumoto et al. (1998, 2007a, and 2007b) noted that the mitigation of Karman Vortex shedding, caused by the introduction of axial flow in the subcritical regime, was the major source of the limited-amplitude unstable response. This type of response is suppressed when reaching higher Reynolds numbers, as shown in Figure 3-5 (for $Re>2.1\times10^5$). This is associated with the fact that within the subcritical regime, the fluctuations in the separation angle becomes relatively large just before the transitional Reynolds numbers. This would be accompanied by large fluctuations of lift force (Raeesi et al., 2008) within this Re range. When entering the transitional range, fluctuating lift and drag drop promptly. This effect, combined with the highly correlated spatial flow structure within the subcritical range as observed in Figure 3-12, seems to have major contributions to the limited-amplitude unstable response or the so-called high-speed vortex excitation observed in Setup 2A (ϕ=60°, γ=90°). When the regular Karman vortex shedding is mitigated because of axial flow, the interaction between the flow fields on both sides of the cylinder is also discouraged. However, the large values of fluctuating lift forces and correlation length still exist on the cylinder which would result in the observed instability (for $Re\approx1.7\times10^5\sim2.1\times10^5$). The magnitude of both fluctuating lift and correlation length drop considerably as shown in Figure 3-12 and Figure 3-15 when entering the transitional and the critical range. The unstable response is hence suppressed.

3.4 Concluding remarks

The possible excitation mechanisms associated with two different types of wind-induced cable vibrations have been investigated based on a series of wind tunnel tests

on a rigid circular cylinder model. Though the corresponded cylinder orientations of the observed divergent type of response and limited-amplitude unstable motion associated to the same wind-cable relative angles angle of 90°, the onset conditions and response characteristics of these two types of motion differed considerably. The divergent type response was observed at an orientation corresponding to full-scale cable inclined and yawed both with 45° against wind. The response had considerable components along the in-plane and out-of-plane directions, with the former being the major one. In contrast, the limited-amplitude instability occurred when a non-yawed cylinder inclined at 60° against wind. It had only one component in the out-of-plane direction, which coincided with the direction of lift force.

Unsteady surface pressure sampled at five different spanwise locations of a corresponding set of cylinder static tests were utilized to obtain the aerodynamic damping ratio, spatial correlation, and power spectra of sectional aerodynamic forces acting on the cylinder to reveal different possible mechanisms of the observed phenomena in the dynamic tests. A general expression for the aerodynamic damping ratio of a circular cylinder in any arbitrary orientation with respect to the on-coming flow was used (McDonald and Larose, 2006), which successfully predicted the negative aerodynamic damping ratio for the observed divergent instability.

A breakdown range was found for relative angles of $\phi \approx 55°\sim64°$ beyond which remarkable change in the symmetry and power spectra of flow field would occur. When reaching the critical Reynolds number, the formation and burst of flow separation bubbles on the surface of cylinder within this breakdown range leads to considerable negative values of $\partial C_L/\partial\phi$ term. The contribution of $\partial C_L/\partial\phi$ term within this

breakdown range along with negative values of $\partial C_D/\partial Re$ and $\partial C_L/\partial Re$ terms in the critical Re range was then pointed to be of great importance in the calculated total negative aerodynamic damping ratio. For the range of $\phi \approx 65° \sim 81°$ and $Re > 3\times10^5$ however, it seems that $\partial C_L/\partial Re$ and $\partial C_D/\partial Re$ terms have major contributions to the total negative aerodynamic damping ratios. Further experiments are required to investigate the possible occurrence of divergent motion associated with these negative values.

When the divergent response occurred, in addition to the negative aerodynamic damping ratios ζ_a, the spatial flow structure is also found to be highly correlated along the cylinder when the divergent response occurred. This suggested the collaboration of sectional aerodynamic forces over the cylinder length might be an important or even a necessary factor for the excitation of the first vibration mode of the cylinder model.

The limited-amplitude instability occurred at $\phi = 60°$ ($\alpha = 60°$, $\beta = 0°$) within the subcritical Re range ($Re \approx 1.7\times10^5$-2.1×10^5). This instability associated with the mitigation of regular Karman vortex shedding in the breakdown range while the spatial flow field was highly correlated. This instability can be suppressed by reaching critical Re range owing to the drop of the correlation length.

References

Bosch, H., 2006. Review of Bridge Cable Vibrations within the USA. Proceeding of 2006 Wind Induced Vibration of Cable Stay Bridges Workshop (on CD-ROM).

Cheng, S., Tanaka, H., 2005. Correlation of aerodynamic forces on an inclined circular cylinder. Wind and Structures an Int. J. 8(2), 135-146.

Cheng, S., Larose, G. L., Savage, M. G., Tanaka, H., Irwin, P. A., 2008a. Experimental study on the wind-induced vibration of a dry inclined cable—Part I: Phenomena. J. Wind Eng. Ind. Aerodyn. 96, 2231-2253.

Cheng, S., Irwin, P. A., Tanaka, H., 2008b. Experimental study on the wind-induced vibration of a dry inclined cable—Part II: proposed mechanism. J. Wind Eng. Ind. Aerodyn., 96, pp. 2254-2272.

Den Hartog, J.P., 1956. Mechanical Vibrations, forth ed. McGraw-Hill, New York Reprinted by Dover, New York. 1984.

Hayashi, T. and Kawamura, T., 1995. Non-uniformity in a flow around a yawed circular cylinder. Flow meas. Instrum. 6(1), 33-39.

Higuchi, H., Kim, H.J., and Farell, C., 1989. "On flow separation and reattachment around a circular cylinder at critical Reynolds numbers. J. Fluid Mech., 200, 149-171.

Hikami, Y. Shiraishi, N., 1988. Rain-wind induced vibration of cables in cable-stayed bridges. J. Wind Eng. Ind. Aerodyn. 29, 409-418.

Hoerner, S. F., 1965. Fluid Dynamic Drag. Hoerner Fluid Dynamics, Bricktown.

Honda, A., Yamanaka, T., Fujiwara, T., Saito, T., 1995. Wind tunnel test on rain-induced vibration of the staycable. Proceedings of International Symposium on Cable Dynamics, Lie`ge, Belgium, pp. 255–262.

Humphreys, J. S., 1960. On a circular cylinder in a steady wind at transition Reynolds numbers. J. Fluid Mech., 9, 603-612.

Irwin, P.A., Nedim, A., Telang, N., 1999. Wind induced stay cable vibrations a case study. Proceeding of the Third International Symposium on Cable Aerodynamics, Trondheim, Norway, pp. 171-176.

Main, J.A., Jones, N.P., 2001. Evaluation of viscous dampers for stay-cable vibration mitigation. Journal of Bridge Engineering ASCE. 6 (6), 385-397.

Marshal J. S., 2003. Wake dynamics of a yawed cylinder. Journal of Fluid Eng. 125, 97-103.

Matsumoto, M., 1998. Observed behavior of prototype cable vibration and its generation mechanism. Bridge Aerodynamics, Larsen & Esdahl (eds), Balkema, Rotterdam, pp. 189-211.

Matsumoto, M., Ishizaki, H., Kitazawa, M., Aoki, J. and Fujii, D., 1995. Cable aerodynamics and its stabilization. Proceeding of International Symposium on Cable Dynamics, Liege, Belgium, pp. 289-296.

Matsumoto, M., Shiraishi, N., Kitazawa, M., Knisely, C., Shirato, H., Kim, Y, Tsujii, M., 1990. Aerodynamic behaviour of inclined circular cylinders-cable aerodynamics. Journal of Wind Eng. and Ind. Aero. 33, 63-72.

Matsumoto, M., Yagi, T., Adachi, Y., Hatsuda, H., Shima, T., 2007a. Cross flow response of circular cylinders influenced by Karman vortex mitigation. Proceedings of Seventh International Symposium on Cable Dynamics, Vienna, Austria,

Matsumoto, M., Yagi, T., Adachi, Y., Hatsuda, H., Shima, T., 2007b. Sensitivity of dry-state galloping of cabled stayed bridges to Scruton number. Proceedings of Seventh International Symposium on Cable Dynamics, Vienna, Austria.

Matsumoto, M., Yagi, T., Tsushima, D., 1999. Vortex-induced vibration of inclined cables at high wind velocity. Proceedings of the 10th International Conference on Wind Engineering, Copenhagen, Denmark, pp. 979-986.

McDonald, J.H.G., 2002. Separation of the contributions of aerodynamic and structural damping in vibrations of inclined cables.Journal of Wind Engineering & Industrial Aerodynamics 90, 19–39.

McDonald, J.H.G., Larose, G.L., 2006. A unified approach to aerodynamic damping and lift/drag instabilities and its application to dry inclined cable galloping. . J. of Fluids and Structures. 22, 229-252.

Miyata, T., Yamada, H., Hojo, T., 1994. Aerodynamic response of PE stay cables with pattern-indented surface. Proceedings of International Conference on Cable-Stayed and Suspension Bridges (AFPC), Deauville, France, Vol. 2, 515–522.

Norberg, C., 2003. Fluctuating lift on a circular cylinder: Review and new measurements. J. Fluid and Struc. 17, 57-96.

Raeesi, A., Cheng, S., Ting., D. S. K., 2008. Spatial flow structure around a smooth circular cylinder in the critical Reynolds number regime under cross-flow condition. Wind and Structures, an Int. J. 11(3), 221-240.

Ramberg, S. E., 1983. The effects of yaw and finite length upon the vortex wakes of stationary and vibrating cylinders. J. Fluid Mech. 128, 81-107.

Roshko, A., 1954. On the development of turbulent wakes from vortex streets. NACA Report No., TR1191.

Roshko, A., 2001. Aspects of flow-induced vibrations. J. of Fluids and Structures. 15, 415-425.

Saito, T., Matsumoto, M., Kitazawa, M., 1994. Rain-wind excitation of cables of cable-stayed Higashi–Kobe Bridge and cable vibration control. Proceedings of International Conference on Cable-Stayed and Suspension Bridges (AFPC), Deauville, France, 2, pp. 507–514.

Schewe, G., 1983. On the force fluctuations acting on a circular cylinder in cross-flow sub-critical up to transcritical Reynolds numbers. J. Fluid Mech. 133, 265-285.

Shirakashi, M. Hasegawa, A. and Wakiya, S., 1986. Effect of the secondary flow on Karman vortex shedding. Bulletin of JSME. 29, No. 250.

Simiu, E., Scanlan, R. H., 1996. Wind Effects on Structures, an Introduction to Wind Engineering, John Wiley & Sons.

Snarski, S. R., 2004. Flow over yawed circular cylinders: Wall pressure spectra and flow regimes. Phys. Of Fluids. 16(2), 344-359.

Van Atta, C.W., 1968. Experiments in Vortex Shedding From Yawed Circular Cylinders. AIAA J. 6(5), 931–933.

Williamson, C. H. K., 1997. Advances in our understanding of vortex dynamics in bluff body wakes. J. of wind Eng. And Ind. Aerodyn. 69-71, 3-32.

Zdravkovich, M.M., 1997. Flow around circular cylinders, Fundamentals, Vol. 1, University Press, Oxford, England.

Chapter 4

Conclusions and suggestions for future work

4.1 Summary

Two different types of wind-induced cable vibration phenomena identified an earlier the wind-tunnel studies by Cheng et al. (2003 & 2008a) are investigated. The limited-amplitude instability was suppressed before reaching the critical Reynolds number regime. The divergent type response linked to galloping instability was found to be totally dependent on the emergence of critical Re range. To further uncover the flow characteristics within the critical regime, cross-flow past a circular cylinder was first studied in Chapter 2. The unsteady surface pressure data sampled at five spanwise locations of the cylinder model in the static tests were utilized with a number of analyses including time-averaged surface pressures, time-averaged and FFT of separation angle, and spatial correlation of aerodynamic characteristics. Subsequently in Chapter 3, using both dynamic and static tests results, different possible mechanisms of the two observed phenomena on the cable models are studied. A general expression for the aerodynamic damping of circular cylinder, spatial correlation and FFT of lift and drag forces were utilized to unveil the mechanisms behind each response. The concluding remarks of each chapter were presented in the following two subsections.

4.2 Circular cylinder in cross-flow

The unsteady surface pressures sampled at five different locations along the cylinder span were used to obtain time-averaged surface pressure distribution. The surface pressure contours demonstrated the existence of three-dimensional flow patterns in terms of cell-like structures at Reynolds numbers larger than 2.90×10^5. In addition, time-averaged circumferential pressure distribution at different longitudinal locations showed the characteristics of dual flow sub-regimes along the span of circular cylinder in the critical Re range. Therefore, the three-dimensionality of the flow was associated with different circumferentially asymmetric flow patterns along the cylinder span when entering or leaving TrBL1 regime. This led to the existence of two overlap regions at both upper and lower limits of TrBL1 regime.

The spanwise correlation coefficients of separation angles and sectional aerodynamic forces were also calculated. Strong spanwise correlation, i.e. well organized flow structure was observed before the transitions into the TrBL1 and TrBL2 regimes. These transitions were marked with the disruption of organized flow structures. More organized flow structures were observed in the TrBL1 regime at $Re=3.33\times10^5$. The large spanwise lift correlation coefficients seemed to be associated with the observed spanwise sub-systems in terms of cell-like structures. The size of cell-like structures was measured by in-phase fluctuating points which spanned approximately two cylinder diameters.

4.3 Excitation mechanisms of wind-induced instability phenomena of inclined and/or yawed circular cylinder

The possible excitation mechanisms associated with two different types of wind-induced cable vibrations have been investigated based on a set of earlier dynamic and static wind-tunnel test results. Though the divergent type of response and limited-amplitude unstable motion were observed at the same cable-wind relative angle of 60°, the onset conditions and response characteristics of these two types of motion differed considerably. The corresponding orientation to the divergent type response was a full-scale cable inclined and yawed both with 45° against wind. Two considerable components of response were along the in-plane and out-of-plane directions, with the former being the major one. The limited-amplitude instability occurred when a non-yawed cylinder inclined at 60° against wind. Unlike the divergent response, it had only one component in the out-of-plane direction, which coincided with the direction of lift force. Consequently, it was noticed that when the cylinder were both inclined and yawed, the direction of motion would have two components along the in-plane and out-of-plane directions with the major one being closer to the direction of lift force.

In order to investigate the divergent type response and its possible connection to galloping, a general expression of the aerodynamic damping ratio of a circular cylinder vibrating along any arbitrary direction with respect to the on-coming flow (McDonald and Larose, 2006) was used. This expression successfully predicted the observed divergent instability in Setup 2C (ϕ=60°, γ=54.7°) by producing negative aerodynamic damping ratios.

Additionally, the circumferential pressure distribution on the inclined and/or yawed circular cylinder showed a breakdown range (beyond which remarkable changes in the symmetry of flow field could occur) existed for $\phi \approx 55°\sim64°$. This was linked with the formation or burst of the separation bubbles on the surface of cylinder. Small changes in ϕ within this range, led to dramatic alternation of the flow characteristics. The contribution of $\partial C_L/\partial \phi$ term within this breakdown range was then pointed out to be of great importance in the obtained negative aerodynamic damping ratios along with the negative values of $\partial C_D/\partial Re$ and $\partial C_L/\partial Re$ terms in the critical Re range.

Within this breakdown range, the correlation length of sectional lift and drag forces showed that the spatial flow was highly correlated along the cylinder. It seemed that due to the collaboration of sectional aerodynamic forces, correlation length is a determining or possibly a necessary factor for the onset of excitation for the first vibration mode of cylinder (in addition to the negative aerodynamic damping ratios). Further experiments could serve to verify this hypothesis, e.g. the aerodynamic damping ratio in the range of $\phi \approx 65°\sim81°$ and $Re>3\times10^5$ where the $\partial C_L/\partial Re$ term had the dominant contribution, even though it was not accompanied with large correlation length values. It is also worth noting that although the divergent type response was highly encouraged by the formation and burst of separation bubble and TRBL1 regime, it has never been observed on real bridge site. This may be due to the existence of natural turbulence in wind that could eliminate the formation of the separation bubbles as noted by Larose et al. (2006).

The so-called high-speed vortex excitation was observed for the breakdown range $\phi \approx 60\sim64°$ in which the regular Karman vortex shedding was suppressed within the subcritical Re range ($Re \approx 1.7\times10^5\sim2.1\times10^5$). This type of response was accompanied with high correlation length values in the subcritical Re range. By entering the critical regime, the limited-amplitude response was suppressed, which was associated with the decrease of correlation length values. It was then speculated that the breakdown range may be associated with the strength of axial flow and the component of vorticity discharged by the axial component of flow. These which could alter the regular Karman vortex shedding as pointed out by Marshal (2003) and Snarsky (2004).

4.4 Suggestions for future work

Flow past a circular cylinder has been found to be exceedingly rich in fluid dynamics phenomena. From a fundamental point of interest, the formation mechanism of the cell-like pressure structures on the surface of cross-flow circular cylinder and its connection with separation bubbles are not clear. More research needs to be conducted for clarification of fluid dynamic phenomena associated with formation of cell-like structures. The existence of dual flow characteristics along the cylinder span has to be verified by flow visualization. Flow visualization and other measurements of the velocity field would help reveal the mechanism of the large spanwise correlation of the flow patterns within TrBL1 regime.

From a structural and design point of interest, there are still much more about the excitation mechanisms of bridge stay-cables to be unveiled. More experimental data are required where the general expression for the aerodynamic damping ratio predicted

negative values for $\phi \approx 65° \sim 81°$ and $Re > 3 \times 10^5$ range. These negative values, however, were not accompanied by the large correlation length. Therefore, more experiments at the above-mentioned range could verify the role of high correlation length in the onset of divergent response of the cable model. In addition, it has been noted that dry-inclined cable galloping has never been observed on the real bridge site which might be due to the effect of wind turbulence in eliminating TrBL1 regime in a natural enviroment. Experiments with different turbulence intensities could verify this hypothesis.

References

Cheng, S., Tanaka, H., 2005. Correlation of aerodynamic forces on an inclined circular cylinder. Wind and Structures. An Int. J., 8(2), pp. 135-146.

Cheng, S., Larose, G. L., Savage, M. G., Tanaka, H., Irwin, P. A., 2008a. Experimental study on the wind-induced vibration of a dry inclined cable—Part I: Phenomena. J. Wind Eng. Ind. Aerodyn. 96, 2231-2253.

Larose, G. L., Zasso, A. and Giappino, S., 2006. Experiments on a yawed stay cable in turbulent flow in the critical Reynolds number range.

Marshal J. S., 2003. Wake dynamics of a yawed cylinder. Journal of Fluid Eng. 125, 97-103.

Snarski, S. R., 2004. Flow over yawed circular cylinders: Wall pressure spectra and flow regimes. Phys. Of Fluids. 16(2), 344-359.

Appendix A: Curve fitting and Uncertainty Analysis

Instantaneous surface pressure tap readings were recorded for a sampling time of 120 and 60 seconds respectively at 400Hz and 1200Hz data acquisition rate. Afterwards, the recorded data were averaged over the whole sampling period. Pressure coefficient was defined as $C_p = P / (0.5\rho V^2)$, where V is the wind tunnel speed, ρ is the air density, and P is the measured gauge pressure. Using linear least square method, curve fitting was then applied to the time-averaged pressure data to obtain coefficients of polynomials varying from order of 12 to 22. Figure A-1 shows the sum of squared errors (SSE) in the polynomial fitting process for different order, n, of applied polynomials at 7 different Reynolds numbers. The polynomial fitting error was defined as the difference between pressure coefficient (C_P) of time-averaged data at each pressure tap, and the prescribed values of pressure coefficient by the fitted polynomials at the corresponding circumferential location.

It can bee seen from Figure A-1 that the smallest errors occur over the range of n=16-20, out of which the errors become drastically larger. Also, at $Re=3.80\times10^5$, the polynomial fitting errors seem to be higher for any n attempted. Figure A-2 shows the fitted curves and captured time-averaged data points for four different polynomial orders of n=16-19 at $Re=3.80\times10^5$.

It is evident from the figures that once the polynomial order becomes higher, another error arises, i.e. the miss-prediction of pressure coefficient between regions of $\theta=0^\circ$-30° and $\theta=330^\circ$-360°. These errors are corresponded to the number of roots, whether real or imaginary, that each polynomial could produce. As the polynomial

order increases, these errors also increase and an undesirable curve shape forms at θ=0°-30° and θ=330°-360° ranges. This predicted pressure distribution in the mentioned regions, definitely differs from the expected pressure distribution that can be found in the literature. Consequently, these differences must be regarded as undesired errors due to the fitted polynomial order. It can be seen from Figure A-2(a), when n=16, these undesired errors are less as compared to those shown in Figures A-2(b) and A-2(d).

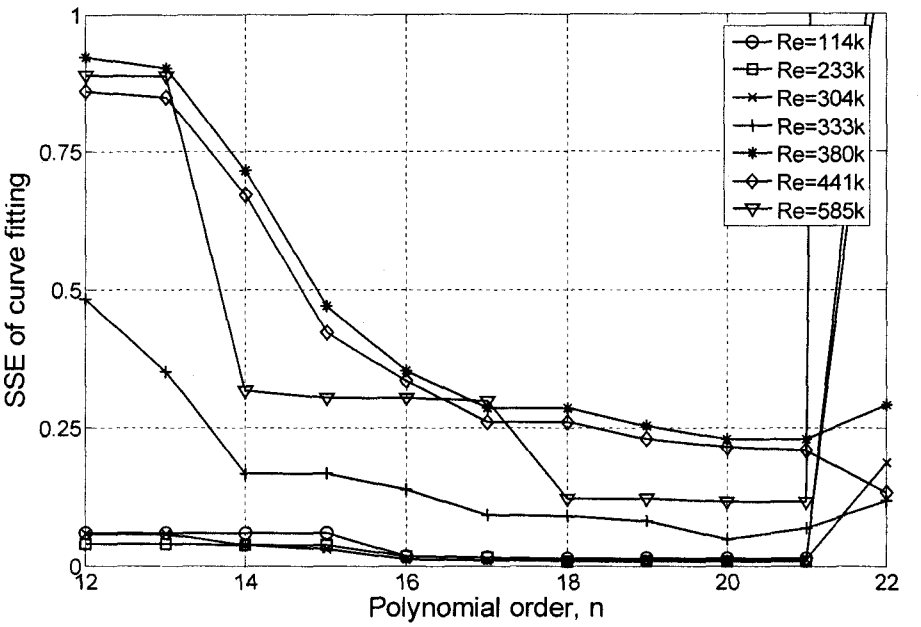

Figure A-1 Sum of squared errors of polynomial fitting at 7 different Reynolds numbers

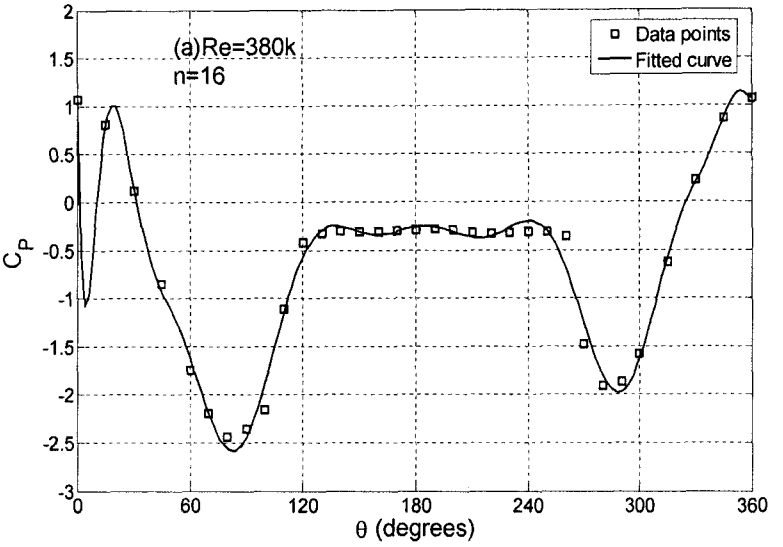
(a)Re=380k
n=16
Data points
Fitted curve
C_P
θ (degrees)

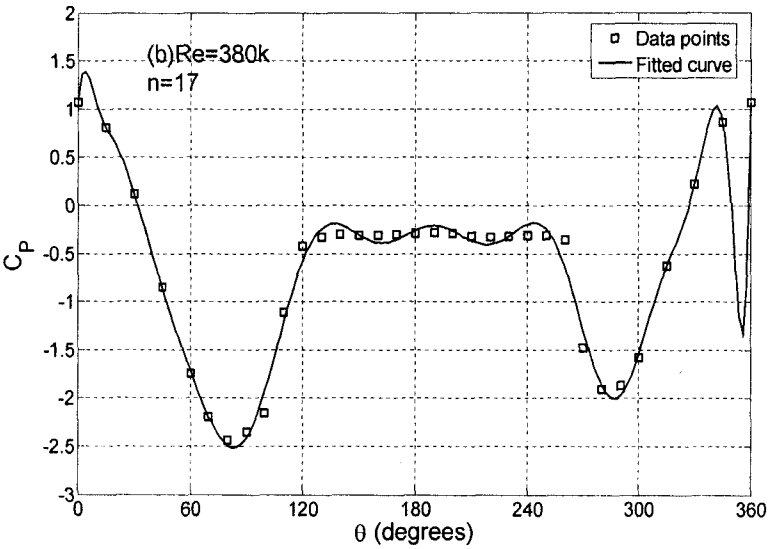
(b)Re=380k
n=17
Data points
Fitted curve
C_P
θ (degrees)

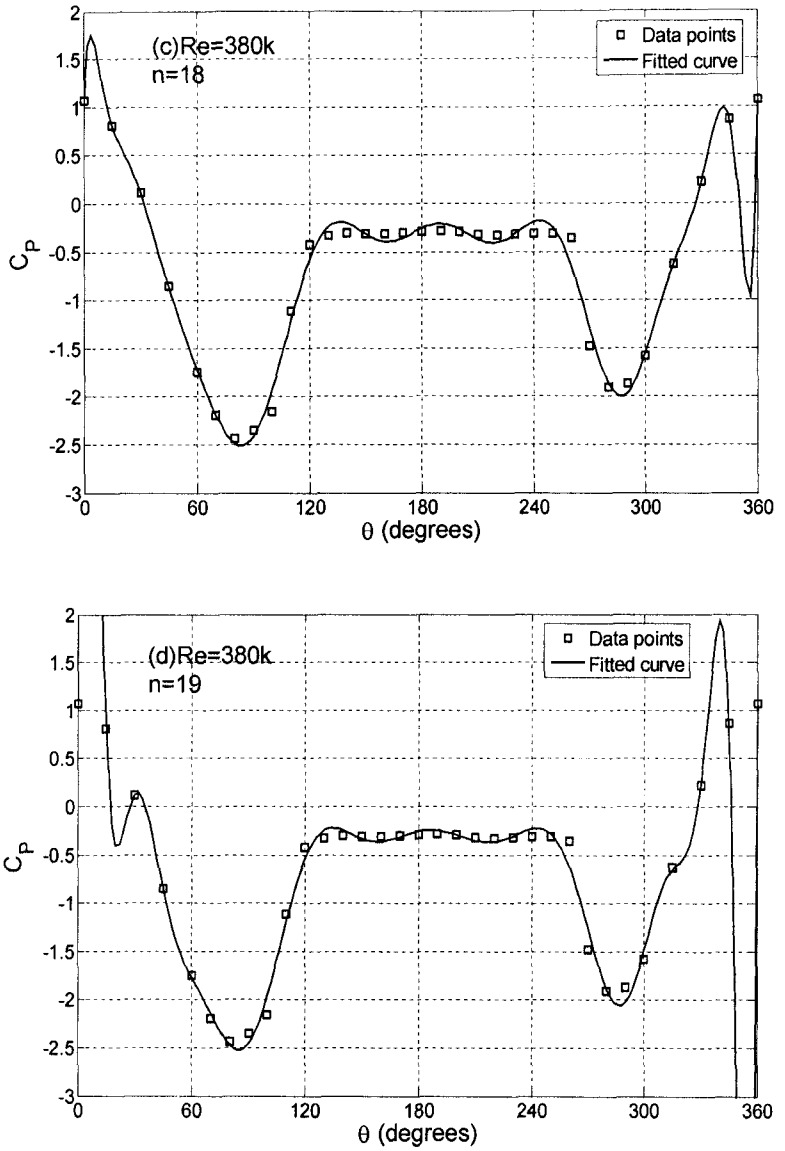

Figure A-2 Fitted polynomials to the time-averaged pressure coefficient data at Re=441k; (a) n=16, (b) n=17, (c) n=18, (d) n=19

In order to decide the curve fitting process, the level of errors induced during the experiments and also the curve fitting errors must be studied. To estimate the level of former errors, the uncertainty analysis was conducted based on the ambient during experiment and information of the experimental facilities.

(a) The following assumptions were made in order to determine the uncertainty in the air density:

- Duration of the experiments is such that semi-diurnal pressure variation can be taken.
- A typical standard deviation of semi-diurnal pressure variation is U_{Patm}=0.53mBar=103.88Pa.
- A typical indoor temperature could be taken as 20°C.
- A conservative temperature change during the experiment might be taken ±2°C.

Based on the above mentioned assumptions and using ideal gas law for air, $P=\rho RT$, the density of air can be calculated as: $\rho=1.1927\pm0.0082$ kg/m^3 ($U\rho$=0.0082kg/ m^3).

(b) The velocity of wind tunnel was measured using Pitot tube. The following assumptions were made to determine uncertainty in the velocity of wind tunnel:

- Assume 1% error in the dynamic pressure caused by a maximum yaw angle of 8° in the direction of Pitot tube with respect to the on-coming flow direction (Figliola and Beasly, 2005).
- Using $P_{dyn}=0.5\rho V^2$, the uncertainty in the wind tunnel velocity values can be calculated by knowing uncertainty in the dynamic pressure and density (U_{Pdyn}/P_{dyn}=1% & U_ρ=0.0082 kg/m^3).

Tap pressures were scanned by Scanivalve ZOC™Kulite. Using the specification sheets of this pressure scanner and within the current pressure range, the bias in the measured pressures is 0.08% of full-scale, which consequently would be U_P=276Pa.

(c) Using $C_p = P / (0.5\rho V^2)$, the uncertainty in the time-averaged pressure coefficient values can be calculated for each pressure tap and at the tested Reynolds number range as below:

$$U_{Cp} = \sqrt{\left(\frac{\sigma C_p}{\sigma \rho} U_\rho\right)^2 + \left(\frac{\sigma C_p}{\sigma V} U_V\right)^2 \left(\frac{\sigma C_p}{\sigma P} U_P\right)^2} \qquad \text{(A-1)}$$

Figure A-3 illustrates the sum of squared uncertainties in the raw data (SSE) at 7 Reynolds numbers within the tested range. It can be clearly seen from the figure that the sum of errors decreases drastically with the increase of the Reynolds number. Comparing to Figures A-1 and A-2, it can be implied that at lower Reynolds numbers, the uncertainty in the raw data predominates; while at higher Reynolds numbers, curve fitting error becomes a matter of concern. Consequently, the polynomial fitting order should be selected such that not only to keep curve fitting errors not higher than uncertainty in the raw data, but also to make a balance between polynomial fitting errors and those errors that shown in Figure A-2. Therefore, the polynomials with the order of 16 were found to satisfy all the above mentioned concerns better. Hence, for consistency, all curve fittings were applied by the use of 16^{th} order polynomials.

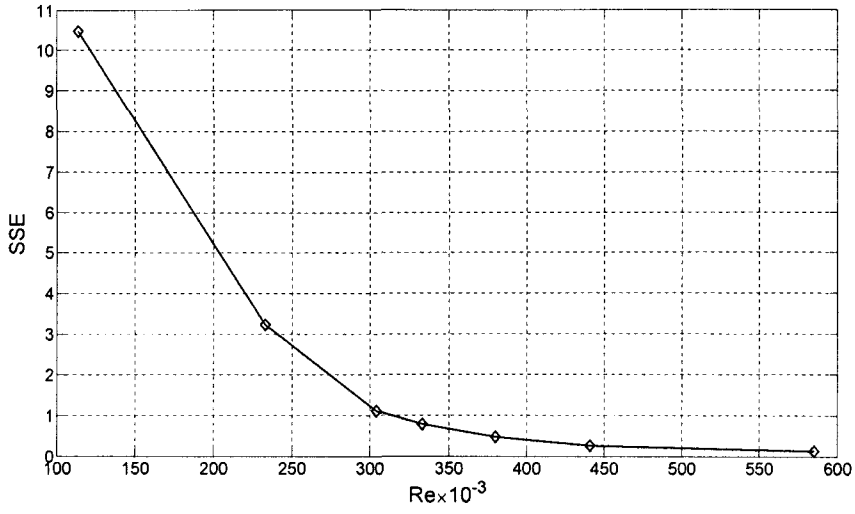

Figure A-3 Sum of squared uncertainties of time-averaged pressure tap readings at 7 Reynolds numbers within the tested range

Appendix B: Copyright permission

Request for the reproduce of the copyrighted material and the response of the Journal editor in chief:

To: <shaohong@uwindsor.ca>
From: "CHOI_CK" <cck@kaist.ac.kr>
Date: 12/14/2008 06:21PM
Subject: Re: Permission to reproduce materials in WAS 571

Dear Prof Cheng:

We are happy to grant you a permission to reproduce some parts of your published article in Wind and Structures as you requested.

Good Luck !!

C.K. Choi

Editor-in-Chief, WAS

----- Original Message -----

From: shaohong@uwindsor.ca

To: cck@kaist.ac.kr

Sent: Thursday, December 11, 2008 7:11 AM

Subject: Permission to reproduce materials in WAS 571

Dear Prof. Choi:

RE: Spatial flow structure around a smooth circular cylinder in the critical Reynolds number regime under cross-flow condition By Raeesi, Cheng and Ting

The paper listed above was published in Wind and Structures (2008, May issue, Vol.11, No.3). We will need your permission to reproduce the results in the Master's thesis by Raeesi. Thank you!

Regards

Shaohong Cheng, Ph.D. P.Eng.
Assistant Professor

Department of Civil and Environmental Engineering
University of Windsor
401 Sunset Avenue, Windsor Ontario, N9B 3P4

Vita Auctoris

Arash Raeesi was born in 1983 in Tehran, Iran. He graduated from Farzan High School in 2001. From there he went on to the University of Tehran, Iran where he obtained a B.Sc. in Mechanical Engineering in 2006. Having started in January 2007, he is currently a candidate for the Master's degree in Mechanical Engineering at the University of Windsor and hopes to graduate in winter 2009.